Development and Properties of All-Dielectric and Metal-Dielectric Heterostructures at Atomic Scale

seit 1558

Dissertation

zur Erlangung des akademischen Grades Doctor rerum naturalium

(Dr. rer. nat.)

vorgelegt dem Rat der Physikalisch-Astronomischen-Fakultät der

Friedrich-Schiller-Universität Jena

von

Pallabi Paul

geboren in Kalkutta (Kolkata), Indien

Gutachter:

1. Dr. rer. nat. Adriana Szeghalmi, Friedrich-Schiller-Universität Jena
2. Prof. Dr. Detlev Ristau, Leibniz Universität Hannover
3. Prof. Dr. Erwin Kessels, Technische Universität Eindhoven

Tag der Disputation: 07.11.2023

Dedicated to my Ma and Baba

Contents

Chapter 1

Introduction

Discoveries of new materials have been among the greatest achievements of every era of human civilization. They have been an integral part of the growth and prosperity of our lives since the beginning of history, while opening the door to new technologies. With the development of science and technology and the demand for miniaturization of device platforms, a new generation of nano and Angstrom scale materials have emerged into the centre of attention. Such ultrathin materials can inherently possess very unique properties as compared to their bulk counterparts [1, 2]. Therefore, the creation of novel nanoscale materials with tunable functionalities has been of immense interest. Among various nanoscale systems, heterostructures of different classes of materials enable materials with significantly different properties than the individual constituents. These heterostructures consist of alternating layers of different materials, e.g., oxides [3, 4], nitrides [5], fluorides [4], insulators [6–8], semiconductors [9–11], met-als [12–15], and even 2-dimensional materials [16–19]. As the individual thickness of the constituents decreases, new properties can emerge due to quantizing ef-fects [20]. Atomically engineered systems pave the way towards the solution of many technological challenges. The tailored materials manifest fascinating struc-tural, electrical, magnetic, optical, and mechanical properties determined by their compositions. The individual layer thickness can be scaled down to nanometer or even sub-nanometer scales. It is therefore interesting to study the unique impact of such a length scale on the resulting properties of materials.

In order to grow ultrathin films (thickness < 2 nm), and their heterostructures, cutting-edge atomic scale processing techniques need to be developed and implemented. One of the most precise techniques established in the 1970s for depositing high-purity monocrystals and their heterostructures is molecular beam epitaxy (MBE) [21–23]. It has been instrumental in the development of III-V compounds [24], semiconductor devices [25], quantum materials [26,27], and nanoelectronics [28] as a whole. However, MBE requires a highly controlled environment, ultrahigh vacuum (10^{-8} - 10^{-12} mTorr) chamber, as well as suitable crystalline substrates resulting in high-quality layer by layer epitaxial thin films with relatively low growth rate in comparison to conventional evaporation and sputtering techniques. Therefore, this method has been facing a continuous challenge both technologically and economically to scale up such processes for industrial production. Further, MBE poses limitations on the choice of substrates to reduce the lattice mismatch between the substrate and the coating. These stringent conditions have intrigued the development of further relatively flexible yet atomically controlled growth techniques for various amorphous and crystalline thin films.

The advancement of nano-structuring and coating technologies down to atomically controlled dimension and composition, for instance, electron beam lithography, atomic layer deposition, and atomic layer etching have enabled the quest of modern device fabrication. Among them atomic layer deposition (ALD) has been a very promising technology to achieve high quality thin films for a wide range of applications [29], e.g., integrated photonics [30–33], semiconductors [34, 35], barrier coatings [36], photovoltaic [37,38], electrical [39,40] and optical applications [41–43]. ALD is basically a chemical coating technology that enables precise thickness and composition control at the nanoscale [44]. Furthermore, being based on self-limiting surface reactions, ALD provides conformal films on any 3D substrate geometry. This has indeed been the need of the hour to satisfy the ongoing demand of 3D device architectures for size miniaturization. In the conventional thermal ALD, the surface reactions are activated using substrate heating. An alternative approach for providing the required energy can be implemented based on plasma (energy) enhanced ALD [45,46], where the substrate is exposed to energetic radicals generated by the plasma allowing for low-temperature depositions.

This dissertation deals with the development of all-dielectric and metal-dielectric heterostructures down to atomic scale. We have leveraged the precise thickness and composition control provided by the ALD technique. This approach allows for the creation of heterostructures with precise control at the atomic level, thereby tailoring their functionalities. Oxide-based heterostructures of Al_2O_3/TiO_2 have found various applications in organic light emitting diodes [47], organic thin film transistors [48], photovoltaics [49] or optical coatings [41, 42]. Previous studies have reported on structural, mechanical, and optical properties of Al_2O_3/TiO_2 nanolaminates grown by thermal ALD [50,51] and PEALD methods [52], respectively. Alongside, the exploration of the quantum confinement effect in dielectric materials is gaining a lot of interest due to their improved optical and optoelectronic properties [20,53]. Among dielectrics, oxide interfaces manifest many novel phenomena, such as, tunable electrical and optical confinement in Ta_2O_5/SiO_2 nanolaminates [53], enhanced photoluminescence in Al_2O_3/ZnO nanolaminates [20], improved laser induced damage threshold in TiO_2/SiO_2 and HfO_2/Al_2O_3 nanolaminates [54]. This dissertation presents the limits on the manipulation of optical properties of Al_2O_3/TiO_2 heterostructures at atomic scale.

Alternative layers of metal and dielectric ultrathin films for heterostructures, or metallic nanoparticles embedded in dielectric matrices could lead to a plethora of new functionalities. It has remained challenging to grow thin metallic layers while minimizing the percolation threshold thickness as much as possible. Ultrathin metallic layers have been explored for improved applications in nanoelectronics, plasmonics, and photonics [55–62]. Metal dielectric multilayer structures have revealed remarkable applications in enhancing optical nonlinearity by implementing $LiNbO_3$ in Au nanorings [58], photocatalysis based on Cu/TiO_2 heterostructures [63], and ultrafast transport of plasmonic electrons [64], to name only a few. A unique combination of noble metal iridium (Ir) in a dielectric matrix of Al_2O_3 has been introduced in this work for understanding the limit of atomic scale fabrication of ultrathin metallic coatings along with tailored properties depending on the composition of heterostructures.

A brief outline of the dissertation is as follows: Chapter 2 provides a perspective on the theoretical background of the investigations performed in this research. Material dispersion models and effective medium approximation approaches have been discussed for reliable determination of the optical properties of the heterostructures. It elucidates the idea of creating quantum well structures composed of heterostructure films. Further, it demonstrates the basics of designing multilayer interference coatings which have been eventually applied in antireflection coatings using dielectric heterostructures. Following this, a brief overview of an emerging application of optical thin films towards alternative nonlinear optical materials is given. Chapter 3 outlines a detailed description of the ALD and plasma enhanced ALD (PEALD) techniques. The applied ALD equipments, corresponding precursors, and ALD process parameters are thoroughly described. Chapter 4 briefly illustrates the set of thin film characterization techniques performed for evaluating the growth and various properties of the heterostructures. Chapter 5 focuses on the development of dielectric heterostructures. It reveals the growth and properties of such nanoscale materials in detail. A case study has been thoroughly performed using Al_2O_3/TiO_2 interfaces. The evolution of structural and optical properties along with an emergence of quantizing effects based on the reduction of layer thickness have been thoroughly investigated. An antireflection coating for 355 nm wavelength has been demonstrated by broadening the application window of TiO_2 via the creation of heterostructures with Al_2O_3. Chapter 6 presents the growth and investigations of atomically thin heterostructures based on Ir/Al_2O_3 systems. This chapter shows detailed analyses of the film properties, e.g., the formation of a nearly metallic monolayer, new structural features along the metal-dielectric interfaces, and the evolution of linear optical properties. The potential to create epsilon-near-zero (ENZ) materials via precise composition control by ALD has been explored. The role of heterostructures in nonlinear optical processes, such as second harmonic generation (SHG) has also been briefly addressed. Chapter 7 summarizes the contents of this dissertation and provides an outlook for future research in broadening the material basis available for novel optical applications by employing emerging atomic scale processing technologies.

Chapter 2

Theoretical methodology

This chapter provides an overview of the fundamental concepts shaping the ba-sis of the research performed in this dissertation. Various multi-oscillator models were explained in order to determine the optical dispersion spectra of single ma-terial ultrathin films and their heterostructures. These models pave the path for understanding the optical response of such structures. Additionally, the effective medium approximation (EMA) approaches have been discussed for describing the dielectric function of composite materials. This chapter also introduces the quantum confinement effect and optical quantizing structures. Further, it discusses the basics of developing multilayer interference coatings. This chapter concludes with a general overview of the emergence of nanoscale nonlinear optical materials.

2.1 Dispersion function

It is fundamental from the perspective of creating optical thin films and heterostructures to precisely determine the film thickness and optical dispersion behaviour of them. Such estimations can be performed experimentally by implementing the spectroscopic ellipsometry technique, as discussed in Chapter 4.1. The change in polarization of the incident beam upon reflection from the sample is recorded in terms of amplitude and phase. In order to extract the optical constants of thin films, various multi-oscillator models have been implemented to fit the measured ellipsometric parameters. Historically, the first empirical dispersion equation has been developed by Cauchy in 1836, and can be expressed as,

$$n(\lambda) = A + \frac{B}{\lambda^2} + \frac{C}{\lambda^4} + \ldots \tag{2.1}$$

$$k(\lambda) = 0 \tag{2.2}$$

This model is used to describe the materials in a transparent regime, considering the imaginary part of the refractive index k to be zero. A is a dimensionless parameter, which portrays the linear trend of the dispersion towards longer wavelengths. The terms containing B and C become negligibly small at higher values of λ. B (nm^2) and C (nm^4) describe the curvature for n while approaching shorter wavelength λ, i.e., the curvature of the dispersion.

For the description of absorbing materials, multi-oscillator models have been developed. The multi-oscillator models have to be consistent with the Kramers-Kronig relation, which explains the mutual dependence of the real part ϵ_1 and imaginary part ϵ_2 of the dielectric function of a material [65].

$$\epsilon_1(\omega) = 1 + \frac{2}{\pi}\int_0^{\infty} \frac{\omega'\epsilon_2(\omega')}{\omega'^2 - \omega^2} d\omega \tag{2.3}$$

$$\epsilon_2(\omega) = -\frac{2\omega}{\pi} P \int_0^{\infty} \frac{\omega'\epsilon_1(\omega') - 1}{\omega'^2 - \omega^2} d\omega \tag{2.4}$$

Equations 2.3 and 2.4 describe the Kramers-Kronig relationship, where P is the Cauchy principal value of the integral, ω and ω' are angular frequencies. Two important models used for the description of amorphous dielectrics are the Tauc-Lorentz and the Cody-Lorentz models. The Tauc-Lorentz model simulates the joint density of states by combining the Tauc band edge with the classical Lorentz broadening function, giving an expression for the imaginary part of the complex dielectric function as expressed below,

$$\epsilon_{2,[Tauc-Lorentz]}(E) = \epsilon_{2,[Tauc]}(E).\epsilon_{2,[Lorentz]}(E) \tag{2.5}$$

$$\epsilon_{2,\mathrm{Tauc-Lorentz}}(E) = \begin{cases} \frac{1}{E}\frac{AE_0C(E-E_g)^2}{(E^2-E_0^2)^2+C^2E^2}, & \text{if } E > E_g \\ 0, & E \le E_g \end{cases} \tag{2.6}$$

where A is the amplitude, C is the broadening, E_0 is the peak transition energy, E_g is the energy band gap, and E is the photon energy ($E = h\nu$). Even though proven well for many amorphous materials, this model has some limitations due to the fact that the imaginary part of the dielectric function (ϵ_2) is neglected for energies below the band gap. In many cases, especially for indirect bandgap materials, ϵ_2 may not abruptly decrease to zero. Instead, it exhibits a tail due to defects and intraband absorptions. The Tauc-Lorentz model calculates ϵ_2 based on the assumption of parabolic bands and a constant momentum matrix element [66].

The Cody-Lorentz model derives ϵ_2 assuming parabolic bands and constant dipole matrix element, resulting in a different expression near the band edge [67]. Three important differences are: (i) weak exponential absorption below the band gap, (ii) a modified joint density of states, and (iii) a restriction on the $\epsilon_1(\alpha)$ parameter, respectively. Cody-Lorentz model has been derived by Ferlauto et al., which combines a variable band edge function $G(E)$ and Lorentz oscillator expression $L(E)$ along with the Urbach absorption tail [68] and can be described as

$$\epsilon_2 = G(E).L(E) = \frac{(E-E_g)^2}{(E-E_g)^2+E_p^2} \times \frac{A\Gamma E E_0}{(E-E_0)^2+\Gamma^2E^2}, E > E_t \tag{2.7}$$

$$\epsilon_2(E) = \frac{E_tG(E_t)L(E_t)}{E} \times \exp\left(\frac{E-E_t}{E_u}\right), 0 < E \le E_t \tag{2.8}$$

where E, E_t, and E_0 are the photon energy, transition energy, and peak energy of the Lorentz oscillator, respectively. Γ is the width of the Lorentz oscillator and E_p is a weighting factor between the Cody and Lorentz part. When the photon energy is less than E_t, ϵ_2, the imaginary part of the dielectric function undergoes an exponential decay, which is the so-called Urbach tail [68], where E_u determines the rate of decrease in the Urbach tail with decreasing photon energies. This Urbach tail carries the information on the intraband transitions or transitions occurring at a lower energy than the optical bandgap due to doping or impurities. Especially for high k materials with a high band gap, the Cody-Lorentz model shows a higher accuracy (lower mean squared error MSE) compared to the Tauc-Lorentz model [69]. In this dissertation, the Cody-Lorentz model has been chosen to examine the optical properties of Al_2O_3/TiO_2 heterostructures near the absorption edge since it successfully incorporates the absorption phenomenon below 400 nm due to the presence of TiO_2 in the heterostructures.

The metals are differentiated from the other classes of materials in terms of the conduction of the free electrons. Paul Drude first explained the transport of electrons in metallic materials in 1900, commonly known as the Drude model [70]. This model formulates the relationship between the current density and the external electric field. It is a semi-classical approach that considers the collision of electrons. The electrons are assumed to move as free particles. The time duration and the path traveled between two successive collisions are termed as mean free time and mean free path. These assumptions lead to the following expression for current density

$$\vec{J} = \frac{n_d e^2 \tau}{m}\vec{E}, \tag{2.9}$$

where $\vec{J}$ is the current density, n_d is the number density of electrons, e is the electronic charge, m is the mass of electron, τ is the mean free time between two collisions, and $\vec{E}$ is the external electric field. This expression leads to the definition of conductivity σ, where

$$\sigma = \frac{n_d e^2 \tau}{m}. \tag{2.10}$$

Further, by applying a time varying electric field and solving the Maxwell equations, the complex dielectric function $\epsilon(\omega)$ of metal can be described as the following,

$$\epsilon(\omega) = 1 + \frac{i\sigma}{\omega\epsilon_0}, \tag{2.11}$$

where ϵ_0 is the free space dielectric constant. To understand the metal-dielectric heterostructures, a combined approach has been implemented. The absorption spectra of materials contain certain peaks corresponding to the resonance frequencies of the system. This means the material has a significantly higher absorption probability at those resonance wavelengths, rather than any other non-resonant conditions. Oscillator models are useful for describing resonance conditions with only a few parameters, e.g., the position, amplitude, and broadening of the absorption peak. The oscillators can be symmetric around the resonances, whereas the asymmetric oscillators describe materials with optical bandgap [71, 72].

Therefore, to elucidate optical constants of the Ir/Al_2O_3 heterostructures discussed in this dissertation, a combination of the Drude model along with a set of Lorentz oscillators has been implemented. The Drude term accounts for the contribution of free charge carrier from the metallic part, whereas the Lorentz oscillators incorporate the bound electron descriptions from the dielectric side. The expression for the Drude-Lorentz oscillator model is as follows:

$$\epsilon(\omega) = \epsilon_\infty - \frac{\omega_p^2}{\omega^2 + i\omega\gamma_D} - \sum_i \frac{\Omega_{p,i}^2}{(\omega^2 - \omega_i^2) + i\omega\gamma_{L,i}} \tag{2.12}$$

where ϵ_∞ is the high frequency limit of dielectric function, ω_p is the plasma frequency and γ_D is the damping factor of the Drude contribution. Ω_p is the oscillator strength, ω_i is the resonance frequency of each oscillator, and $\gamma_{L,i}$ is the damping of Lorentz oscillators, respectively.

2.2 Effective medium approximation

The effective medium theory has been significantly applied to solve wide range of problems in physics and materials engineering. In this dissertation, various effective medium approximation (EMA) approaches have been implemented to simulate the optical constants of atomic scale heterostructures.

In order to describe a mixture of materials, the general mixing formula depending on the properties of the constituents has the following form [73, 74] :

$$\frac{\epsilon_{eff} - \epsilon_h}{\epsilon_h + (\epsilon_{eff} - \epsilon_h)L} = \sum_j f_j \frac{\epsilon_j - \epsilon_h}{\epsilon_h + (\epsilon_j - \epsilon_h)L} \tag{2.13}$$

where ϵ_{eff} is the effective dielectric function of the mixture, ϵ_h corresponds to the host medium (e.g., the dominant constituent), f_j is the volume fill fraction of the inclusion material and ϵ_j is the j^{th} inclusion (e.g., some pores, voids, or some other material) of the mixture. L is the depolarization factor, which is in general a real number representing the morphology of the constituents or the assumed shape of the inclusions (spheres, needles, etc.) [73]. Several models based on this macroscopic mixing formula were developed:

- Lorentz-Lorenz approach: The Lorentz–Lorenz equation is derived from the Clausius–Mossotti relation, which relates the dielectric constant of spherical particles with their density N and their polarizability α and has the following form,

  $$\frac{\epsilon - 1}{\epsilon + 2} = \frac{1}{3}\sum_j N_j \alpha_j . \tag{2.14}$$

  In general, this assumes vacuum as the host medium, consequently, $\epsilon_h = 1$ and the corresponding mixing formula becomes

  $$\frac{\epsilon_{eff} - 1}{1 + (\epsilon_{eff} - 1)L} = \sum_j f_j \frac{\epsilon_j - 1}{\epsilon_h + (\epsilon_j - 1)L}. \tag{2.15}$$

  This model has found several applications in ellipsometric porosimetry studies and modelling of small scale surface roughness [73].

- Maxwell-Garnett (MG) approach: This aims to consider the material with the largest constituent fraction as the host, i.e., $\epsilon_h = \epsilon_l$. Standard MG approach assumes spherical material inclusions inside a host matrix with a particular volume fill fraction f in quasi-static and dipolar approximation [75, 76]. However, particle-particle interactions are not considered, which leads to lose its validity with increasing fill fraction (for instance, $f \geq 50\%$).

  $$\frac{(\epsilon_{eff} - \epsilon_l)}{\epsilon_l + (\epsilon_{eff} + \epsilon_l)L} = \sum_{j=l} f_j \frac{\epsilon_j - \epsilon_l}{\epsilon_l + (\epsilon_j - \epsilon_l)L} \tag{2.16}$$

  Maxwell-Garnett approximation simulates the permittivity for a uniform mixture consisting of the constituents (host and inclusion). While investigating the optical constants of Ir/Al_2O_3 heterostructures, the MG approach was a method of choice. Considering iridium (Ir) nanoparticles as spherical inclusion in Al_2O_3 matrix, a depolarization value of 0.33 has been incorporated.

- Bruggeman (BG) approach: This approach does not consider any distinction between the composite materials into a host and an inclusion material, or in other words, the system is considered as a homogeneous mixture of the constituents, i.e, an effective medium as a whole [77, 78]. Therefore, Bruggeman's theory allows for understanding more complex mixtures of the constituents without assuming a particular shape.

$$\sum_j f_j \frac{\epsilon_j - \epsilon_{eff}}{\epsilon_{eff} + (\epsilon_j - \epsilon_{eff})L} = 0 \qquad (2.17)$$

  While investigating the Al_2O_3/TiO_2 heterostructures, Bruggeman's approach has been implemented to determine the refractive index spectra of the ultrathin dielectric based hetero-interfaces. The corresponding complex refractive index $\tilde{n} = n + ik$ is obtained from $\tilde{n} = \sqrt{\epsilon_{eff}}$.

Thus, the EMA models based on Bruggeman and Maxwell-Garnett approaches have enabled the estimation of the optical properties of heterostructures at atomic scales. This essentially becomes an inevitable perspective for designing new materials for targeted applications.

2.3 Quantum confined structures

Low dimensional nanomaterials have been extensively explored due to the possibility of tailoring and enhancing their functionalities as compared to their bulk counterparts [1, 2]. Electron confinement phenomena in solids with restricted geometry like quantum dots, quantum wires, or quantum wells emerges into the modification of optical and electronic properties. These phenomena are direct consequences of the wave properties of electrons. The variation of electronic density of states depending on size of the nanostructures is discussed further.

The density of states (DOS) $\rho(E)$ is defined as the number of electron states $N(E)$ per unit volume per unit energy (E), which means the number of states at a particular energy level that electrons are allowed to occupy. The general form of the electron DOS is given by the following expression:

$$\rho(E) = \frac{dN(E)}{dE}. \tag{2.18}$$

In order to deduce Eq. 2.18 for the quantum confined structure, the effective mass approximation approach has been considered. The electrons in a crystal are not ideally free, instead, they interact with the periodic potential of the lattice. The effective mass is the mass experienced by the electrons inside the solid. Therefore, the wave-particle motion of electrons in a lattice cannot be expressed by the equation of motion of electrons in free space. By taking (i) the influence of the lattice, (ii) the shape of energy bands in three-dimensional reciprocal momentum (κ)-space, (iii) the appropriate average over the various energy bands into account, the effective mass ($m^{\square}$) of an electron in a band with a given (E, κ) relationship can be expressed as,

$$m^{\square} = \frac{\square^2}{\frac{d^2E}{d\kappa^2}}, \tag{2.19}$$

where $\square = \frac{h}{2\pi}$ and h is the Planck's constant, $h = 6.626 * 10^{-34}$ J.s. This effective mass is inversely proportional to the electron mobility μ_e at a particular band, and can be described as,

$$\mu_e = \frac{e\tau_c}{m^{\square}}, \tag{2.20}$$

where, τ_c is the mean free time of electrons, i.e., the time between two successive collisions. Quantum confined structures are precisely engineered nanostructures where electrons and holes are confined in any of one, two, or three directions. Table 2.1 summarizes the three basic types of quantum confined structures depending on the number of confined dimensions. A schematic representation of such structures is illustrated in Figure 2.1.

Quantizing effects start impacting as the dimension of the structures decreases below a certain length-scale, which stems from the change in the functional form of electronic DOS [1,2]. Simultaneously, electron mobility is restricted depending on

Table 2.1: Types of quantum confined structures and information on the electron density of states (DOS).

Structure	Quantum confinement	Number of free dimensions	Electron DOS (proportional to)
Bulk	none	3	$E^{\frac{1}{2}}$
Quantum well	1-D	2	E^{0}
Quantum wire	2-D	1	$E^{-\frac{1}{2}}$
Quantum dot	3-D	0	discrete

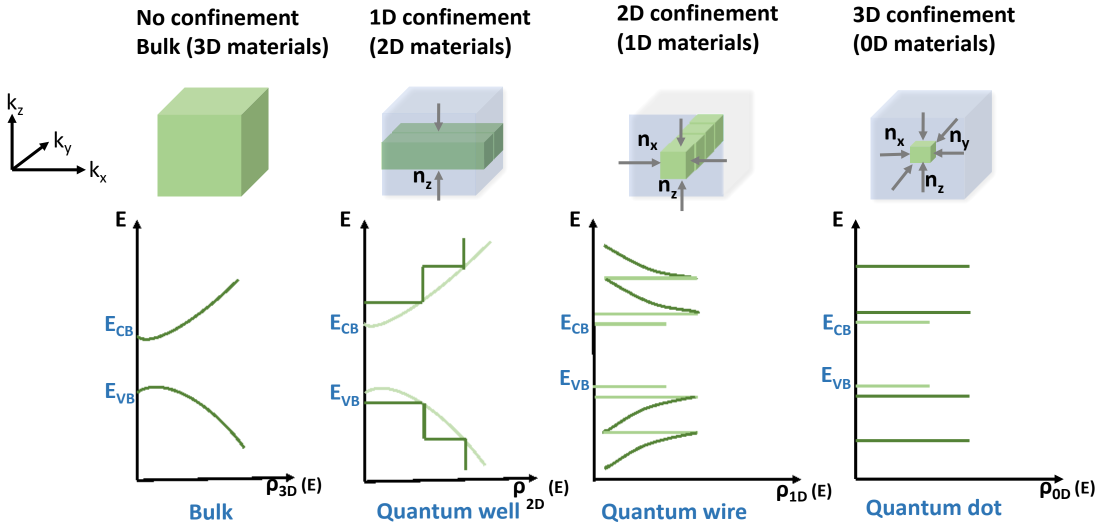

Figure 2.1: Schematic illustration of confinement dimension and functional form of the density of states in 1D, 2D, and 3D confined materials, recreated from reference [2].

the regime of confinement. The focus of this dissertation involves the quantum well based heterostructures. In this case, heterostructures are formed from different interfaces, e.g., a thin layer of a narrow bandgap material (well) is sandwiched between two layers of a relatively wider bandgap material (barrier), as illustrated in Figure 2.2. If the thickness of the well material is suficiently thin for exhibiting quantum effects, such band alignment can manifest quantizing structures. In order to have an estimation of such length scale, one could start with the Heisenberg's uncertainty principle. This principle establishes the impossibility of simultaneous

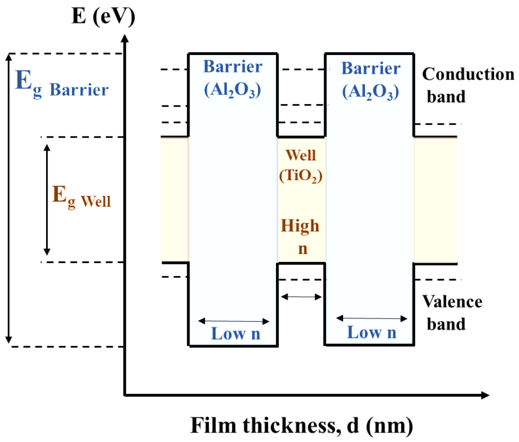

Figure 2.2: Schematic diagram of the quantum well-barrier heterostructure. An example is illustrated using Al_2O_3 and TiO_2 as the barrier and well materials, respectively.

determination of the position and momentum of a particle at the same state to an infinite precision. The measurement will always possess an inherent uncertainty of the order of $\hbar$, which is given by:

$$\Delta x \Delta p_x \approx \hbar, \tag{2.21}$$

where, Δx and Δp_x are the uncertainty in position and corresponding momentum, respectively. For instance, a particle having a mass m, confinement in x direction, the confinement energy E_{conf} can be written as,

$$E_{conf} = \frac{\Delta p_x^2}{2m} \approx \frac{\hbar^2}{2m\Delta x^2}. \tag{2.22}$$

In order to ensure the quantum confinement effect, this confinement energy has to be comparable to or greater than the kinetic energy of the particle due to its thermal motion, which is mathematically expressed as,

$$\frac{\hbar^2}{2m\Delta x^2} \geq \frac{1}{2}k_B T, \tag{2.23}$$

where, k_B is the Boltzmann constant and T is the temperature of the corresponding particle. This indicates that the quantum size effects will be significant if the following condition is satisfied,

$$\Delta x \leq \sqrt{\frac{\hbar^2}{2mk_BT}}, \tag{2.24}$$

which eventually leads to the famous de Broglie equation as given below,

$$\lambda_{deBroglie} \approx \frac{h}{p_x}. \tag{2.25}$$

This precisely explains the need of Δx or the thickness of the quantum well to be comparable to or smaller than the de Broglie wavelength in order to obtain quantizing effects. For having a quantitative idea, at room temperature, with a semiconductor having $m_e^* = 0.1m_0$, where m_0 is the rest mass of the electron, the thickness Δx has to be $\leq$ 5 nm. Furthermore, this structure must be repeated with very high precision by employing eficient atomic scale processing techniques. In order to model the energy states of such heterostructures or superlattices, the Schrödinger equations based on the Kronig-Penny model has been applied [53, 54, 79]. In general, semiconductors possess well defined band structures as a consequence of explicit crystal structures. However, the potential well models used to describe the crystalline semiconductors can successfully describe amorphous dielectric heterostructures to a great extent, considering the short range order of amorphous materials and assuming an idealized band structure in the theoretical simulations. The deposited dielectrics with amorphous structures, which do not have a perfect band structure may lead to a certain extent of mismatch between the quantum mechanical theory and experimental results.

This dissertation allows to experimentally determine the influence of the thickness Δx on the optical bandgap in amorphous all-dielectric heterostructures and on the dispersion of metal-dielectric heterostructures. Here, the effects of interfaces and intermixing have been observed. The formation of chemical bonds between the different materials at the interfaces has been evaluated. This work involves growing superlattices using two technologically relevant dielectrics, viz., Al_2O_3 and TiO_2. Further, the study is extended to HfO_2/SiO_2 heterostructures.

2.4 Multilayer interference coatings

Thin film interference coatings are essential for the advancements of optical system design. Optical interference coatings refer to the films which have thicknesses comparable to the wavelength of incident light. In order to understand thin film interference multilayers, light propagation at a single interface needs to be explained. Let us consider a flat interface, the adjacent media are assumed to be optically homogeneous, isotropic, and non-magnetic. Figure 2.3 illustrates a case where an electromagnetic plane wave is incident at an angle of incidence of φ, where I_i is the incident intensity, $E^{(i)}$ is electric field strength and $e^{(i)}$ is the corresponding unit vector. The reflected intensity is I_r and the electric field strength is $E^{(r)}$, respectively. The incident medium and medium of refraction have complex refractive indices of $\tilde{n}_1$ and $\tilde{n}_2$, respectively. The angle of refraction in the second medium is γ. Similarly, I_t and $E^{(t)}$ denote the intensity of the transmitted wave and electric field strength. $H^{(i)}$, $H^{(r)}$, and $H^{(t)}$ stand for the incident, reflected, and transmitted magnetic field strength. The continuity equations of the tangential components of electric and magnetic field strength vectors obtained from

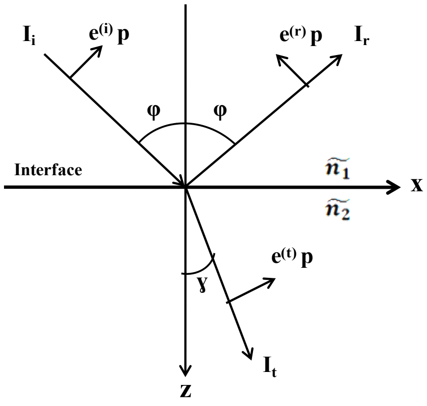

Figure 2.3: Schematic diagram of propagation of light at the interface of two media, recreated from reference [80].

Maxwell’s boundary conditions can be expressed as follows:

$$E_x^{(i)} + E_x^{(r)} = E_x^{(t)} \tag{2.26}$$

$$E_y^{(i)} + E_y^{(r)} = E_y^{(t)} \tag{2.27}$$

$$H_x^{(i)} + H_x^{(r)} = H_x^{(t)} \tag{2.28}$$

$$H_y^{(i)} + H_y^{(r)} = H_y^{(t)} \tag{2.29}$$

The Fresnel coeficients of reflectance (r_p and r_s) and those for transmittance (t_p and t_s) for both p and s-polarizations can be obtained from the set of equations Eq. 2.26 to Eq. 2.29 [81] (a detailed derivation can be found in reference [80]). The Fresnel coeficients are given by:

$$r_p = \frac{\tilde{n}_2 \cos\varphi - \tilde{n}_1 \cos\gamma}{\tilde{n}_2 \cos\varphi + \tilde{n}_1 \cos\gamma} \tag{2.30}$$

$$t_p = \frac{2\tilde{n}_1 \cos\gamma}{\tilde{n}_2 \cos\varphi + \tilde{n}_1 \cos\gamma} \tag{2.31}$$

$$r_s = \frac{\tilde{n}_1 \cos\varphi - \tilde{n}_2 \cos\gamma}{\tilde{n}_1 \cos\varphi + \tilde{n}_2 \cos\gamma} \tag{2.32}$$

$$t_s = \frac{2\tilde{n}_1 \cos\varphi}{\tilde{n}_1 \cos\varphi + \tilde{n}_2 \cos\gamma}. \tag{2.33}$$

The p-polarization stands for $\vec{E}$ field parallel to the plane of incidence ((x-z) plane), while s-polarization corresponds to $\vec{E}$ field perpendicular to the plane of incidence ((x-z) plane)). Using these equations (Eq. 2.30 to Eq. 2.33), the reflectance R and transmittance T (for non-absorbing medium) at the interface can be calculated as follows:

$$R = |r|^2 \tag{2.34}$$

$$T = 1 - R = \frac{\mathrm{Re}(\tilde{n}_2 \cos\gamma)}{\mathrm{Re}(\tilde{n}_1 \cos\varphi)} |t|^2. \tag{2.35}$$

Re indicates the real part of the corresponding quantity. In the case of a normal angle of incidence with real refractive indices, the reflectance for both polarizations can be expressed as:

$$R = \left(\frac{n_1 - n_2}{n_1 + n_2}\right)^2. \qquad (2.36)$$

For a simplified picture, a thin film of refractive index n_2 deposited on a planar substrate having a refractive index n_3 can be visualized as a plane-parallel plate, as illustrated in Figure 2.4.

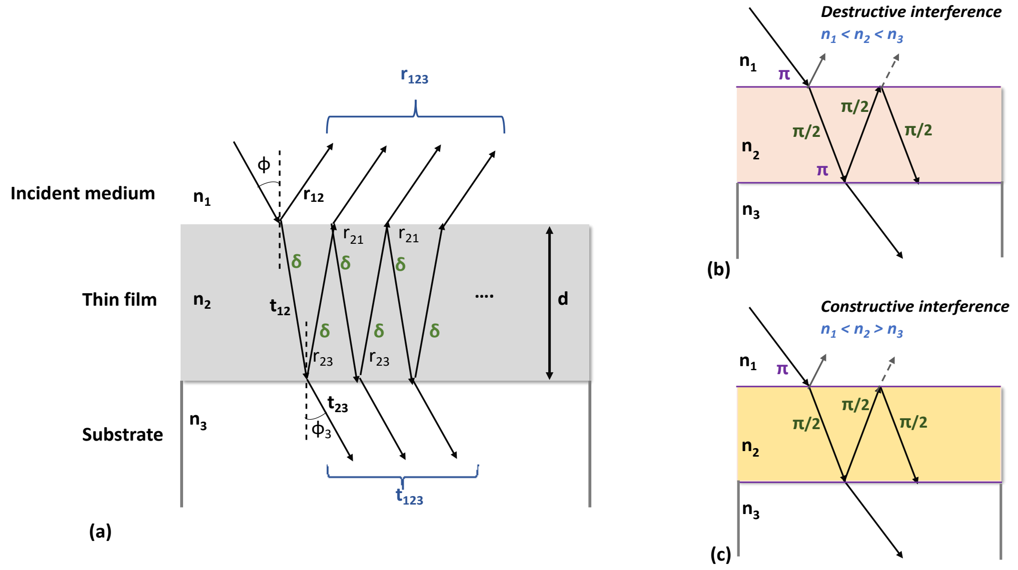

Figure 2.4: (a) Schematic diagram of propagation of light in an 'incident medium/film/substrate' system, (b) conditions for destructive interference, and (c) conditions for constructive interference.

As long as the geometrical thickness of the film d is greater than the coherence length l_{coh} of the incident light, no interference effect can be noticed. When the thickness becomes comparable to the incident wavelength, the phase relationships of the partially reflected beams come into play, leading to interference effects. The optical thickness is known as the product $n_2.d$. The phase shift due to each of the partial reflections can be expressed using these geometric considerations shown in Figure 2.4 and is given by:

$$\delta = \frac{\omega}{c} d\tilde{n}_2 \cos\varphi = \frac{\omega}{c} d \sqrt{\tilde{n}_2^2 - \tilde{n}_1^2 \sin^2\varphi} \qquad (2.37)$$

where, δ is the phase shift of the light after passing through the film once, λ is the wavelength of the incident light, $\tilde{n}_2$ is the refractive index of the film material, d is the geometrical thickness of the film, ω is the frequency of the incident beam, and c is the speed of light in vacuum. Consequently, the reflectance R and transmittance T could be obtained as,

$$R = |r_{123}|^2 \tag{2.38}$$

$$T = \frac{\mathrm{Re}(\tilde{n}_3)\cos\varphi_3}{\tilde{n}_1\cos\varphi})|t_{123}|^2 \tag{2.39}$$

Two important types of single layer films depending on the optical thickness, which are widely applied for designing optical thin film systems: (i) quarter wave optical thickness and (ii) half wave optical thickness. If the optical thickness of the layer is one quarter of the wavelength ($\lambda/4$) of the incident light or an odd multiple of ($\lambda/4$), the phase difference of the partially reflected beams is π or odd multiple of π, since the beam is refracted twice. Assuming real refractive indices, and normal angle of incidence, the phase relationship satisfies as follows:

$$\delta = \frac{\pi}{2}, e^{2i\delta} = -1 \tag{2.40}$$

$$\frac{\pi}{2} = \frac{\omega}{c} d \sqrt{n_2^2 - n_1^2 \sin^2(0)} \tag{2.41}$$

$$\frac{\pi}{2} = \frac{2\pi}{\lambda} n_2 d \quad \rightarrow \quad n_2 d = \frac{\lambda}{4} \tag{2.42}$$

As demonstrated in Figure 2.4(b), the first reflected beam will have a phase difference of π with respect to the incident beam due to the reflection from an optically rarer to optically denser medium. The second reflected beam resulting from two multiple reflections in the film will be in 2π phase difference with respect to the incident beam (due to another π phase shift at the film/substrate interface as $n_2 < n_3$). A phase shift of π causes maximum influence on the resultant reflection and transmission spectra. Hence, if $n_2 < n_3$, this quarter wave optical thickness (QWOT) of the layer extinguishes the resultant reflected intensity. These QWOT layers are the basic building blocks of most of the optical layer systems. Whereas in the case of $n_2 > n_3$ (see Figure 2.4(c)), there is no extra phase shift of π at the film/substrate interface leading to constructive interference; i.e., resultant reflected intensity is maximum.

On the other hand, when the optical thickness of the layer is half of the wavelength ($\lambda/2$) of the incident light or an odd multiple of $\lambda/2$, the phase difference of the partially reflected beams is 2π or even multiple of π. The phase relationship becomes:

$$\delta = \pi, e^{2i\delta} = +1 \tag{2.43}$$

$$\pi = \frac{\omega}{c} d \sqrt{n_2^2 - n_1^2 \sin^2(0)} \tag{2.44}$$

$$\pi = \frac{2\pi}{\lambda} n_2 d \quad \rightarrow \quad n_2 d = \frac{\lambda}{2} \tag{2.45}$$

This is called half wave optical thickness (HWOT), which is optically inert, i.e., it has no influence on the resultant reflectance or transmittance. Additionally, for demonstrating a single layer antireflection coating, another condition of the refractive index needs to be fulfilled, assuming real refractive indices and normal angle of incidence.

$$r_{12} + r_{23} e^{i\frac{\pi}{2}} = 0 \quad \rightarrow \quad r_{12} = r_{23} \quad \rightarrow \quad n_2 = \sqrt{n_1 n_3} \tag{2.46}$$

More than 50% of optical coatings are made for antireflection purposes [82]. Antireflective multilayer interference coatings are based on destructive interference of the reflected light so that the reflected intensity can be reduced to nearly zero, as shown in Figure 2.4(b).

To demonstrate an antireflection coating on glass substrate, the simplest coating example can be QWOT layer of MgF_2 (n_f = 1.38) on a glass substrate (n_s = 1.52), where the incident medium is considered to be air. Theoretically, a material with refractive index n_f of 1.23 is required to extinguish the reflected light from the glass substrate (using Eq. 2.46). However, no solid material with n_f of 1.23 is available in nature making MgF_2 as the suitable choice having the closest refractive index to the required value. Using MgF_2 as a choice of material, for normal incidence, reflectance can be reduced from 4.3% to 1.2%; calculated using the Fresnel equation as in Eq. 2.36. Therefore it is clear that, for further complex applications, precise requirements, and broadband performances, multilayer designs with more than one material are essential in practice. In order to simulate the reflection and transmission coeficient of a QW stack on a substrate, which is assumed to be infinitely thick (i.e., no rear surface), the following matrix formalism is applied [73, 80, 81]. For s- and p- polarizations, a matrix $\hat{M}$ is defined for a single layer film:

$$\text{s-pol.}: \hat{M}_s = \begin{pmatrix} \cos(k_0\tilde{n}d\cos\Psi) & -\frac{i}{\tilde{n}\cos\Psi}\sin(k_0\tilde{n}d\cos\Psi) \\ -i\tilde{n}\cos\Psi\sin(k_0\tilde{n}d\cos\Psi) & \cos(k_0\tilde{n}d\cos\Psi) \end{pmatrix} \tag{2.47}$$

$$\text{p-pol.}: \hat{M}_p = \begin{pmatrix} \cos(k_0\tilde{n}d\cos\Psi) & -\frac{i\tilde{n}}{\cos\Psi}\sin(k_0\tilde{n}d\cos\Psi) \\ -i\frac{\cos\Psi}{\tilde{n}}\sin(k_0\tilde{n}d\cos\Psi) & \cos(k_0\tilde{n}d\cos\Psi) \end{pmatrix} \tag{2.48}$$

According to that, the characteristic matrix $\hat{M}$ of a stack consisting of X layers would be the product over the matrices of all single layers, and thus:

$$\hat{M}_{stack} = \prod_{i=1}^{X} \hat{M}_i(d_i) = \begin{pmatrix} m_{11} & m_{12} \\ m_{21} & m_{22} \end{pmatrix}. \tag{2.49}$$

The reflection and transmission coeficients can be calculated from the matrix elements, which have the form as expressed below:

$$r^s = \frac{(m_{11} + m_{12}\tilde{n}_s\cos\varphi_s)n_1\cos\varphi - (m_{21} + m_{22}\tilde{n}_s\cos\varphi_s)}{(m_{11} + m_{12}\tilde{n}_s\cos\varphi_s)n_1\cos\varphi + (m_{21} + m_{22}\tilde{n}_s\cos\varphi_s)} \tag{2.50}$$

$$t_s = \frac{2n_1\cos\varphi}{(m_{11} + m_{12}\tilde{n}_s\cos\varphi_s)n_1\cos\varphi + (m_{21} + m_{22}\tilde{n}_s\cos\varphi_s)} \tag{2.51}$$

$$r_p = \frac{(m_{11} + m_{12}\frac{\cos\varphi_s}{\tilde{n}_s})\frac{\cos\varphi}{n_1} - (m_{21} + m_{22}\frac{\cos\varphi_s}{\tilde{n}_s})}{(m_{11} + m_{12}\frac{\cos\varphi_s}{\tilde{n}_s})\frac{\cos\varphi}{n_1} + (m_{21} + m_{22}\frac{\cos\varphi_s}{\tilde{n}_s})} \tag{2.52}$$

$$t_p = \frac{\frac{2\cos\varphi}{n_1}}{(m_{11} + m_{12}\frac{\cos\varphi_s}{\tilde{n}_s})\frac{\cos\varphi}{n_1} + (m_{21} + m_{22}\frac{\cos\varphi_s}{\tilde{n}_s})} \tag{2.53}$$

Various thin film interference systems (for instance, antireflection coatings, mirrors, filters, beam splitter, etc.) with different optical properties require multilayer stacks, which can be designed by proper choice of materials and optimizing individual layer thicknesses. As evident from the complexity of the above set of equations, these calculations are currently implemented by using dedicated optical thin film design software, e.g. OptiLayer, Film Wizard, etc. Within the scope of this dissertation, two antireflection coatings are designed and demonstrated on fused silica glass substrates using multilayer stacks of Al_2O_3/TiO_2 heterostructures and SiO_2, which are discussed in Chapter 5.3.

2.5 Nonlinear optical materials

Nonlinear optical effects refer to the nonlinear interaction of light with matter [83, 84]. Such nonlinear properties of materials are very useful in a variety of applications, ranging from optical frequency generation, parametric amplification of light, spectroscopy, and imaging to sensing applications [84, 85]. Commercially available crystals [86,87], such as potassium dihydrogen phosphate (KDP) [88], lithium niobate ($LiNbO_3$) [89], lithium borate (LBO) [90], barium borate (BBO) [89] and silicon or gallium based superlattices [91,92] show decent optical nonlinearities. However, these crystals are difficult to integrate into semiconductor and photonic platforms. Due to the continuous shrinking of device sizes and the use of 3D photonic architecture, the search for alternative nonlinear optical materials has become essential as compared to bulk crystals. A promising alternative approach by designing new optical metamaterials has emerged. The list includes dielectric nanolaminates [93–97], metal-dielectric heterostructures [58,98], epsilon near zero (ENZ) materials [98,99], functional 2-dimensional materials [100,101], and metasurfaces [102,103]. These materials manifest potential optical nonlinearities, e.g., in second, third, or higher harmonic generations.

The polarization in a material is considered as the origin of nonlinearity. The total polarization $\vec{P}$ of a material is the sum of linear ($\vec{P}_L$) (which is a linear function of the electric field) and nonlinear ($\vec{P}_{NL}$) contributions of polarization, i.e., $\vec{P} = \vec{P}_L + \vec{P}_{NL}$. The polarization $\vec{P}$ in a material can be expressed as [84],

$$\vec{P} = \epsilon_0\chi^{(1)}\vec{E} + \epsilon_0\chi^{(2)}\vec{E}\vec{E} + \epsilon_0\chi^{(3)}\vec{E}\vec{E}\vec{E} + ... \tag{2.54}$$

The corresponding general expression for the polarization is given below,

$$P_i = \epsilon_0 \chi^{(1)}_{ij} E_j + \epsilon_0 \chi^{(2)}_{ijk} E_j E_k + \epsilon_0 \chi^{(3)}_{ijkl} E_j E_k E_l + ... \tag{2.55}$$

In the scalar form, the above expression can be simplified as follows,

$$P = \epsilon_0 \chi^{(1)} E + \epsilon_0 \chi^{(2)} E^2 + \epsilon_0 \chi^{(3)} E^3 + ... \tag{2.56}$$

The term $\epsilon_0 \chi^{(1)} \vec{E}$, containing $\vec{E}$ is the linear contribution, whereas the higher order dependence of $\vec{E}$ denotes the nonlinear effect. The higher order effects are relatively weak and have much lower intensity, as $\chi^{(1)} >> \chi^{(2)} or \chi^{(3)}$. Therefore it is essential to impose a very strong excitation electric field $\vec{E}$ to detect the nonlinear effects. As a consequence, the experimental detection of harmonic generation has only been possible after the invention of laser due to its intense coherent radiation. Basically, as $\vec{E}$ is very strong, the corresponding potential in which the electrons in the material are oscillating will not remain as harmonic oscillator, rather becomes anharmonic in nature. The optical nonlinearities can be classified based on their dependence on the order of χ.

- Second harmonic generation

In this section, the second harmonic generation (SHG) phenomenon based on the $\chi^{(2)}$ of a material will be discussed. SHG is a second order nonlinear optical process. For a material with second order nonlinearity, when a strong electric field $\vec{E}$ with frequency ω is launched into the material, it will generate another frequency, which is 2ω. In other words, if the incident light has a wavelength λ, the output intensity will contain both λ and $\lambda/2$ wavelengths.

Figure 2.5 illustrates the schematic diagram of SHG phenomenon from a nonlinear optical material. Consequently, the nonlinear polarization field, i.e., electric dipoles will vibrate with frequency 2ω. This will generate another field in the material which will vibrate with a frequency of 2ω. Exemplary, if the material is excited with a infrared laser of 1064 nm wavelength, SHG enables to create a green-coloured light of wavelength around 532 nm at the output. The term in

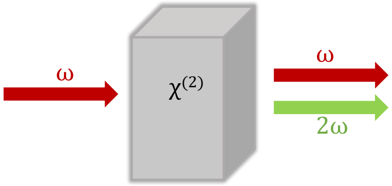

Figure 2.5: Schematic illustration of second harmonic generation (SHG) from a material having second order susceptibility $\chi^{(2)}$, where ω is the pump frequency and 2ω is the frequency of the generated second harmonic wave.

the expression $P_{NL} = \epsilon_0\chi^{(2)}\vec{E}\vec{E}$ governs the SHG response of a material. This indicates the contribution from the dipole term. Upon further expansion into multipole components, the expression becomes as follows,

$$P_{NL} = \epsilon_0\chi_D^{(2)}\vec{E}\vec{E} - \epsilon_0\vec{\nabla}.(\chi_Q^{(2)}\vec{E}\vec{E}) + \frac{\epsilon_0 c}{i\omega}\vec{\nabla}\times(\chi_M^{(2)}\vec{E}\vec{E}) + \dots \qquad (2.57)$$

The term with $\chi_D^{(2)}$ is from the electric dipole contribution. The second and third terms in the above expression contain electric quadrupole tensor and magnetic dipole, respectively. These terms are proportional to the spatial derivative of the incident electric field. Since the polarization in second order nonlinear effect varies quadratically with the incident field, the output SHG power is quadratically proportional to input pump power. This implies that the conversion eficiency of SHG signal has a quadratic dependence on the incident intensity. In order to have higher eficiency, the energy transfer between the fundamental and second harmonic wave has to be as high as possible. This brings us to another important criterion for achieving the SHG effect, namely the phase matching condition. This condition is mathematically expressed as,

$$\Delta K = K_{2\omega} - 2K_{\omega} = \frac{2\omega}{c}(\sqrt{\epsilon_{2\omega}} - \sqrt{\epsilon_{\omega}}) \qquad (2.58)$$

where K is the wave vector, ω and 2ω are the fundamental and second harmonic frequencies, ϵ_{ω} and $\epsilon_{2\omega}$ are the dielectric constants at these frequencies, respectively and c is speed of light in vacuum. When $\Delta K = 0$, the phase matching condition is satisfied implying the phase velocities of the fundamental wave and SHG wave are the same. This indicates that the SHG power converts most efficiently under this condition. If the condition is not met, i.e., $\Delta K = 0$, the conversion eficiency is lower. However, it is indeed critical to obtain complete phase matching in the readily available nonlinear crystals due to large dispersion as well as long propagation length. This situation leads to a more lenient and practical concept of quasi phase matching. It uses a periodically poled crystal to ensure the phase shift between the pump and SHG waves, is less than 180° along the propagation length in the nonlinear material. Although the phase matching condition is not explicitly satisfied, the periodic poling enables continuous energy flow from the pump wave to the output SHG wave.

This stringent condition strongly demands for engineering new alternative materials, where the generation of SHG power will not rely on maintaining the phase matching condition. Sub-wavelength nanostructures, thin film based nanomaterials, nanolaminates, metasurfaces, and supperlattices have been gradually developed as potential new nonlinear optical materials, where the requirement of phase matching is inherently non-essential.

A very important aspect of the origin of SHG in nano or atomic scale materials is the contribution from the bulk and surface nonlinearities, respectively. Bulk nonlinearity stems from the bulk volume of the material, which is primarily dependent on the dipole contribution, as indicated in Eq. 2.57. The contributions of the multipole terms depend significantly on the symmetry of the optical medium. For instance, in a material with inversion symmetry, the dipole term of the susceptibility tensor $\chi_D^{(2)}$ leads to zero, which is the highest contributor to the SHG. Therefore, in general second and even order nonlinearities are only enabled in media having no inversion symmetry. Whereas, surface nonlinearities originate due to the symmetry breaking at the interface of two media. The discontinuity of individual material and the surface normal of the electric field at the interface result in a strong second order dipole electric field across the interface. This phenomenon instigates designing new materials which can generate promising surface second order nonlinearities, while being independent of the symmetry of properties of the bulk of the material.

The search for artificial nonlinear optical materials has in general experienced advances in recent years. A few studies have already been reported on demonstrating nonlinear optical metamaterials composed of thin multilayer dielectric systems prepared by atomic layer deposition (ALD) [93–96]. By creating thin interfaces of different materials (ABC type materials which break the symmetry at the interfaces, e.g., $Al_2O_3/TiO_2/HfO_2$ [94] or $TiO_2/Al_2O_3/In_2O_3$ [95] based nanolaminates), surfaces with tailored nonlinearities and substantial magnitude have been reported. Moreover, ALD can also be used to provide interfaces for the subsequent growth of intrinsically nonlinear materials. Based on the nanolaminate approach to control the crystallinity of ZnO [96], their nonlinearity has been enhanced. In a case study with ZnO/Al_2O_3 nanolaminates [96], the ZnO was manipulated to grow along the (002) crystalline orientation by employing an Al_2O_3 seed layer for every ≈ 9.5 nm of the ZnO film. The nanolaminate structure with an Al_2O_3 seed layer shows an increase in second order nonlinearity by nearly 40 times as compared to single layer ZnO film, due to improved crystallite orientation and size. This concept was later extended to photonic crystal nanostructures [104], utilizing the conformality of ALD technology. The layer by layer growth mode and precise composition control at nanoscale provided by ALD are instrumental to create artificial nonlinear optical materials suitable for photonic and end-of-the-line CMOS integration [95]. Additionally, 3D conformal growth of ALD technology enables it to integrate perfectly with high aspect ratio structures, e.g., gratings, waveguides, and microlens arrays.

In this dissertation, the potential of generating SHG wave in atomic scale metal-dielectric heterostructures based on Ir/Al_2O_3 has been experimentally investigated. Additionally, the impact of the inclusion of dielectric Al_2O_3 spacer layers in the heterostructures has been examined on enhancing the output SHG power as well as the laser induced damage threshold in comparison with pristine Ir nanoparticles.

Chapter 3

Experimental details

This chapter provides a basic outline of the atomic layer deposition (ALD) technique and its advantages over other deposition methods applied in optics. The importance of using plasma enhanced ALD is discussed. A brief specification of the PEALD equipments used during this dissertation work is given. This chapter concludes with the applied precursors and process parameters implemented while developing the thin layer systems.

3.1 Atomic layer deposition (ALD)

The novel technology of atomic layer deposition was developed independently by two groups. In 1965 in Russia, the technique was established by Aleskovskii and Kol'tsov in the name of 'molecular layering' [105, 106] and in 1974 in Finland for the fabrication of electroluminescent flat panel displays by Suntola and his colleagues under the name of 'atomic layer epitaxy' [106, 107]. Over the last two decades ALD has evolved to an indispensable coating technology enabling applications in various fields, for instance, thin film electroluminescence displays [107] in extreme environments, semiconductor devices [108, 109], gate dielectrics [110,111], energy technologies [112–115], and eventually for optical industries [116, 117], to name a few.

ALD is a very powerful chemical coating technology for producing conformal thin films with superior uniformity on various substrate architectures [118, 119], e.g., highly curved substrates [120,121]. Conformal coatings have been achieved on micro- and nanostructures with a very high aspect ratio of, e.g., 3000:1 in thermal ALD [122] and 60:1 using plasma-assisted ALD processes [123]. The superior 3D conformality is enabled due to the surface-controlled nature of ALD processes, rather than being source controlled as in the case of conventional physical vapour deposition (PVD) methods. ALD is based on self-saturating surface reactions of the precursors and surface species (e.g., -OH groups), where the gaseous metal-organic precursor and co-reactant (generally known as 'precursor') are successively and independently pulsed into the reaction chamber. ALD is a modified form of chemical vapor deposition (CVD) where the precursors are introduced to the reaction chamber successively in a cycle, separated by purging steps, and due to that any possible reaction between the precursors in the gas phase is prohibited.

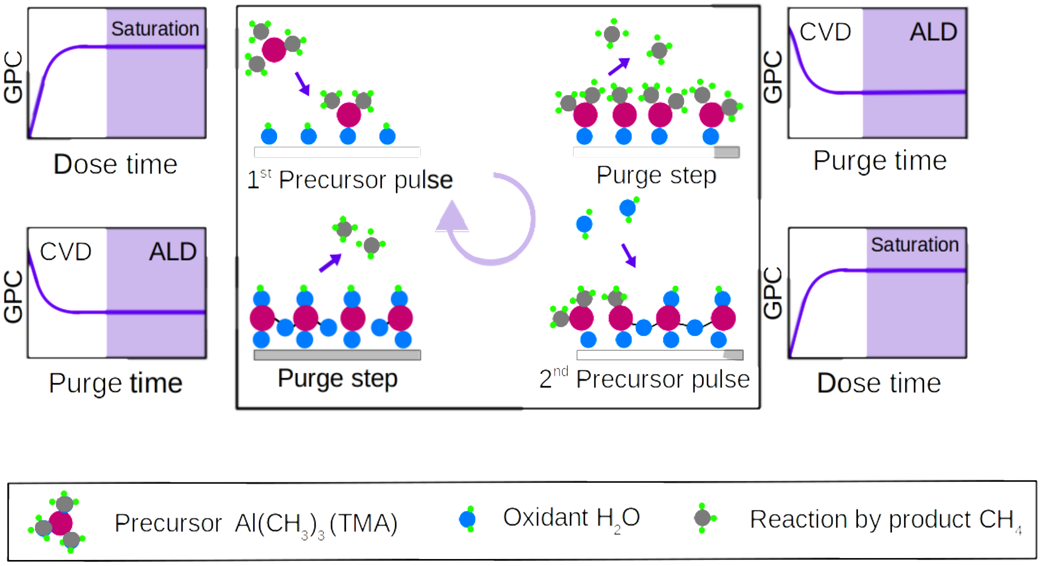

Figure 3.1: Schematic representation of thermal atomic layer deposition (ALD) of Al_2O_3 using trimethyl aluminum (TMA) and water (H_2O) as precursors.

An ALD process consists of typically four successive steps: (i) dosage (pulse) of the first precursor into the chamber, (ii) purge of the excess precursor molecules and reaction by-products by an inert gas, (iii) dosage (pulse) of the second precursor, (iv) purge of the excess molecules and reaction products out of the chamber by an inert gas. Figure 3.1 shows a schematic representation of a single ALD cycle of Al_2O_3 deposition with trimethyl aluminium (TMA) as the first precursor and

H_2O as the co-reactant.

(i) Precursor pulse or dose: The first precursor is pulsed into the chamber and the molecules will react with the available functional groups (generally, -OH) on the substrate surface. These surface reactions are self-limiting, which means the reaction stops once the functional groups on the substrate are consumed and generate reaction by-products. Hence, the precursor should not be reactive with the newly formed functional groups (e.g., $O\text{-}Al(CH_3)_2$) on the substrate surface.

(ii) Purging of excess first precursor and reaction by-products: The excess unreacted precursor and reaction by-products are purged out of the chamber by supplying inert gas (usually, Ar, N_2). A suficiently long purge time is essential to prevent any gas phase reactions between two precursors, otherwise, it may lead to unwanted parasitic CVD-type reactions.

(iii) Dose of second precursor: The second precursor or co-reactant (e.g., water, O_2 plasma, O_3 for growing oxides, or N_2 plasma for producing nitrides) is introduced to the chamber and it reacts with the surface-sites in a self-limiting manner and ideally produces a monolayer of the film and reaction by-products.

(iv) Purging of excess second precursor and reaction by-products: The reaction by-products and excess precursor are again removed from the chamber with the help of inert gas to separate the two ALD surface reactions. The ALD cycle can be repeated according to the desired film thickness. Due to this cyclic nature of the ALD technique, precise thickness control can be achieved down to nanometer or even sub-nanometer scales along with high reproducibility. Consequently, the precise thickness control nearly at the scale of single atomic layers enables fine tuning of compositions. This has been a very important factor in creating the atomic scale heterostructures investigated in this dissertation.

An ALD process is quantified by a growth per cycle (GPC) in Å/cycle, which indicates the thickness of deposited thin film per ALD cycle. The GPC is determined by depositing a thin film and is given by film thickness divided by the number of cycles. The growth is assumed to be the same on the substrate and thin film underlayers. Nucleation aspects are in general significant in the deposition of metals on dielectrics. The GPC depends mainly on the following factors: (i) size of

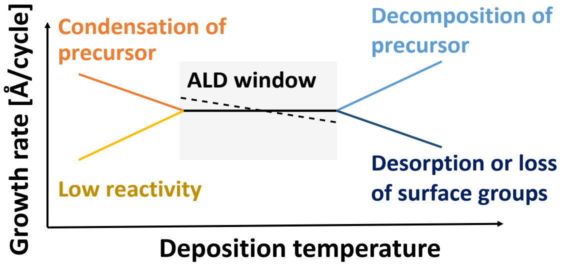

Figure 3.2: Schematic description of the atomic layer deposition (ALD) window indicating the variation of growth rate vs. deposition temperature, recreated from reference [124].

the precursor molecules, (ii) availability of functional groups on the substrate surface, (iii) duration of pulse and purge steps, and (iv) the deposition temperature. In general, ALD processes are described by an ALD window, which shows the variation of the growth rate with respect to the deposition temperature, as illustrated in Figure 3.2. For a certain temperature range, the GPC is ideally constant, which is referred to the stable ALD operation regime or ALD window. However, in reality, GPC is not constant over a broad range of temperatures due to the difference in number of surface groups depending on substrate temperature. With the increase in substrate temperature, the availability of surface sites decreases, and eventually, GPC decreases. On the other hand, when the temperature is very low, it may lead to precursor condensation or incomplete reactions due to low reaction rates at low temperatures. Along with that, thermal ALD process requires relatively longer pulse times such that the reactions can reach self-limiting growth (stable ALD operation regime), as indicated in Figure 3.3, and suficiently long purge times in order to remove excess H_2O or the by-products from the chamber (in case of thermal ALD using water). Consequently, the ALD cycle becomes relatively long and the deposition rate (nm/second) turns out to be low. This is one of the main reasons for applying plasma enhanced ALD (PEALD) processes, which enables high reactivity provided by the plasma radicals even at a lower temperature [45, 46]. Further, PEALD provides several potential advantages, for instance, improved material properties, increased choice of precursors, enhanced growth rate, good stoichiometric and composition control [45].

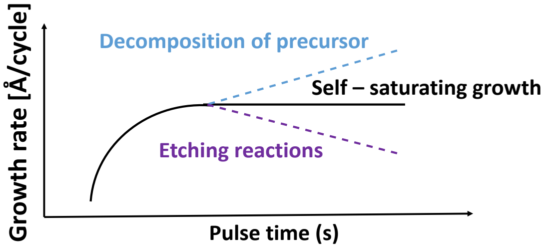

Figure 3.3: Schematic description of the variation of growth rate vs. pulse time in a typical atomic layer deposition (ALD) process, recreated from reference [124].

In this dissertation, single layers of Al_2O_3 and TiO_2 coatings are implemented in realizing Al_2O_3/TiO_2 based quantizing heterostructures using the PEALD method. A reasonable GPC has been achieved at a relatively lower deposition temperature of 100°C. For developing the metal-dielectric heterostructures of Ir/Al_2O_3, the corresponding stacks have been grown using thermal ALD at a higher deposition temperature of 380°C.

3.2 PEALD equipments and process parameters

(A) Oxford Instruments Plasma Technology ALD reactor (OpAL^{TM}): The dielectric thin films and corresponding heterostructures described in this dissertation have been grown using the commercially available OpAL^{TM} tool (Oxford Instruments Plasma Technology open load ALD reactor, Bristol, UK), as depicted in Figure 3.4. The reactor is equipped with an inductively coupled plasma (ICP) RF generator, operating at 13.56 MHz. Depositions can be performed by thermal activation (e.g., water as second precursor) and plasma enhanced ALD processes (e.g., remote inductively coupled O_2 plasma as second precursor). Figure 3.4 shows a schematic representation of the ALD chamber of the OpAL^{TM} tool. The ICP gate valve can be opened and closed as desired, which enables performing thermal ALD and PEALD processes in a single recipe. This is a significant flexibility for depositing multilayer systems, e.g., antireflection coatings, nanolaminates, heterostructures, etc., for research and development purposes. The maximum diameter of the substrates, which can be loaded in this research-purpose tool is about 216 mm. Substrates of a height up to 50 mm can be placed in the deposition

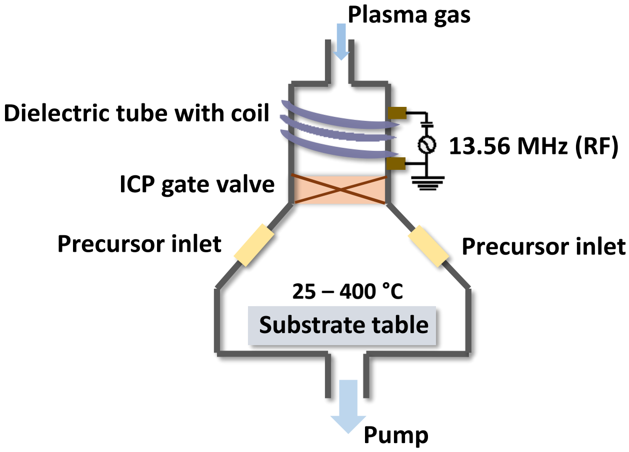

Figure 3.4: Schematics of the side view of ALD chamber of the OpAL^{TM} tool.

chamber, which allows for coating complex 3D substrates, however, only on 100 mm diameter area. The substrate temperature can be varied from 25°C to 400°C. The other important components of the tool are described in the following.

The basic chamber configuration is made up of three main inlet types: (i) metal-organic precursor inlet, (ii) water vapour inlet, and (iii) plasma inlet, respectively. The metal-organic precursors are stored in special bottles and connected through dose lines to the reaction chamber. Maximum of four precursor containers (lines D1-D4, as illustrated in Figure 3.5) can be fitted to this ALD tool, enabling the deposition of multilayer coatings of three different oxides, for example. The water inlet is termed as line D1. The dose valves (D1-D4) enable a fastest possible pulse time of 10 ms. The containers are equipped with heat jack-ets to control the temperature of the precursors and the valves to avoid precursor condensation. Thermal heating of chamber table and chamber walls is available. The water container is cooled to avoid condensation in the stainless steel connection pipelines. When a dose valve (D1-D4) is opened for a particular duration (for instance, 10 to 1500 ms), a certain amount of precursor vapour is released to the reactor. After closing the dose valve, the corresponding purge valve (P1–P4) is activated to remove the excess precursor and reaction by-products from the chamber. Oxygen O_2, and nitrogen N_2 are available as plasma gases and are delivered through the inductively coupled plasma (ICP) source situated at the top

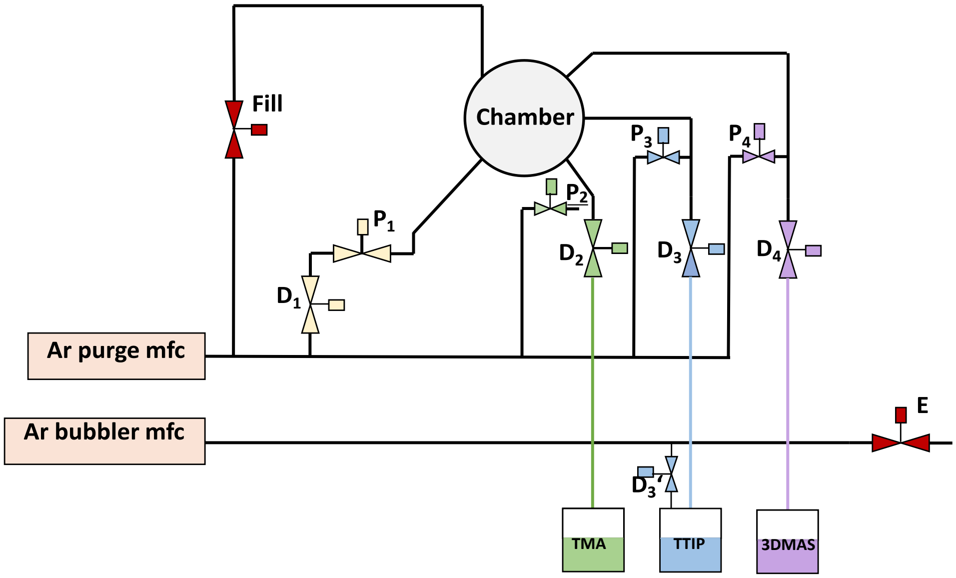

Figure 3.5: Schematic diagram of top view of the OpAL^{TM} chamber, D: dose, P: purge, E: exhaust line, TMA (trimethyle aluminum), TTIP (titanium isopropoxide), 3DMAS (tris(dimethyle)aminosilane).

of the chamber. The ICP consists of a dielectric tube with coil and gate valve, which converts incoming gas to plasma. O_2 plasma is used as the oxidizer for the deposition of oxides. Generally, Ar and N_2 are used as purging gas. If the vapour pressure of any precursor is very low, such that the precursor flux to the chamber is insuficient, the precursor container is equipped with a gas inlet (dose valve D3' in Figure 3.5) which performs the 'bubbling action'. Argon is used as a 'bubbler' or carrier gas to carry the precursor into the chamber, ensuring a uniform distribution of the precursor across the reactor. The flow rate (sccm, standard cubic cm per minute) of this carrier gas is controlled by a mass flow controller (MFC). The gas flow is connected through the bubbler line to obtain a higher precursor flux. In order to deposit TiO_2 films with titanium isopropoxide (TTIP) as precursor, the bubbler line needs to be activated. In the case of SiO_2 films, the precursor tris(dimethylamino)silane (3DMAS) has a suficient vapour pressure; however, significantly low reactivity. An extra 'hold precursor' step is included after the precursor pulse step in order to retain the precursor in the chamber for a longer time, providing it enough time for saturated self-limiting surface reactions to happen.

Precursors and process parameters:

The depositions of Al_2O_3/TiO_2 heterostructures have been performed at 100°C. Al_2O_3 and TiO_2 single layer films, as well as the compositions, are developed us-ing commercially available metal-organic precursors trimethyl aluminium (TMA) and titanium isopropoxide (TTIP), respectively along with oxygen (O_2) plasma as an oxidizer. Argon (Ar) has been used as the purging gas. The Si wafer and fused silica substrates were cleaned using a multi-stage ultrasonic assisted bath cleaning system (Elma Schmidbauer, Germany) containing alkaline solutions and surfactants, followed by washing in a water bath using deionized ultrapure water. The PEALD process parameters for Al_2O_3 and TiO_2 are listed in Table 3.1.

Table 3.1: Process parameters for growing single layer PEALD Al_2O_3, TiO_2, and SiO_2 films.

Material	Precursor pulse +(hold precursor) (s)	Purge (s)	O_2 plasma pulse (s)	Purge (s)
Al_2O_3	0.03	5	5	2.5
TiO_2	1.5	7	6	4
SiO_2	0.4 + (4)	5	3	3

The O_2 plasma parameters are 300 W plasma power, 50 sccm of O_2 gas flow while growing the dielectrics. The TTIP precursor has a relatively low vapour pressure. Therefore, 150 sccm of Ar has been used as a carrier gas to ensure the transportation of the precursor across the whole chamber during the TiO_2 layer deposition. A PEALD SiO_2 layer has been implemented as the top layer for designing the AR coating at 355 nm using 3DMAS and O_2 plasma as precursors. The PEALD process parameters for SiO_2 are tabulated in Table. 3.1. Due to the low reactivity of 3DMAS molecules, an additional 'hold precursor' step of 4 s has been introduced after the 3DMAS pulse for enabling self-saturating reactions.

(B) Picosun Oy, Sunale TM R-200 Advanced: For creating the metal-dielectric heterostructures consisting of Ir/Al_2O_3 interfaces, the Picosun® Sunale TM R-200 Advanced from Picosun Oy (Espoo, Finland) has been used. The tool allows the possibility of performing both thermal and PEALD processes. The plasma unit is capable of generating an inductively coupled plasma (ICP) of 3.2

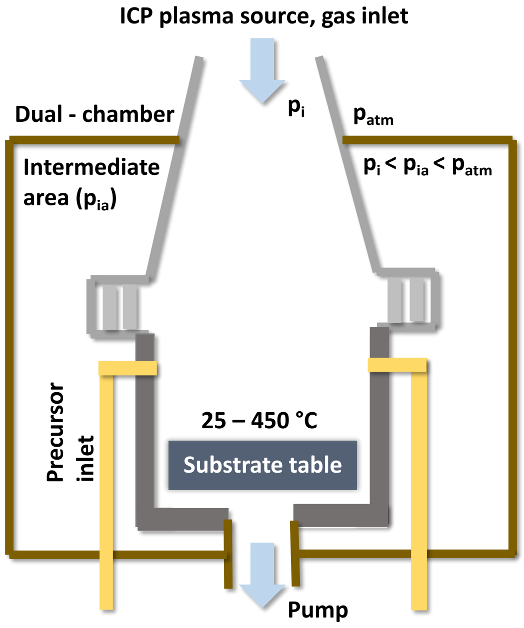

Figure 3.6: Schematics of the side view of ALD chamber of the Picosun R200 tool.

MHz with a maximum power of 3 kW. This ALD reactor can coat substrates having a diameter of up to 200 mm along with a substrate height of up to 50 mm. The substrate table and the chamber walls can be heated up to 450 °C due to the dual chamber design. The intermediate area as shown in Figure 3.6 is also pumped down, therefore, no sealing rings are required between the upper and lower chambers. Five metal-organic precursors and water container can be accommodated in the tool, which ensures depositions of multiple materials in a single ALD run. While coating metal and dielectric in the same process, one needs to be very careful regarding the contamination of the reaction chamber. Otherwise, it may lead to unpredictable growth behaviour. Owing to the separate precursor valves and inlets, the mutual contamination is minimized. In order to enable short, controlled precursor pulse times, fast-switching dose valves ($\geq$ 10 ms) are implemented. The temperatures of the precursor bottle, as well as, dose lines and valves are maintained by the heating jackets.

Precursors and process parameters

The substrate temperature for preparing Ir/Al_2O_3 heterostructures was kept at 380°C. This high temperature was essential for the growth of Ir layers since the reactivity of the iridium precursor molecules is low at lower temperatures. Furthermore, in order to grow the metal-dielectric compositions in a single ALD run within one recipe, the deposition of Al_2O_3 was also performed at 380°C. In this work, Ir layers are deposited using iridium acetylacetonate ($Ir(acac)_3$) and oxygen (O_2) gas as precursors along with N_2 purge in between. The $Ir(acac)_3$ precursor bottle was kept at 200°C. The corresponding process parameters are summarized in Table 3.2. The deposition process became relatively slow due to the relatively longer purge time after $Ir(acac)_3$ pulse to ensure complete removal of residual precursor and reaction by-products along with no blistering effect, as reported in previous literature [125].

Table 3.2: Process parameters for growing single layer ALD Ir and Al_2O_3 coatings.

Material	Precursor pulse (s)	Purge (s)	Co-reactant pulse (s)	Purge (s)
Ir	6	60	2	6
Al_2O_3	0.1	4	0.2	4

The thermal Al_2O_3 deposition is performed using TMA and H_2O as precursors, separated by N_2 purge steps. The TMA precursor is maintained at 20°C. The complete ALD cycle for thermal Al_2O_3 deposition is listed in Table 3.2.

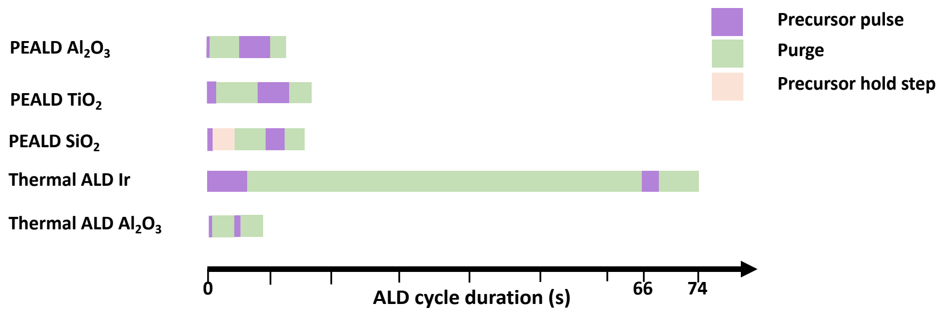

Figure 3.7: Schematic diagram of ALD cycle duration for depositing PEALD Al_2O_3, TiO_2, SiO_2, and thermal ALD Ir and Al_2O_3 thin films.

In Figure 3.7, an overall summary is provided on the duration of thermal and PEALD processes used in this dissertation. It depicts an outline of step sequences of the materials grown for single layer films and corresponding heterostructures.

Chapter 4

Characterization techniques

In this chapter, various thin film characterization techniques will be discussed. A holistic set of spectroscopic and microscopic methods which have been implemented to determine the structural, chemical, and optical properties of the single layer films and heterostructures will be briefly explained.

4.1 Spectroscopic ellipsometry

Spectroscopic ellipsometry is a non-destructive, non-contact, highly sensitive optical measurement technique, which enables the determination of thickness and optical constants of thin films [126, 127]. The working principle is based on the change in polarization of the incident beam after being reflected from the sample surface (as demonstrated in Figure 4.1). Linear polarized light is incident on the sample surface, and then the polarization state is changed to elliptical polarization due to the interaction of light with the specimen. The polarization of the reflected beam is then analyzed using an analyzer. The change in polarization states is characterized by ellipsometric parameters, amplitude ratio ψ, and phase difference Δ between the parallel (p) and perpendicular (s) polarized components. They are related to each other by Eq. 4.1, where the product of $\tan\psi$ and $e^{(i\Delta)}$ is equal to the ratio of Fresnel coeficients. The values of r_p and r_s are Fresnel coeficients for reflectance at p- and s-polarizations, respectively, as mentioned in

Chapter 2.4.

$$\tan\psi e^{(i\Delta)} = \frac{r_p}{r_s} \tag{4.1}$$

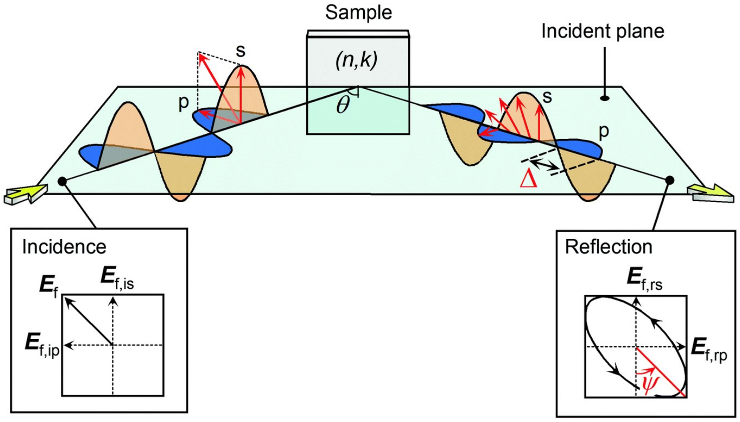

Figure 4.1: Schematic representation of the basic working principle of spectroscopic ellipsometry technique [128]. It indicates the change in polarization of incident electromagnetic wave after reflection from the sample surface, i.e., from linear polarization to elliptical polarization.

For a fixed angle of incidence, within a given spectral range, the values of ψ and Δ are determined as a function of wavelength during the measurement. The determination of optical constants (refractive index n, extinction coeficient k) and the film thickness are performed indirectly, from a model-based fitting approach. An optical model for each layer material system is developed based on dispersion models (e.g., the Cauchy model for the transparent wavelength range [129]). The final result is obtained by fitting the experimentally measured data with the ellipsometric data of the dispersion model by varying the model parameters until a possible minimum root mean square error (MSE) is attained. For example, the most general form of the Cauchy equation is

$$n(\lambda) = A + \frac{B}{\lambda^2} + \frac{C}{\lambda^4} + \ldots \tag{4.2}$$

where n is the real part of refractive index, λ is the wavelength, A, B, C,.... are the Cauchy coeficients which can be determined for a material by fitting the equation to the measured ellipsometric parameters at a particular wavelength range. The general form of MSE is as follows,

$$MSE = \sqrt{\frac{1}{N}\sum_{(i=1)}^{N}(f_i - x_i)^2} \tag{4.3}$$

where, N is the number of data points, f_i is the value obtained by the model and x_i is measured value of i_{th} point. This quantifies the quality of the fit to the experimentally measured data.

In order to evaluate the optical constants and thickness of the films, the measurements were performed using a Woollam M-2000^{TM} spectroscopic ellipsometer [130] on one side polished Si (100) wafers as substrates. While developing single layer dielectric and metal films, four small Si wafers were placed at approx. 150 mm diameter across the chamber in order to estimate non-uniformity across the chamber around 6". The angle of incidence of the ellipsometer is fixed at 75°. The spectral range of the measurement is from 246 to 1687 nm.

In this dissertation, all the Al_2O_3/TiO_2 heterostructures were investigated to determine the total stack thickness and optical constants. Cody-Lorentz dispersion model [131] has been implemented to obtain precise information about the optical band-edge of various compositions due to the presence of TiO_2 in the system. Experimental data were analysed using the CompleteEASE^{TM} software program. For the metal-dielectric (Ir/Al_2O_3) heterostructures, the measurements were performed on fused silica samples using an SE850 DUV ellipsometer by Sentech Instruments GmbH [132]. The angle of incidence has been varied from 50° - 70° in steps of 10°. Drude model accompanied by multiple Lorentz oscillators has been found to be the most suitable to describe these systems. The ellipsometric parameters were fitted using the SpectraRay/4 software for assessing the total stack thickness and optical constants of different compositions.

4.2 UV/VIS spectrophotometry

The spectrophotometry technique has been implemented to measure the reflection R and transmission T spectra of the thin film optical coatings. Commercial dual beam ratio recording spectrometers Lambda 950 and Lambda 900 from PerkimElmer^{TM} have been used. These spectrometers mainly consist of the following components: (i) light sources (UV and VIS/NIR), (ii) monochromator (wavelength selector), (iii) mirrors, (iv) sample holder, (v) photodetectors, (vi) signal processor, and (vii) display unit. A schematic illustration is given in Figure 4.2(a). The radiation sources used are tungsten filament and deuterium arc lamp (for the UV region). Monochromator selects a particular wavelength. The measurement accuracy is around ±0.2% in the VIS and ±0.3% in the UV. A home-build VN device [134] enables the measurement of transmittance T and reflectance R for the same position on the sample. An example of the VN-device operating in reflection mode is displayed in Figure 4.2(b). The sample (marked in red in Figure 4.2(b)) is placed between the source and a rotating mirror setup. The mirror setup can be adjusted to measure the T and R respectively without modifying the position of the sample, essentially keeping the incident beam geometry intact. The measurements are performed on coated fused silica substrates at an incident angle of 6°, where polarization effects are negligible, in the spectral range of 200 nm to 2200 nm. The total optical losses OL due to absorption and scattering are determined as OL(%) = 1 − (T + R).

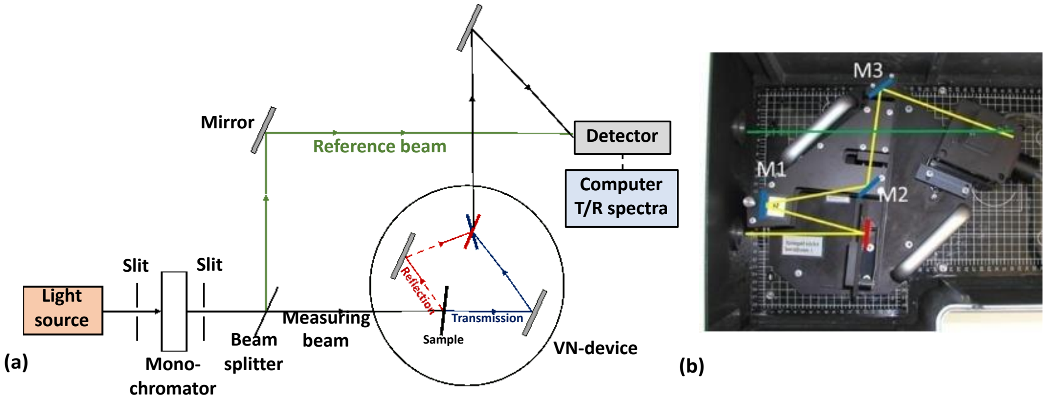

Figure 4.2: (a) Schematic diagram of the UV/VIS spectrophotometry measurement setup. (b) Optical beam path through the in-house-built VN device while measuring in the reflection mode [133].

The T, R spectra of the single layer films, and corresponding heterostructures are thoroughly measured by employing UV/VIS spectrophotometry. Additionally, for the AR coatings, the T, R spectra are also measured at 45° for evaluating the wide angular response of those coatings. At a higher angle of incidence, the T, and R measurements were performed at s and p polarization separately, and further, the average is calculated.

4.3 Various methods

X-ray reflectometry (XRR)

X-ray reflectometry (XRR) has been applied to determine the layer thickness, layer density, and interface roughness of the coatings. For these measurements, the X-ray diffractometer D8 Discover (Bruker AXS, Karlsruhe, Germany) with Cu K_α radiation ($\lambda = 0.154$ nm) in Bragg-Brentano geometry in a 2θ angle range from 10° to 70° was used. Acceleration voltage and cathode current were set to 40 kV and 40 mA, respectively. The XRR data were further analysed using the Bruker Leptos 7 software package. When X-ray radiation (where the refractive index n of material is slightly less than 1) is incident on the sample surface at a grazing angle θ around the critical angle θ_c, the light is reflected off the surface and detected by the detector according to the geometry shown in Figure 4.3. The reflected intensity decays rapidly with increasing θ above θ_c, proportional to θ^4. The reflected intensity contains information on the thickness, density, and roughness of the layer system. The critical angle θ_c corresponds to the film density, the

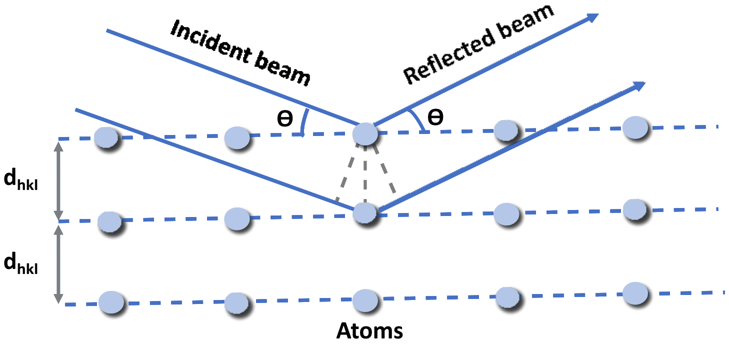

Figure 4.3: Schematic illustration of X-ray diffraction (XRD) and reflectometry (XRR) techniques. The incident beam is reflected from the thin film surface.

period of oscillation is related to the layer thickness, and the attenuation in intensity and oscillations at higher angles imply the interface and surface roughnesses. The structure of a heterostructure with film thicknesses of a few Å is approaching the X-ray incident beam wavelength. Having a wavelength range comparable to the lattice constants of materials, the X-ray diffraction (XRD) technique is performed to probe the crystallinity of a material. When X-ray radiation penetrates the sample surface, it undergoes diffraction and multiple reflections at each lattice plane. This phenomenon can lead to constructive interference when the Bragg condition is satisfied:

$$m\lambda = 2d_{hkl}\sin\theta \tag{4.4}$$

where m is the diffraction order, λ is the wavelength of incident X-ray, d_{hkl} is the lattice plane spacing, and θ is the angle between the incident X-ray beam and the lattice planes. The crystalline phases of the material can be determined from the diffraction peaks. For amorphous materials, a flat spectrum profile is observed due to diffused scattering instead of distinct diffraction peaks.

The individual layer thicknesses, density, and interface roughness of the ALD-grown heterostructures have been investigated by the XRR technique. The amorphous nature of metal-dielectric heterostructures was verified by the XRD measurements.

X-ray photoelectron spectroscopy

X-ray photoelectron spectroscopy (XPS) is a quantitive elemental analysis method at the surface of the sample by the spectroscopy of emitted photoelectrons. The peak positions, peak shifts, or changes in peak shape in the binding energy spectra demonstrate the chemical states in the material. X-ray photons are incident on the sample, which cause the removal of bound electrons (i.e., photoelectrons) if the photon energy is higher than the work function of the material. The excess energy will be attributed to the kinetic energy of the emitted photoelectrons. This method is capable of providing a depth resolution of 2-10 nm depending on the energy of incident electrons.

The chemical composition of the grown heterostructures has been analyzed by the XPS method using an XR 50 M X-ray source with a FOCUS 500 monochromator (SPECS Surface Nano Analysis GmbH, Berlin, Germany) employing an Al K_α radiation (1486.7 eV) in normal emission. The photoelectrons were detected with a PHOIBOS 150 hemispherical electron analyzer with a three-dimensional DLD4040-150 delay-line detector.

Scanning tunneling microscopy

The scanning tunneling microscopy (STM) technique enables visualization of the topography of the sample surface to an atomic resolution. The method relies on the change in tunneling current based on the separation between the probe tip and the sample surface. The STM measurement was executed at room temperature using an Easyscan 2 STM from Nanosurf operated with a Pt/Ir tip. In this dissertation, STM measurements were performed on a few ALD cycles of Ir coating for understanding the nucleation behaviour of Ir at an atomistic level. Measurements were done at a voltage of 2.5 V with 1.0 nA current in constant current mode. STM is typically performed on conductive surfaces. The measurement method being extremely surface sensitive limits the depth resolution up to a few monolayers ($\approx$ a few Angstroms).

Electron microscopy methods

Various electron microscopy techniques, e.g., scanning electron microscopy (SEM), scanning transmission electron microscopy (STEM), transmission electron microscopy (TEM), high resolution TEM (HRTEM) have been implemented to visualize the topography, morphology, and cross-sectional view of the heterostructures depending on the required resolution. Electron microscopes are employed to obtain images with very high resolving power (down to atomic limit), which optical microscopes are limited to provide. A highly focused beam of electrons impinges on the sample to scan across the surface. In general, the working principle of an electron microscope involves focusing of an electron beam on the sample surface, the interaction of the electrons with atoms on the surface, and the detection of electrons or X-ray radiation. The electrons can be generated out of various types of interactions, such as secondary electrons - produced by the excited atoms on the sample surface, back-scattered electrons, transmitted electrons, and characteristic X-rays. This contains information about the morphology and cross-sectional view of the film system.

The basic scanning electron microscopy (SEM) consists of an incident electron beam system, scanning of the sample surface, and eventually detection of secondary and back-scattered electrons. The achieved resolution is in general around 1-10 nm. The number of generated secondary electrons depends on the incident energy. In order to gain a better insight into the microstructures ($\approx$ a few nm) of the atomic scale heterostructures presented in this dissertation, selected samples were examined using a scanning transmission electron microscope (STEM). Here, the electron beam passes through a very thin lamella of the layer system, which is previously cut and thinned out of the sample by means of a focused ion beam (FIB). STEM is able to produce an even higher resolution images below a nanometer. Selected Al_2O_3/TiO_2 heterostructures have been investigated under the cross-sectional STEM using a Thermo Fisher FEI Titan3 80–300 transmission electron microscope, equipped with a high-angle annular dark field (HAADF) STEM detector (Fischione model 3000), at 300 kV acceleration voltage. TEM sample preparation was done with a wedge polishing approach, i.e., by a purely mechanical thinning of a sample piece under a defined, low angle with an Allied MultiPrep sample polishing tool. The wedge-polishing was done until the sample surface with the PEALD layer on top gained a residual thickness of a few tens of nm. Final thinning to electron transparency and sample cleaning was done with a low-angle, low-energy (2.5 keV) broad Ar^+ ion beam polishing device (Gatan precision ion polishing system PIPS II).

The Ir/Al_2O_3 heterostructures possessing even thinner individual thicknesses demanded for further higher resolution. Transmission electron microscopy (TEM) relies on the detection of transmitted electrons through a suitably prepared thin lamella of the sample, enabling resolution as close as a nanometer. Here, TEM, including high-resolution (HRTEM) studies were performed on selected compositions using an image aberration-corrected Titan 80-300 environmental TEM operated at 300 kV, and equipped with a Gatan Quantum 965ER GIF. For the TEM studies, the samples were prepared by mechanical polishing followed by ion milling using a Gatan PIPS 695 setup.

White light interferometry

White light interferometry (WLI) is used to evaluate the surface roughness of thin films based on the optical interference effect. The interference pattern (i.e., optical beam path) changes depending on the distance between different points of the scanning area on the sample surface and the detection objective lens. A NewView 7300 system (Zygo, Middlefield, CT, USA) with 50x magnification was used for WLI measurements to evaluate the long-range surface roughness of the Ir/Al_2O_3 heterostructures. Sample areas of 500 x 500 μm^2 were scanned. For each WLI measurement area, the power spectral density (PSD) function was calculated, characterizing the relative strength of each roughness component in terms of spatial frequencies. These single PSD functions were combined by geometrically averaging to the so-called Master-PSD function.

Thin film stress measurement

Mechanical stress of the layered stacks has been measured using the wafer curvature method with an FLX 2320 equipment (KLA-Tencor GmbH, San Jose, USA). The change in radius of curvature of the Si wafer before and after the deposition of thin films allows for determining the mechanical stress. The stress value for the coating is calculated using Stoney's equation [135],

$$\sigma = \frac{1}{6}\frac{E_s}{(1-\nu_s)}\left(\frac{1}{R_f}-\frac{1}{R_s}\right)\frac{t_s^2}{t_f} \tag{4.5}$$

where E_s is the Young's modulus, ν_s is Poisson's ratio of the substrate, R_s and R_f are the radii of curvature of the substrate before and after deposition, and t_s and t_f are the thicknesses of the substrate and the film, respectively. Posi-tive and negative mechanical stress values correspond to tensile and compressive stresses, respectively. The mechanical stress of Al_2O_3/TiO_2 heterostructures has been determined on 3" double-side polished Si (100) wafers applying this method.

Chapter 5

Dielectric heterostructures

This chapter thoroughly discusses the development and properties of atomic scale quantum-well heterostructures composed of Al_2O_3/TiO_2. It starts with a detailed analysis of the growth of single layer Al_2O_3 and TiO_2 films followed by the creation of their hetero-interfaces by precise tuning of compositions enabled by the ALD technology. Various spectroscopic and microscopic characterization methods have been carried out to understand the structure-property relationship of these heterostructures. Following this, the evolution of optical bandgap has been studied in the light of quantizing heterostructures. Finally, an application of selected heterostructures in antireflection coating for the UV spectral range has been demonstrated.

Semiconductor quantum well structures and their device applications have been a broad field of research over the past decades. It started with the experimental realization of widely applied GaAs/AlGaAs [9, 10], GaN/AlN [5] heterostructures in the early 1980s and eventually leading towards a plethora of III-V and II-VI based materials using epitaxial growth techniques [136–138]. These structures have revolutionized the field of optoelectronics [139, 140], laser diodes [141, 142], LEDs [143, 144], and quantum well lasers [145], to list a few. Gradually, attention has been devoted towards developing dielectric-based quantum well structures due to their suitability in optical and photonic applications [53, 54, 146]. In this disser-tation, an experimental route to access the technologically challenging thickness requirements of dielectric quantum well structures via PEALD processes has been demonstrated along with their potential utilization in multilayer optical coatings.

5.1 Growth of single layer films

The PEALD equipment, precursors and process parameters for growing single layer Al_2O_3 and TiO_2 films have been discussed in detail in Chapter 3.2. The PEALD processes of the single layer oxides were developed to ensure a reproducible growth rate and necessary optical properties along with a reasonably low non-uniformity, which is <3% on 200 mm area. The PEALD method enables to grow high quality films while maintaining the substrate temperature at 100°C for all depositions.

- Single layer TiO_2 films

Upon growing the single layer PEALD TiO_2 films, these were thoroughly characterized to assess their properties with decreasing film thickness. The level of dificulty to determine the properties of ultrathin layers increases as the film thickness decreases to nanometer or sub-nanometer scales. The implemented characterization methods are thoroughly described in Chapter 4. The film thickness d has been determined and compared by using XRR and SE methods. Figure 5.1(a) shows d of single layer TiO_2 films as a function of ALD cycles obtained by XRR and SE (using both Cauchy and Cody-Lorentz models, as discussed in Chapter 2.3) indicating a promising agreement between these two techniques. A linear increase in film thickness with an increasing number of ALD cycles ensures the self-limiting growth behaviour, i.e., the so-called stable ALD operation regime (as discussed in Chapter 3.1). From the linear fit of the data, the slope and the x-intercept provide the growth per cycle (GPC) and the nucleation delay, respectively. Consistent GPC values are obtained by both SE and XRR methods ranging from 0.33 to 0.35 Å/cycle. These investigations ensure precise control and reproducibility over the PEALD processes.

Thermal and PEALD TiO_2 films were studied previously by various research groups [52,147–151]. The developed PEALD layers at 100°C demonstrated in this

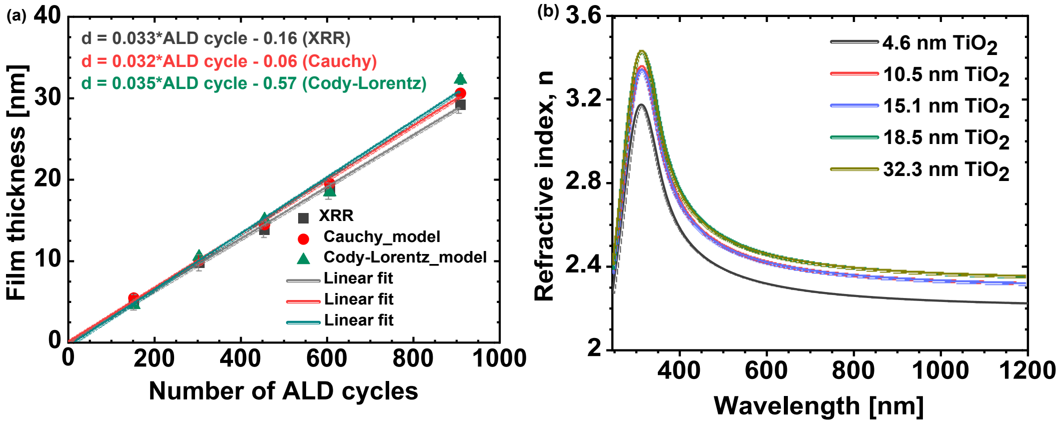

Figure 5.1: (a) Film thickness of single layer PEALD TiO_2 films deposited at 100°C determined by spectroscopic ellipsometry (SE) and X-ray reflectometry (XRR) measurements, (b) dispersion behaviour of single layer TiO_2 films determined by the Cody-Lorentz SE model.

dissertation manifest similar properties to the previously reported investigations. Table 5.1 summarizes the film thicknesses and the root mean square (r.m.s.) surface roughness values of single layer PEALD TiO_2 films estimated by SE and XRR measurements, respectively. The thickness values obtained by SE, are in excellent agreement with the XRR results even for the ultrathin layers. Simultaneous determination of the optical constants and the film thickness of ultrathin films by SE is challenging. However, the agreement with the XRR measurements indicates the reliability of the SE technique even for thin films with less than 20 nm thickness. The TiO_2 films are smooth having r.m.s. surface roughness values varying from 0.3 to 0.4 nm, whereas the uncoated Si wafer substrate has a r.m.s. roughness of about 0.15 nm. The XRR and SE measurements also confirm a negligible nucleation delay during the growth of PEALD TiO_2 layers, as indicated by the intercept of the curves in Figure 5.1(a).

Figure 5.1(b) illustrates the dispersion spectra of single layer PEALD TiO_2 films of different thicknesses obtained by the Cody-Lorentz SE model. The refractive index n values range from 2.3 to 2.6 in VIS, which corresponds very well with the TiO_2 thin films grown by other deposition techniques, such as e-beam evaporation [152], RF-sputtering [153] and thermal ALD [154]. As the film thickness increases, a slight increase in n is observed, indicating the growth of denser films.

Table 5.1: Film thickness d and r.m.s. surface roughness, refractive indices n, and indirect optical bandgap E_g of single layer PEALD TiO_2 films deposited at 100°C were characterized by XRR and SE on Si substrates.

Number of TiO_2 PEALD cycles	Target thickness (nm)	Experimental thickness d (nm)			Roughness r.m.s. (nm)	n at 1030 nm	E_g (eV)
		Cody-Lorentz	Cauchy	XRR			
152	5	4.6	5.5	4.9	0.32	2.23	3.36
303	10	10.5	10.1	9.8	0.32	2.32	3.33
455	15	15.1	14.5	13.9	0.33	2.32	3.32
606	20	18.5	19.5	18.6	0.36	2.35	3.31
909	30	32.3	30.6	29.2	0.40	2.35	3.30

Indirect optical bandgap E_g of amorphous thin PEALD TiO_2 layers was evaluated by implementing Tauc-plot calculations, as reported by Jan Tauc et al. in 1966 [155]. The Tauc plot method is a well-established technique for determining optical bandgap values for a wide range of amorphous and crystalline thin film materials [156,157]. Since the density of states are considered as a parabolic function, we linearize it. This technique uses the relationship between energy E and the absorption coeficient α to estimate the optical bandgap. The equation below describes the relationship between α and E according to the Tauc plot method:

$$\alpha h\nu = A(h\nu - E_g)^b \tag{5.1}$$

$$A = \frac{e^2}{bch^2 m_e^*}(2m_r)^{\frac{3}{2}} \tag{5.2}$$

where A is a proportionality constant, hν is the photon energy in eV, E_g is the optical bandgap in eV, and b is the electronic transition coeficient. The value of b depends on the case of direct or indirect transitions. Such as, $b = 2$ and $b = \frac{1}{2}$ imply the indirect allowed and direct allowed transitions, respectively. Similarly, the values of $b = 3$ and $b = \frac{3}{2}$ demonstrate the indirect forbidden and direct forbidden transitions consecutively. The m_e^* and m_r are the effective mass and reduced mass of the electron or charge carrier, respectively.

Amorphous TiO_2 thin films possess indirect optical bandgap. Therefore, a

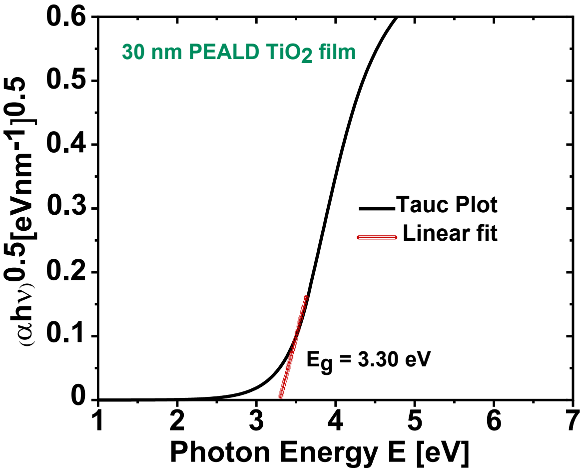

Figure 5.2: Estimation of the indirect optical bandgap of 30 nm PEALD TiO_2 film using Tauc plot calculations.

plot of $(\alpha h\nu)^{1/2}$ vs. E (where, E = hν, in eV) has been depicted. Initially, the absorption contribution is zero at energies below the optical bandgap, followed by a slow gradual increase (the so-called Urbach tail, due to intraband or defect state transitions very close to the bandgap; discussed in Chapter 2.2), and finally leading to sharply rising linear regime as depicted in Figure 5.2, a typical Tauc plot of an indirect bandgap material. The intercept of the linear fit along this linear regime at the E axis estimates the value of the optical bandgap. The indirect optical bandgap of thin PEALD TiO_2 layers is about 3.3 eV, with a ±0.02 eV determination uncertainty, which is in very good agreement as reported in several literatures [152, 154]. The bandgap of the single layer TiO_2 films increases with decreasing film thickness (Table 5.1) indicating towards quantization effects. This relatively low bandgap material TiO_2 has been employed as the quantum well material in the heterostructures.

- Single layer Al_2O_3 films

Alumina (Al_2O_3), the classical ALD material has been extensively studied since the beginning of ALD technology. Single layer PEALD Al_2O_3 thin films have a GPC of ≈ 1.23 Å/cycle and n ≈ 1.6, which is consistent with previously reported data [158]. The optical bandgap of Al_2O_3 is typically around 7 eV [159]; however, it could not be determined in this work for the PEALD films because of the limited available spectral range of the ellipsometer. The high bandgap material Al_2O_3 is therefore a suitable choice as the barrier layer in the heterostructures.

5.2 Growth and properties of Al_2O_3/TiO_2 heterostructures

Upon developing uniform, dense, optically homogeneous, and smooth single layer films, various sets of Al_2O_3/TiO_2 heterostructures were prepared by tailoring their compositions. The sequential deposition of Al_2O_3 and TiO_2 layers are performed keeping the total stack thickness above 50 nm to facilitate reliable optical characterizations. The convention of naming the dielectric heterostructures is as follows: for instance, composition '[16:64]*50' stands for 16 cycles of Al_2O_3 followed by 64 cycles of TiO_2 and this sequence has been repeated for 50 times (i.e., the number of supercycles). This framework has been followed throughout the description.

5.2.1 Structural properties

To elucidate the structural evolution of these heterostructures, several microscopic and spectroscopic analyses have been carried out. Table 5.2 summarizes the composition parameters including individual numbers of Al_2O_3 and TiO_2 cycles and numbers of supercycles. It also provides a thorough evaluation of film thickness d determined by Cauchy and Cody-Lorentz SE models, respectively, n at 1030 nm for each composition and E_g of the Al_2O_3/TiO_2 nanostructures. Film thickness d (see Table 5.2) evaluated by both dispersion models exhibit excellent agreement with a minimal discrepancy. The optically determined thickness values of the samples which have additionally been investigated by XRR and STEM are presented in bold. These values indicate very good agreement with the XRR data (see Table 5.3). Some bilayer structure has been further investigated by STEM cross-sectional analysis. The STEM image of a '[16:8]*10' composition is presented in Figure 5.3 to obtain a visual perspective of PEALD-grown atomic scale heterostructures. From left (in Figure 5.3(a)), the crystalline Si substrate, fol-

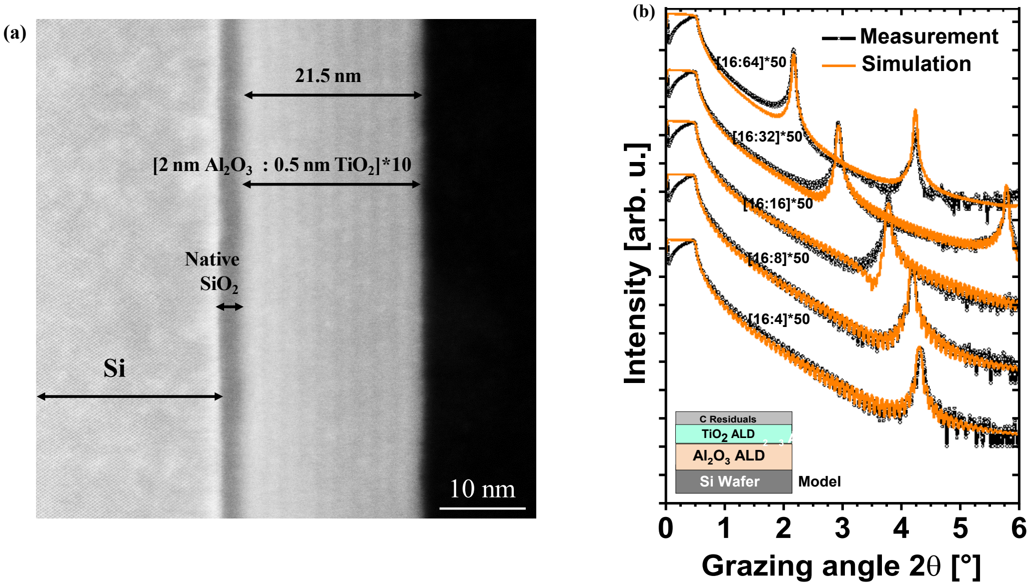

Figure 5.3: (a) Cross-sectional scanning transmission electron micrograph (STEM) of the [16:8]*10 sample and (b) X-ray reflectometry (XRR) measurements in grazing angle of incidence up to 3°and simulation curves of selected Al_2O_3/TiO_2 heterostructures.

lowed by the native SiO_2 (≈ 1.5 nm) and finally the periodic bilayer structure of Al_2O_3/TiO_2 are visible. The contrast is quite constrained due to the instrument limitation at this length scale. However, the superlattice structure of the sample is clearly visible, ensuring distinct interfaces at sub-nanometer scale along with an indication of 10 supercycles, as expected from the deposited repetitions. The total thickness of the '[16:8]*10' bilayer is 21.5 nm, as obtained by STEM measurement, and corresponds well with the thickness value of the same composition ratio evaluated by SE, as given in Table 5.2.

The results of XRR measurements on a selected set of compositions are illustrated in Figure 5.3(b). The fit of the experimental data has been performed using the density of the single layer thin films, in order to reduce the number of fit parameters. The density parameters were 3.90 gm/cm^3 and 2.95 gm/cm^3 for Al_2O_3 and TiO_2, respectively [52]. Distinct Bragg peaks are observed for these compositions already below $2\theta = 6°$ angle indicating layered heterostructures with very high quality. A distinct reflection peak is observed even for the [16:4]*50 sample having ≈ 0.13 nm of individual TiO_2 layer thickness, thus roughly corresponding

Table 5.2: Composition ratio, total stack thickness d, mechanical stress σ, refractive indices n and indirect optical bandgap E_g of various Al_2O_3/TiO_2 heterostructures.

Composition $[Al_2O_3:TiO_2]*N$	Ratio of $Al_2O_3:TiO_2$	Expected percentage of TiO_2 (%)	d (nm)		σ (MPa)	n at 1030 nm Cody-Lorentz	E_g (eV)	
			Cauchy	Cody-Lorentz			Cody-Lorentz	Optical Losses
[16:64]*50	1:4	52	204.7	204.6	162	2.08	3.45	3.33
[8:64]*50	1:8	68	156.4	156.3	210	2.17	3.43	3.32
[4:64]*50	1:16	81	133.3	132.6	256	2.24	3.40	3.18
[16:32]*50	1:2	35	150.3	149.9	216	1.96	3.46	3.34
[8:32]*50	1:4	52	100.2	100.7	270	2.04	3.50	3.33
[4:32]*50	1:8	68	72.7	72.8	276	2.14	3.35	3.33
[16:16]*50	1:1	21	117.6	117.5	255	1.81	3.70	3.53
[8:16]*50	1:2	35	70.4	70.4	297	1.92	3.57	3.50
[4:16]*50	1:4	52	47.6	47.6	294	2.04	3.56	3.49
[2:16]*75	1:8	68	54.8	54.9	319	2.16	3.50	3.63
[16:8]*50	2:1	12	106.1	106.2	257	1.72	4.04	3.72
[16:8]*10	2:1	12	21.0	21.4	-	1.70	-	-
[8:8]*50	1:1	21	61.0	61.1	336	1.79	3.78	3.69
[4:8]*100	1:2	35	73.7	73.8	294	1.91	3.74	3.51
[2:8]*100	1:4	52	50.2	50.3	294	2.01	3.58	3.48
[16:4]*50	4:1	6	104.2	104.2	280	1.66	3.67	3.78
[8:4]*100	2:1	12	108.6	108.7	266	1.72	4.03	3.76
[4:4]*100	1:1	21	62.8	62.9	312	1.78	3.88	3.73
[2:4]*150	1:2	35	54.9	55.0	274	1.92	3.65	3.64
[8:2]*100	4:1	6	103.4	103.5	105	1.66	4.00	3.85
[4:2]*200	2:1	12	108.9	109.1	267	1.72	3.98	3.79
[2:2]*200	1:1	21	62.1	62.2	301	1.80	3.86	3.72
[1:2]*400	1:2	35	75.4	75.5	363	1.90	3.77	3.56
[1:1]*400	1:1	21	62.1	62.1	351	1.81	3.84	3.74

Table 5.3: Individual layer thicknesses and interface roughness σ_{XRR} of ultrathin Al_2O_3/TiO_2 heterostructures estimated by XRR measurements.

Compositions	[16:64]*50	[16:32]*50	[16:16]*50	[16:8]*50	[16:4]*50
Al_2O_3 thickness (nm)	1.93	1.93	1.93	1.93	1.93
σ_{XRR} Al_2O_3/TiO_2 (nm)	0.37	0.34	0.33	0.22	0.41
TiO_2 thickness (nm)	2.25	1.12	0.42	0.19	0.13
σ_{XRR} TiO_2/Al_2O_3 (nm)	0.83	0.59	0.44	0.62	0.68
Period (nm)	4.18	3.05	2.35	2.12	2.06
Total thickness (nm)	209	152.5	117.5	106	103

to a single monolayer. This leads to the conclusion of achieving controlled growth of heterostructures by ALD. Table 5.3 summarizes individual layer thicknesses determined by fitting the XRR measurements and the resulting total thicknesses, which are also in accordance with SE evaluations, as listed in Table 5.2. The determination and interpretation of interface roughness for such atomically thin heterostructures are complex. It emphasizes that the interface roughness estimated on ultrathin heterostructures are of the same order or even more than the individual TiO_2 layer thickness as film thickness approaches to ≈ 0.5 nm. Al_2O_3/TiO_2 interfaces manifest smaller intermixing than TiO_2/Al_2O_3 interfaces, which can be attributed to the smoothening influence of prior Al_2O_3 layer. Consequently, due to some interface mixing effect, it implies the formation of -O-Al-O-Ti-O- bonds as an intermediate layer at the interface, the apparent quantum well structures gradually become similar for even thinner cases. However, no evolution in roughness has been observed while growing thicker single layer TiO_2 films, as mentioned in Table 5.1. This strongly emphasizes the growth of high quality films via PEALD.

Altogether, the STEM and XRR analyses clearly demonstrate the superlattice nature of these ALD heterostructures. The single layers are very smooth, and despite some intermixing of the oxides at the interfaces, the periodicity of the heterostructure is not altered by increasing the number of bilayers. The presence of the first Bragg peaks even at more than the 4° grazing angle indicates a very precise repetition of the ultrathin layers, which goes down to the atomic scale.

5.2.2 Chemical and me$_c$hanical properties

- Chemical composition

It is important to address the elemental analysis of such atomic scale heterostructures as compared to their thicker counterparts. The chemical composition and structural integrity of selected ultrathin hetero-interfaces in comparison with the single layer films have been investigated by the X-ray photoelectron spectroscopy (XPS) method, discussed in Chapter 4.3. Binding energy analysis has been performed on a selected set of samples. Due to the charge accumulation effect, the binding energies of the C 1s levels vary more than 1 eV. Hence, a correction of the binding energy to 284.5 eV was applied [160]. In Figure 5.4, the comparison of Al 2p, Ti $2p_{1/2}$ and $2p_{3/2}$ peaks have been plotted for a selected set of compositions, such as [2:2]*80, [4:4]*40, [16:8]*10 along with single layer films of Al_2O_3 and TiO_2 as references.

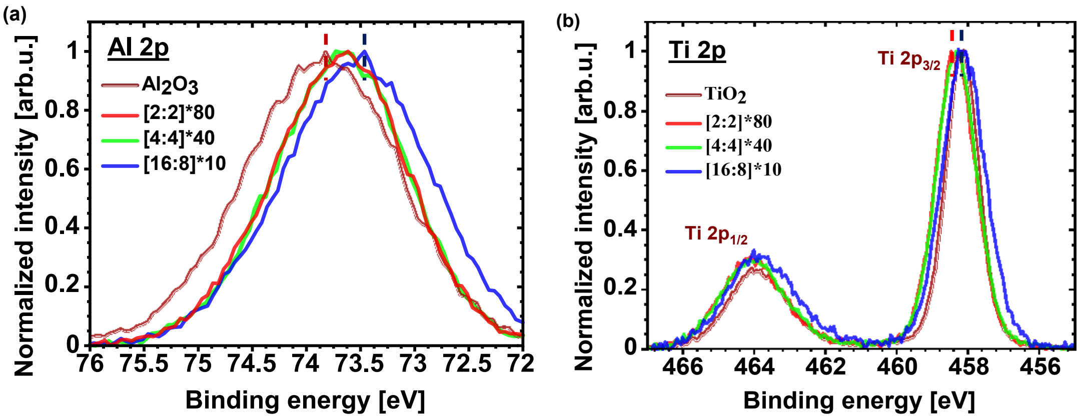

Figure 5.4: X-ray photoelectron spectra (XPS) of (a) Al 2p states and (b) Ti $2p_{1/2}$ and $2p_{3/2}$ states in single layer Al_2O_3, TiO_2 films and three selected heterostructures.

As illustrated in Figure 5.4(a), for the heterostructures, Al 2p peaks are shifted by approximately 0.4 eV. The environment around the Al_2O_3 in the heterostructures is altering the chemical bonding when the layer thickness is approximately 2 nm or below. Previous XRR estimations show that 16 cycles of Al_2O_3 corresponds to ≈ 2 nm and the XPS study indicates the influence of the TiO_2 environment on this bonding. The Ti $2p_{1/2}$ and $2p_{3/2}$ XPS peaks of the above mentioned heterostructures and single layer film are depicted in Figure 5.4(b). The shape of the peaks and their energetic positions are in agreement with single layer TiO_2 peaks as reported in previous studies [161–163]. The Ti peaks for [16:8]*10 heterostructure (blue curve) resemble that of pristine TiO_2 film (brown curve), emphasizing that the chemical character is still preserved even at ≈ 0.2 nm (i.e., 8 ALD cycles) of individual TiO_2 layer thickness. A shift (≈ 0.3 eV) of Ti $2p_{3/2}$ peaks has been observed for the thinner compositions, however, Ti $2p_{1/2}$ peaks remain consistent. Consequently, this highlights the precise composition control achieved by the PEALD technique. The O 1s levels of single layer Al_2O_3 and TiO_2 films are found to be at ≈ 531 eV and ≈ 529 eV, respectively, whereas the O 1s levels of the heterostructures remain in between as a superposition of both oxides. With decreasing thickness of the quantum well and barrier layers, there is a transition to the formation of ternary oxides, where –O–Al–O–Ti–O– bonding is assumed to be prevalent, as the individual thickness approaches below the bond length of the corresponding material. This transition is also reflected in the evolution of optical properties from quantizing structures to atomically mixed oxides, as discussed in the subsequent sections.

- Mechanical properties

The mechanical stress of thin film coatings has a huge impact on optical or MEMS applications [52]. Mechanical stress of the heterostructures has been estimated by using wafer curvature measurements on 3” double-side polished Si wafers, as described in Chapter 4.3. The film stress values σ of Al_2O_3/TiO_2 heterostructures are included in Table 5.2. All compositions undergo tensile stress ranging from 105 - 361 MPa, depending significantly on the composition ratio, i.e., the relative content of the individual components. Broadly, the mechanical stress is higher for the compositions having a higher volume fraction of TiO_2, keeping the number of PEALD Al_2O_3 cycles intact. This is consistent with the previous studies showing enhanced mechanical stress upon increasing the TiO_2 content in TiO_2 based nanolaminates [52]. The mechanical stress could be significantly reduced in heterostructures compared to pure TiO_2 or nanolaminates with thicker TiO_2 layers.

5.2.3 Optical properties

In this subsection, the optical properties, e.g., dispersion spectra, and optical bandgaps of all the compositions have been thoroughly studied by means of a versatile set of optical characterization techniques. The dispersion of the previously selected heterostructures is given in Figure 5.5. The refractive indices of heterostructures with a well thickness of about 2 nm (i.e., 64 ALD cycles of TiO_2) with decreasing barrier thickness are shown in Figure 5.5(a), and the heterostructures with the same barrier thickness of 2 nm (16 cycles Al_2O_3) but decreasing well thickness are depicted in Figure 5.5(b). The dispersion curves show promising agreement between the Cauchy and Cody-Lorentz models emphasizing the reliability of the SE method for precise determination of optical constants of these atomic scale heterostructures. Decreasing the Al_2O_3 content results in increasing n, while decreasing the TiO_2 content indicates decreasing n values. Figure 5.5 also carries the evidence that the superlattices with 2 nm TiO_2 are still not in the quantizing regime since the wavelength range of the refractive index peak does not shift for the corresponding compositions. With further decreasing the quantum well thickness, a quantizing regime is reached and a shift of the spectral position of maximum n has been observed.

To observe the impact on optical properties among the heterostructures having the same ratio of constituent materials, a case study is performed on the compositions possessing the same ratio of materials. Figure 5.6 presents the optical constants for heterostructures with the same ratio of Al_2O_3:TiO_2 and a decreasing period of the superlattice. The total number of cycles for each material is kept constant for the [1:1] up to the [8:8] structures. Their total film thicknesses are nearly identical, indicating robust and precisely controlled ALD growth and no significant effect of the nucleation of the oxides on each other. Refractive index maxima and the extinction coeficients have undergone a small shift in wavelength with decreasing bilayer period. The optical bandgap values of these heterostructures are nearly the same. These properties assure a proper understanding and control of the PEALD processes without any in-situ monitoring, further an important pre-requisite while fabricating heterostructures down to an atomic scale.

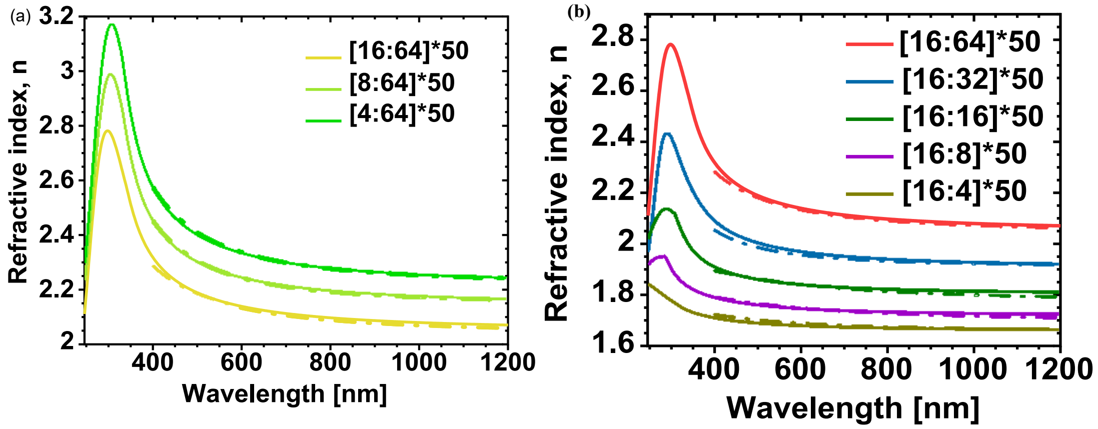

Figure 5.5: Comparison of refractive index n of the heterostructures determined by Cauchy and Cody-Lorentz models (a) with well structures of 64 cycles of TiO_2 where the barrier structure is tuned from 16 to 4 cycles of Al_2O_3 layers and (b) with a barrier structure of 16 cycles with varying well structures from 64 to 4 cycles of TiO_2. Solid and dashed curves represent evaluations by Cody-Lorentz and Cauchy models, respectively.

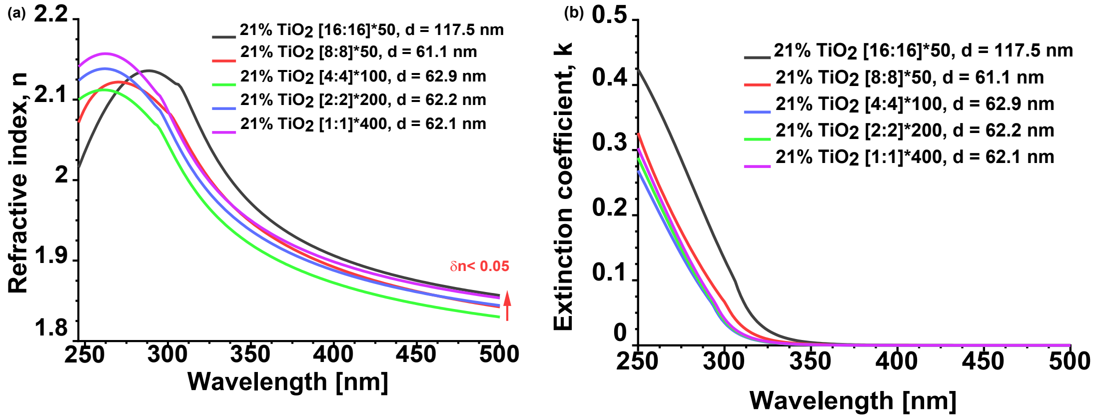

Figure 5.6: (a) Dispersion relation of Al_2O_3/TiO_2 heterostructures having approximately 21% of TiO_2 content, (b) extinction coeficient values denote that the deviation in k is more pronounced near the absorption edge region (i.e., wavelengths lower than 350 nm) for the thickest composition.

- Simulation of optical properties using Bruggeman's approach

In order to obtain consistent theoretical evaluations, the Bruggeman's approach has been implemented in simulating the refractive index spectra of atomic-scale dielectric heterostructures. For simplicity, the electric field vector is assumed to be parallel to the layer interfaces. The anisotropy of the heterostructures is not considered since it is generally very low as compared to the incident wavelength regime [80]. The alternating growth of the two oxides results in the formation of a superlattice with the corresponding energy levels of the constituent conduction and valence bands, as evident from the STEM investigations. In this case, the system behaves like an assembly of dielectrics in parallel alignment [80]. The effective dielectric constant for such an arrangement can be expressed based on Bruggeman's effective medium approximation approach as follows:

$$\epsilon_{1eff} = f_A \epsilon_{1A} + f_T \epsilon_{1T}, \quad \epsilon_{2eff} = f_A \epsilon_{2A} + f_T \epsilon_{2T} \tag{5.3}$$

$$\text{where,} \quad \epsilon = \epsilon_1 + i\epsilon_2 \tag{5.4}$$

and material A signifies Al_2O_3 and material T signifies TiO_2, f_A and f_T are the volume fractions of Al_2O_3 and TiO_2, respectively. Subsequently, the effective refractive index n_{eff} of the composites has been calculated using this approach. The observations from Bruggeman's approximation imply a very good agreement with the experimental values in the transparent spectral range. A reasonable consistency between the simulation and experiment has been observed, as demonstrated in Figure 5.7(a). However, some deviation has been noted for the thicker compositions, as inhomogeneous nanolaminates are assumed to be uniform mix-

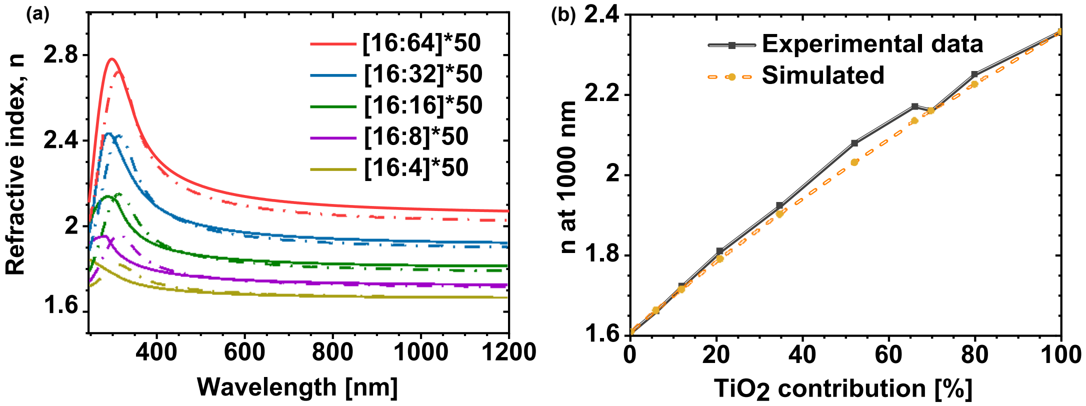

Figure 5.7: (a) Comparison of the dispersion spectra evaluated by SE (solid curves) and the Bruggeman approach (dashed curves) and (b) n at 1000 nm wavelength as a function of the percentage of the TiO_2 content in heterostructures, showing reasonable agreement between simulated and experimental data.

tures in Bruggeman's approximation calculations. From previous investigations, ultrathin layers must be considered in the design of optical interference coatings, since even a 1.5 nm thin Al_2O_3 layer has an influence on the optical performance of antireflection coatings [120]. Simultaneously, this indicates that the 16 cycles Al_2O_3 (≈ 2 nm) lead to a closed layer, as supported by XRR and STEM investigations making the system inappropriate to be modelled by a homogeneous mixture description. The discrepancies can be attributed to such deviations. The agreement between the experiment and the simulated data using the Bruggeman model is more reliable in the spectral range where TiO_2 is transparent. In the UV spectral range, a large discrepancy is observed for the quantizing structures with ultrathin bilayers. Significantly higher extinction properties are predicted as the model does not consider the quantizing phenomenon or the formation of ternary compounds. The EMA approach based on Bruggeman's approximation supports in providing a reasonable estimation of the optical dispersion spectra of these all-dielectric heterostructures, especially in the transparent spectral range.

- Optical bandgap and quantizing structures

Upon evaluating the structural properties, and optical constants, the evolution of the optical bandgap has been systematically analyzed in the context of creating quantizing heterostructures. Here, the well structure (TiO_2 cycles) is varied, while keeping a fixed barrier thickness (Al_2O_3 cycles). A case study is included using 16 cycles of Al_2O_3 layers, corresponding to a barrier thickness of 2 nm, with varied TiO_2 thicknesses between 2 and ≈ 0.1 nm (basically, 64 to 4 PEALD cycles).

Coming to the extinction coeficient spectra, Figure 5.8 depicts (a) the extinction coeficients k and (b) the optical losses OL for films with the Al_2O_3 barrier structure of 16 cycles (2 nm) with varying well structures of TiO_2 cycles from 64 (≈ 2 nm) to 4 (≈ 0.1 nm). As demonstrated in Figure 5.8, the k and OL val-ues undergo a blue shift as the amount of TiO_2 is decreasing in the composition implying a promising indication towards obtaining optical quantizing structures in Al_2O_3/TiO_2 based hetero-interfaces. These results demonstrate an eficient route via PEALD to precisely control the compositions and optical properties of

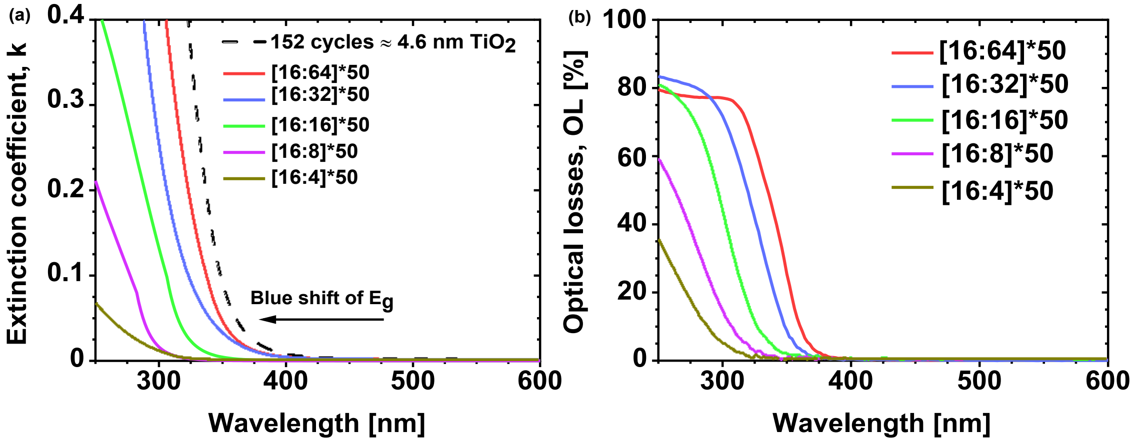

Figure 5.8: Comparison of (a) extinction coeficients k and (b) optical losses OL for a barrier thickness of 16 cycles of Al_2O_3 with a varying number of TiO_2 cycles.

heterostructures. Novel Al_2O_3/TiO_2 quantum well structures are fabricated to tailor both n and k of the heterostructure stacks. As observed in the extinction coeficient curves, initially when the quantum well thickness is ≈ 1 nm or above (corresponding to red and blue curves) there is a slight decrease in the absorption edge. Further, as the quantum well thickness becomes comparable to or less than 0.5 nm (i.e., close to 16 PEALD cycles, denoted by the green curve), the strong blue shift in the absorption edge and consequently in the optical bandgap denotes the presence of the quantum confinement phenomenon. As the quantum well thickness approaches the Bohr radius, it supports the trapping of electron mobility within the well structure such that there is a negligible probability of obtaining the electron wave function outside the quantum well region.

The indirect optical bandgap E_g of the dielectric heterostructures has explicitly been explored using Tauc plot calculations. Table 5.2 enlists the estimated E_g values of Al_2O_3/TiO_2 composite films, indicating a significant dependence on the thickness as well as more importantly on the composition ratio. As an example, Figure 5.9 exhibits the determination of E_g using the [16:8]*50 structure from (a) SE and (b) OL data, respectively. As implied from the Tauc plots, the electronic transitions are changing with the compositions, which demonstrates that both the electron and hole configurations can be manipulated within the well structure. For example, for the structure [16:64]*50, i.e., ≈ 2 nm well thickness, the

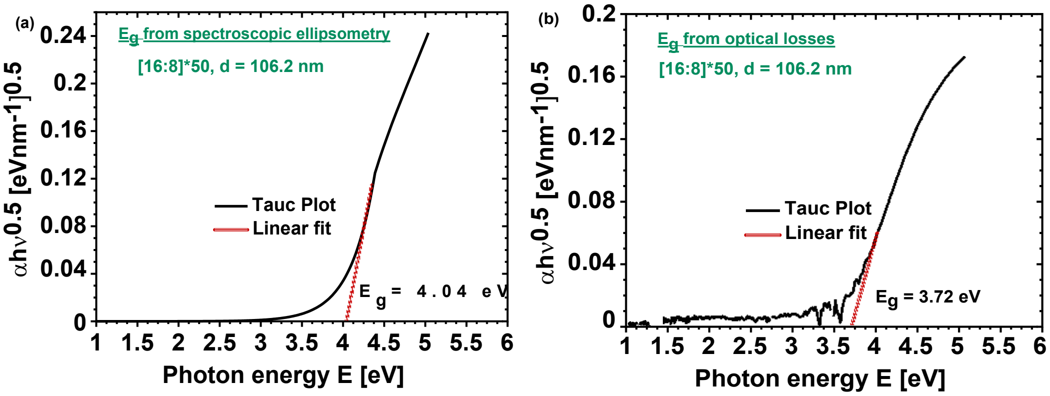

Figure 5.9: Indirect optical bandgap E_g of the [16:8]*50 heterostructure sample estimated from the (a) SE (Cody-Lorentz model) measurements and (b) OL data by UV/VIS spectrophotometry.

shape of the Tauc plot is very similar to that of single layer TiO_2 films, indicating 2 nm is too thick to obtain quantizing effects. Whereas, in the case of the [16:8]*50 composition having ≈ 0.5 nm TiO_2 thickness gives rise to a significant increase in optical bandgap (see Figure 5.9 (a)), which can be attributed to the quantum confinement effect when the well thickness emerges to values comparable to the Bohr radius. However, the Tauc plot obtained from OL values in Figure 5.9 (b) incorporates noise from the T/R measurements. Furthermore, while fitting the Tauc plot obtained from OL data, it can be challenging to differentiate the influence of the Urbach tail region, making it critical to precisely estimate the optical bandgap. In contrast, the ellipsometry technique facilitates a direct determination of extinction coeficient k values. OL contains the information on the overall optical losses (i.e., absorption and scattering losses), implying SE measurements to be more reliable for precise estimation of E_g values. The determination of E_g relies on the accuracy of finding the linear region in the Tauc plot to obtain the best fit, which contains an estimation uncertainty of ±0.2 eV. Both techniques exhibit a clear increase in bandgap values in the heterostructures as compared to single layer TiO_2 films due to the presence of Al_2O_3 layers, validating a consistent trend between the two evaluation methods. Values of E_g vary from 3.38 to 4.04 eV as estimated from SE measurements (see Table 5.2), whereas E_g values range from 3.18 to 3.85 eV using UV/VIS spectrophotometry measurements. Overall, the estimation of E_g from the SE method turns out to be more reliable, as it contains a significantly lower signal-to-noise ratio near the Urbach tail region along with providing a direct estimation of k values as a function of λ based on fitting with the dispersion model approach.

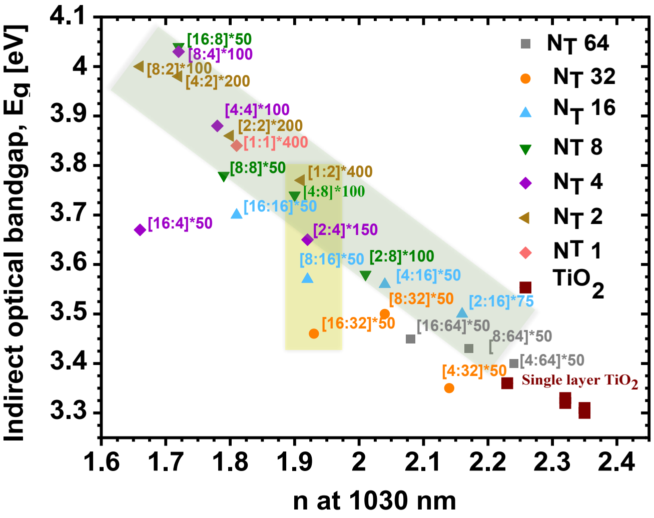

Figure 5.10: Indirect optical bandgap E_g of Al_2O_3/TiO_2 heterostructures in comparison with single layer TiO_2 films as a function of refractive index n at 1030 nm wavelength. The green shaded region is provided for a guide to the eye indicating an inverse relationship between E_g and n. The yellow shaded region demonstrates a set of heterostructures of the same ratio (1:2) of constituents exhibiting similar n, yet tunable E_g values.

Furthermore, the variation of E_g as a function of n for all the heterostructures as compared to single layer TiO_2 films has been visualized. Figure 5.10 summarizes the E_g values as a function of n at 1030 nm wavelength for various compositions; N_T stands for the number of TiO_2 PEALD cycles in the compositions. At first sight, the bandgap is inversely proportional to the refractive index. A plateau is observed in terms of engineering new materials with simultaneously the highest possible bandgap and refractive index combination since the fundamental relation between the refractive index and the bandgap is preserved [164, 165]. At the bottom right corner, the brown coloured boxes denote pure TiO_2 films having n about 2.3 and E_g around 3.3 eV along with a slight increase in E_g with decreasing thickness. It is clear that, in order to achieve a heterostructure with higher n, the barrier thickness requires to decrease, whereas, for a higher E_g composition, the quantum well thickness needs to be reduced which is simultaneously the essential criterion for creating optical quantizing structures. The tunability of n and E_g in the heterostructures are limited by the properties of the constituent materials, i.e., n of the high index material and E_g of the low index material, respectively.

Notably, a closer look reveals that the optical bandgap can be widely tuned based on the confining structures. For example, the various heterostructures with a 1:2 PEALD cycle ratio (i.e., [1:2], [2:4], [4:8], [8:16], [16:32] nanostructures) have n of about 1.91 eV, but E_g varies from 3.45 to 3.75 eV, which corresponds to approximately 10% tunability in E_g. Additionally, the chemical integrity of the oxides can be inferred to reach a limit at around 4 cycles for Al_2O_3 and 4 cycles for TiO_2, corresponding to 5 Å and 1 Å, respectively. Figure 5.10 reveals the essence of synthesizing new ternary oxides by precise tuning of the compositions, especially, e.g., [4:4], [2:2] and [1:1] materials, having n ≈ 1.8 and E_g values between 3.8 -3.9 eV. It indicates on reaching a limit to the formation of new tailored composite oxide materials, as successfully enabled by PEALD.

Recent studies by Steinecke et al. [54] reported on predicted phase diagrams of quantizing nanolaminates by combining various oxides illustrating high flexibility in tuning optical properties of generated metamaterials. In the context of optical quantizing structures, our study demonstrates the experimental realization and control of optical properties in such structures consisting of Al_2O_3/TiO_2 prepared by PEALD technique. For single layer TiO_2 films addressed in Table 5.1, E_g values are estimated to be ≈ 3.3 eV, which have a decreasing trend with increas-ing thickness. In the heterostructures, it is evident that E_g not only depends on the ratio of the constituent oxides, but also on the material structure. The variation in optical bandgap with the quantum well thickness has been presented in Figure 5.11(a). This shows a similar trend as observed in quantizing oxide-semiconductor superlattices composed of a-IGZO/a-Ga_2O_3 reported by Abe et al. [166] or SiO_2/Ta_2O_5 [53] and TiO_2/SiO_2 [54] based dielectric nanolaminates.

Figure 5.11(a) illustrates the bandgap evolution from the perspective of creating quantizing heterostructures. The numbers on the graph in Figure 5.11(a) indicate the individual Al_2O_3 PEALD cycles N_A corresponding to N_T values.

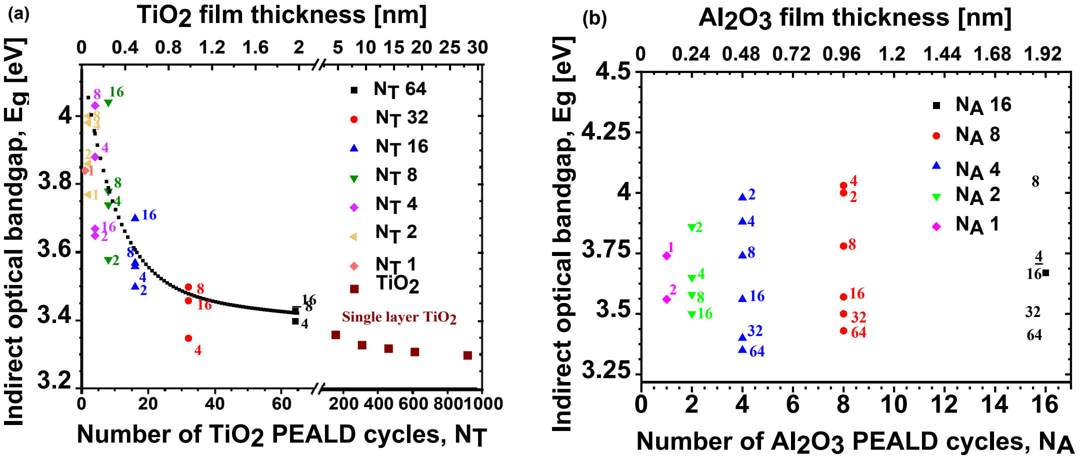

Figure 5.11: Bandgap of thin films as a function of (a) the quantum well thickness and of (b) the barrier thickness. N_T and N_A indicate the individual number of TiO_2 and Al_2O_3 PEALD cycles used while growing the heterostructures. The lower x-axis depicts the number of PEALD cycles, and the upper x-axis denotes the corresponding film thicknesses.

The increase in the optical bandgap with decreasing quantum well thickness is governed by the Kronig-Penney model while solving the eigenvalues of the quantizing nanolaminates [53, 54, 167]. Significant quantum confinement is observed for quantum well thicknesses below 1 nm with values up to approximately 0.7 eV (≈ 25% tunability) higher than the bandgap of single layer TiO_2 films. Finally, it is interesting to explore how much the barrier thickness can be reduced, while still enabling quantum confinement. Additionally, it is also questionable, how the structural integrity of the oxides (both barrier and quantum well) will influence the optical properties of the superlattices and its impact on the confinement effect. Figure 5.11(b) depicts the influence of the barrier thickness depending on various quantum well thicknesses (the numbers in the graph show N_T values for the corresponding N_A values). Reducing the barrier layer thickness below 1 nm (for instance, by reducing the number of Al_2O_3 PEALD cycles to 8, 4 and 2) still provides confinement. While the bandgap of the [8:16], [4:16], and [2:16] mixtures is higher than single layer TiO_2 systems, the probability of electron tunneling could be higher as compared to the thicker barrier layers. This study predicts that a barrier thickness of approximately 1 nm or slightly less is necessary to observe the influence of quantizing effects. The heterostructure films discussed here provide an experimental platform to clarify these issues since the individual oxides have a well-controlled growth rate with a sub-nanometer precision.

5.3 Application of dielectric heterostructures

- Demonstration of antireflection (AR) coatings at 355 nm

Here, an application in optical coatings has been demonstrated by employing these artificially engineered heterostructures. An antireflection coating has been designed for 355 nm using the OptiLayer software (version 12.83g, OptiLayer GmbH, Garching, Germany). The 355 nm is an important wavelength for various laser applications being the third harmonic wavelength of the NdYAG laser. Al_2O_3/TiO_2 heterostructures are considered as the high n material, whereas SiO_2 has been employed as the low n material. The SiO_2 process has been optimized in our previous work [120] using 3DMAS and O_2 plasma as precursors, as mentioned in Chapter 3. The GPC of PEALD SiO_2 at 100°C is about 1.15 Å/ cycle. The GPC corresponding to heterostructures is calculated using the single layer GPC values. For example, the GPC of [16:16] heterostructure process is calculated as:

$$\frac{(16 \times Al_2O_3 GPC + 16 \times TiO_2 GPC)}{(16 + 16)}.$$

Two compositions having relatively higher E_g values, for instance, [16:16] ($n \approx 1.8$, $E_g \approx 3.7$ eV) and [4:8] ($n \approx 1.9$, $E_g \approx 3.75$ eV) have been chosen for simulating the design. The AR design is elaborated in Table 5.4.

Table 5.4: Design of AR coatings for 355 nm wavelength using two different Al_2O_3/TiO_2 heterostructures and SiO_2 layers.

Materials	AR D1 (nm) using [16:16] composition	AR D2 (nm) using [4:8] composition
Al_2O_3/TiO_2	10.2	7.8
SiO_2	156.3	151.3
Al_2O_3/TiO_2	35.8	24.4
SiO_2	70.4	69.7

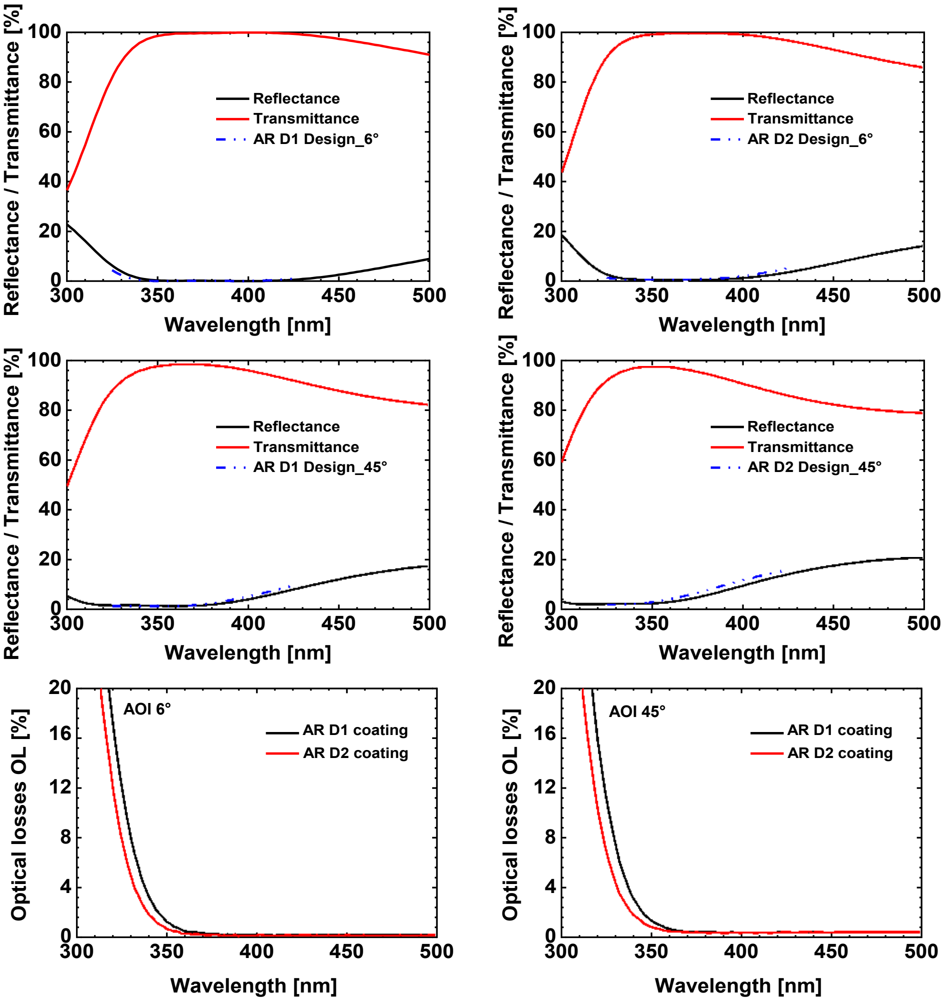

Figure 5.12: Reflection R (black) and Transmission T (red) spectra of AR D1 and AR D2 coatings in comparison with corresponding designs (blue dash) at an AOI of 6° (top panel) and 45° (middle panel), respectively. The bottom panel depicts optical losses OL of the AR coatings at an AOI of 6° and 45°.

Upon implementing these AR coatings, it is observed that the transmission at 355 nm has been enhanced up to 99%, simultaneously decreasing the reflectance below 1%, as shown in Fig. 5.12. Measurements at 6° (Figure 5.12, top panel) and 45° (Figure 5.12, middle panel) angle of incidence (AOI) demonstrate a wide-angle AR response. As well, Figure 5.12 (bottom panel) highlights no significant optical losses in spite of the presence of TiO_2 in the design, even at higher AOI. These observations successfully imply that heterostructures can overcome the limitation of low bandgap dielectric TiO_2 for applications in the UV spectral range.

5.4 Discussions

This chapter represents a comprehensive study on engineering the optical properties, e.g., dispersion relation and optical bandgap, by creating atomic-scale heterostructures of two technologically relevant oxides, namely Al_2O_3 and TiO_2. These served as model systems as their characterizations are relatively simple with available equipments in the optical laboratories. Upon developing uniform, dense, precisely controlled PEALD processes of Al_2O_3, TiO_2 films, and corresponding nano-heterostructures, challenges of obtaining eficient and reliable characterizations of such ultrathin interfaces are addressed. For the single layer TiO_2 films, a promising agreement between XRR and SE measurements demonstrates the suitability of SE for characterizing ultrathin films. Moreover, an excellent agreement between Cauchy and Cody-Lorentz SE models for the Al_2O_3/TiO_2 heterostructures ensures the successful estimation of their absorption edges. Additionally, XRR and XPS analyses on heterostructures reinforce Angstrom level composition-controlled growth of interfaces and demonstrate that the desired chemical properties are maintained. To gain further insight, the Bruggeman's approach is implemented to theoretically estimate effective refractive indices of the composites, which in turn exhibits a reasonable agreement between experimental measurements and simulations. Following this, an exciting set of compositions reveal distinct blue shifts in the absorption edge when the TiO_2 (quantum well) film thickness becomes comparable or less than ≈ 0.5 nm embedded in 2 nm of Al_2O_3 (barrier) film thickness. This phenomenon firmly indicates the creation of electronic and optical confinement in quantum well structures consisting of Al_2O_3/TiO_2 interfaces due to an extremely reduced out-of-plane thickness of the well material. Furthermore, the feasibility of the prepared heterostructures for application in optical coatings in UV spectral range has been demonstrated.

Additionally, a detailed study was carried out on other technologically relevant oxide interfaces made of HfO_2 and SiO_2 layers. Optical properties of HfO_2/SiO_2 heterostructures exhibit extended transparent regime, and tailored refractive indices enabling improved laser induced damage threshold in nanosecond pulse regime. Their characterizations have been however more challenging since their optical bandgaps must be determined by measurements in the vacuum UV (VUV) spectral range. This is available only in dedicated facilities such as the Physikalisch-Technische Bundesanstalt (PTB), Berlin.

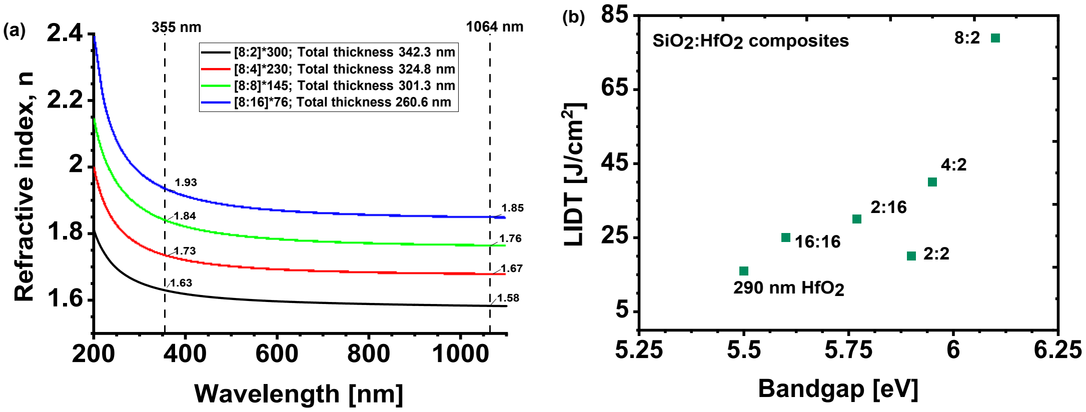

Figure 5.13: (a) Refractive index n curves of HfO_2/SiO_2 heterostructures with increasing HfO_2 content for 8 cycles of SiO_2. Tailored refractive indices are obtained by precisely mixing two oxides. (b) Laser induced damage threshold (LIDT) of selected HfO_2/SiO_2 heterostructures at 355 nm wavelength for 7 ns pulses as function of their optical bandgap values.

Exemplary, Figure 5.13(a) depicts the tailoring of refractive indices n, for instance from 1.6 to 1.9; and consequently the optical bandgap by means of precise composition control of the grown HfO_2/SiO_2 heterostructures. Figure 5.13(b) illustrates the realization of improved laser induced damage threshold (LIDT) of selected compositions measured at 355 nm using 7 ns laser pulses in comparison with single layer HfO_2 films. The observations on HfO_2/SiO_2 heterostructures have been documented in detail in our recent publication [168]. Overall, these systematic studies certainly elevate the advantages of ALD for producing superior interfaces at an atomic scale enabling multitude of new functionalities.

Chapter 6

Metal-dielectric atomically thin heterostructures

In this chapter, a detailed research on the growth and properties of atomic scale heterostructures of metal-dielectric systems based on Ir and Al_2O_3 is presented. This chapter outlines a comprehensive study on the growth, structural, chemical, linear, and nonlinear optical properties of these heterostructures. These investigations open up the possibility of designing new alternative nonlinear optical materials based on such interfaces. Further, an application in future PHz optoelectronics has been briefly demonstrated.

6.1 Growth of Ir/Al_2O_3 heterostructures

Metals have been an integral part of the development of human civilization. Naming various pre-historic eras, viz., copper age, bronze age, and iron age, after different metals emphasizes that the metals play an extremely important role in the evolution of human societies in general. Therefore, for ages, society has made continuous efforts to manipulate and expand the range of applications from metals.

Coming to the modern-day research questions, it remains a challenge to develop continuous metallic films with very small thickness, of the order of around 1-2 nanometers using various state of the art thin film deposition techniques. This achievement could lead to the realization of new electrical, optical, and plasmonic properties of metallic layers [55–57, 59]. Several approaches have been implemented to develop smooth metallic layers by decreasing their percolation length, for instance, using various transition metal seed layers [56, 57, 59, 61, 169], semiconductor seed layers made of Ge [170], combining template stripping and patterning [171]. Physical vapour deposition (PVD)-based processes were developed to grow thin metal films of Ag [56], Al [59], Au [57], Cu [172, 173], Cr [174], Ir [175, 176], Ti [172], and the list goes on. Ensuring the uniformity of film growth on a reasonably large area is also a challenge.

Over the past two decades, the ALD method has been extensively implemented for developing noble metallic thin films due to its inherent ability to control the thickness and composition of the films, along with a promising uniformity. Research efforts have been made to prepare a plethora of metallic thin films [177,178], for example, Ag [179–181], Au [182–184], Cu [185], Os [186], Pd [187], Pt [188,189], Ir [61, 190, 191], Rh [192], Ru [188, 193, 194]. Exclusively, noble metal Ir has also been studied using PVD [62, 175, 176, 195, 196] and ALD (different precursors: $Ir(acac)_3$ [61, 62, 190], IrF_6 [197], Ir(CpEt)(COD) [198], Ir(CpMe)(CHD) [199], Ir(CpEt)(CHD) [200]) based growth methods. However, the question of obtaining ultrathin smooth metallic layers preventing their island-type growth characteristic still persists. In this dissertation, a metal-dielectric heterostructure strategy has been introduced to examine the alteration in the growth mechanism of noble metal Ir at an atomic scale. Alumina (Al_2O_3) has been chosen as the dielectric component of the heterostructure because of its stable growth in a wide temperature window. The properties of the interfaces along with the structural integrity of ultrathin metallic systems have been thoroughly investigated to comprehend the growth behaviour of the metal-dielectric heterostructures at an atomic scale using ALD processes.

The atomically thin heterostructures of Ir/Al_2O_3 have been developed on Si wafers and fused silica substrates. The ALD equipment, and process parameters for preparing Ir and Al_2O_3 layers are thoroughly described in Chapter 3.2. The corresponding growth per cycle (GPC) values of Ir and Al_2O_3 were 0.6 Å/cycle [61] and 0.9 Å/cycle, respectively. A detailed study on the growth and properties of Ir nanoparticles and ultrathin layers has been presented in our previous work [61]. Upon developing single layer Ir and Al_2O_3 ALD films, two sets of heterostructures have been prepared. In these heterostructures, Al_2O_3 ALD cycles (i.e., spacer layer thickness) have been kept at 35 and 15 cycles, corresponding to approximately 3.5 nm and 1.5 nm Al_2O_3 thicknesses. The number of Ir ALD cycles was varied as 2, 4, 8, 16, 32, 64, and 128 cycles, respectively. The stack has been repeated to achieve at least a minimum of about 120 nm thickness in order to ensure reliable characterizations. For example, the sample named as [4:35]*102, stands for 4 cycles of Ir, followed by 35 cycles of Al_2O_3, and the stack is repeated for 102 times. This notation is followed throughout this chapter.

Following this, a systematic study has been conducted to understand the influence of Ir content on the properties of the heterostructures. Our previous study dealt with the understanding of the nucleation behaviour and film formation of noble metal Ir using ALD technique. We prepared ALD coatings of Ir by varying ALD cycles from 30 to 200 on various substrates. Initially, nanometer-sized Ir islands were formed, with the diameter of nanoparticles ranging from 5 to 15 nm. Exemplary, Figure 6.1 depicts the SEM micrographs of Ir coatings using 30, 75, and 200 ALD cycles on Si wafer and fused silica substrates. On further increasing the number of ALD cycles, these islands expand and start forming a percolating network; as a consequence leading towards the growth of closed metallic layers.

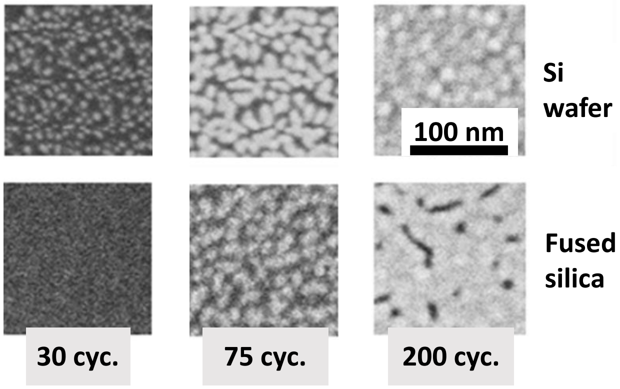

Figure 6.1: Scanning electron micrographs (SEM) of Ir coatings with different ALD cycles on Si wafer and fused silica substrates [61].

The aim of this dissertation was to further explore the growth of noble metal

Ir at an atomic scale. In order to visualize the evolution of surface coverage of Ir during the ALD growth, scanning tunneling microscopy (STM) investigations have been carried out for a coating with 4 Ir ALD cycles grown on gold-coated mica substrate. Figure 6.2(a) shows the STM micrograph of 4 Ir ALD cycles on

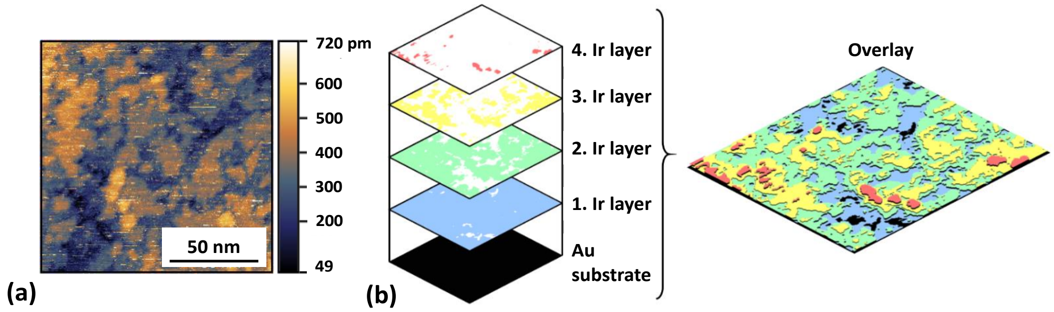

Figure 6.2: (a) Scanning tunneling microscopy (STM) image of 4 ALD Ir cycles deposited on Au(111) coated mica substrate. The scan area is 130*130 nm^2. (b)Analysis of the corresponding STM micrograph. Atomically thin Ir layers were reconstructed based on the height profile of the STM image. The overlaid image provides a visual perspective of the STM image.

Au(111)/mica substrate indicating a smooth Au substrate with a variation of Ir thickness over the substrate surface. Following this, based on the height profiles, atomically thin Ir layers were reconstructed using the ImageJ software. In Figure 6.2(b), the Au substrate is denoted by black. In addition, the coloured regions imply the estimated Ir layers on top of each other, whereas the uncoated regions are drawn in white. For instance, the lowest Ir layer directly on the substrate is denoted by a blue colour, and the remaining uncoated area is minimal. The second Ir layer on top of the first Ir layer is denoted by a green colour; the rest uncoated area is marked white. This colour scheme is followed for 4 Ir layers that could be identified after 4 ALD cycles. The overlaid image provides a visual perspective based on this STM analysis demonstrating around 97% surface coverage after 4 ALD cycles of Ir. This is in contrast to our a-priori observation of Ir nano-islands from 30 ALD cycles onwards, as shown in Figure 6.1 [61]. The first Ir layer directly on the substrate has the highest surface coverage behaving as an initial wetting layer. Upon further increasing the number of ALD cycles, a discrete accumulation of Ir on preferred substrate regions has been observed. The surface coverage is gradually decreasing, leading to the case of Stranski-Krastanov growth mode, i.e., islands on the top of the first monolayer. This enables the growth of a nearly metallic monolayer for precise layer-by-layer heterostructures provided by ALD. Additional STM measurements were also attempted on Ir film on Al_2O_3 coated Au(111) substrate; however, no signal was observed.

6.2 Structural and chemical properties

In order to obtain a deeper understanding of the structural properties of Ir/Al_2O_3 heterostructures, X-ray reflectometry (XRR) and grazing incidence X-ray diffraction (GIXRD) techniques have been applied. Coming to the heterostructures with the lower number of ALD cycles, i.e., 2, 4, 8 cycles, Ir nanoparticles have been presumed to be embedded in dielectric Al_2O_3 matrix, based on the Volmer-Weber island type growth mechanism [61]. Surprisingly, the XRR analysis depicts a Bragg peak at about 2.8° even for the 2 cycles of Ir contribution as illustrated in Figure 6.3(a), indicating a typical layered structure. This interpretation is even more evident from the HRTEM micrograph of [4:35]*50 sample indicating periodic bilayer structure of Ir/Al_2O_3 stacks in Figure 6.3(b). The dark layers denote Ir and the bright layers display Al_2O_3.

In addition, GIXRD measurements have been performed on a selected set of compositions as illustrated in Figure 6.4. These heterostructures show no presence of XRD peaks indicating an amorphous growth of Ir/Al_2O_3 nanostructures. Only for a relatively thick Ir (32 ALD cycles, ≈ 2 nm) and ultrathin Al_2O_3 (5 ALD cycles, ≈ 0.5 nm) individual contributions, XRD peaks corresponding to Ir are visible. These layers with 32 Ir ALD cycles (≈ 2 nm) are polycrystalline. All heterostructures with 35 cycles of Al_2O_3 spacer layers are amorphous, as observed by the GIXRD measurements. Consequently, it indicates that the spacer film thickness of 3.1 nm is suficient to inhibit the crystallization of ultrathin Ir layers.

From the XRR and HRTEM investigations, an intermixing of Ir and Al_2O_3 along the interfaces has been predicted for very thin Ir contributions. To elucidate the bonding environment for such ultrathin heterostructures, two samples were

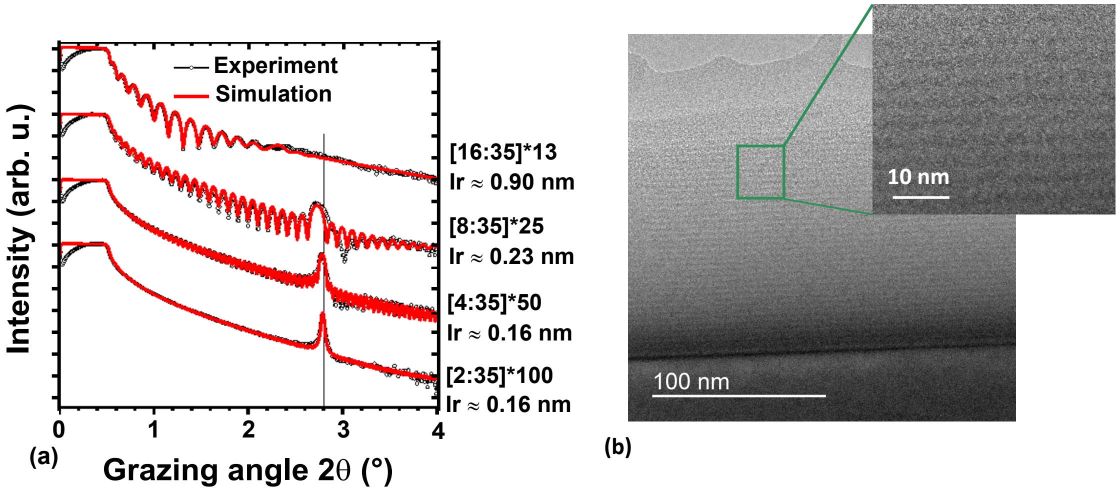

Figure 6.3: (a) X-ray reflectometry (XRR) measurements and simulations on selected heterostructures, (b) High-resolution transmission electron micrograph (HRTEM) of [4:35]*50 sample.

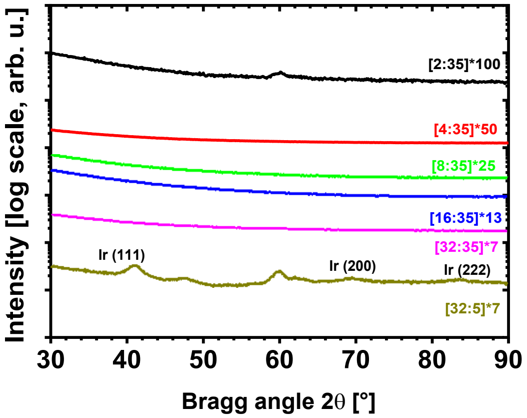

Figure 6.4: Grazing incidence X-ray diffraction (GIXRD) measurements on a selected set of Ir/Al_2O_3 heterostructures. The heterostructures with 35 cycles of Al_2O_3 are amorphous in nature, whereas 5 ALD cycles of Al_2O_3 led to the crystallization of Ir layer.

exclusively prepared making them suitable for X-ray photoelectron spectroscopy (XPS) measurements. It is essential to obtain the extent of the metallicity of these nanostructures. The designs of the structures were as follows,

- (Ir 2 cycles : Al_2O_3 35 cycles)*3 + Ir 2 cycles + Al_2O_3 20 cycles
- (Ir 16 cycles : Al_2O_3 35 cycles)*3 + Ir 16 cycles + Al_2O_3 20 cycles.

A single layer Ir film with 200 ALD cycles has been investigated as a reference. In Figure 6.5, the compositions are denoted with '4' times of repetition to keep the notation short and consistent as before.

It was necessary to prepare the layer stacks with few bilayers and an ultrathin Al_2O_3 (20 ALD cycles ≈ 1.8 nm) layer on the top to reduce the spectral shift in XPS due to charging effects. The top Al_2O_3 layer was made with 20 cycles instead of 35 cycles (≈ 3.1 nm) as the latter was too thick for the photoelectrons due to the limited escape depth. On the other hand, the top Ir layer is necessary to be overcoated with the ultrathin Al_2O_3 to incorporate a sandwiched Ir layer in between the Al_2O_3 layers to establish a similar bonding environment as that of the thicker stacks.

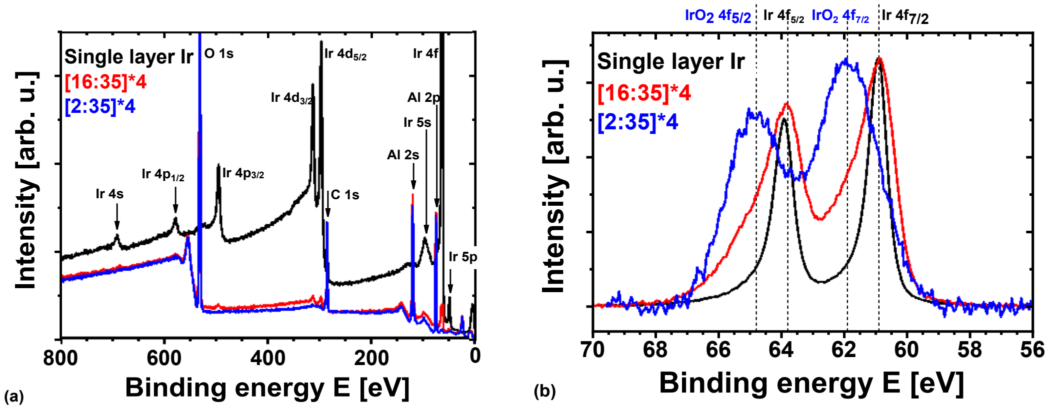

Figure 6.5: X-ray photoelectron spectroscopy (XPS) of Ir/Al_2O_3 heterostructures in comparison with a single layer Ir coating of approximately 10 nm. (a) 0 - 800 eV binding energy range and (b) zoomed in for the range of 56 - 70 eV showing exclusively the contributions from Ir 4f states.

Figure 6.5(a) illustrates the peak intensity vs. the binding energy curves over the available energy range from 0 to 800 eV, whereas, Figure 6.5(b) focuses on an interesting range of binding energies from 56 to 70 eV corresponding to the Ir 4f energy states. In Figure 6.5(b), pristine Ir film depicted by the black curve displays the contribution from Ir $4f_{7/2}$ and Ir $4f_{5/2}$ states respectively with an excellent agreement with the literature values [201–204]. The red curve denotes a heterostructure with 16 cycles of Ir (≈ 0.9 nm), where the XPS profile corresponds very well with the pure Ir 4f states. Mainly metallic Ir bonding state is prevalent; however, a contribution towards higher binding energies indicates the subtle presence of Ir-O-Al bonding environment. A quantitative analysis shows approximately 68% metallic and 32% oxidic chemical composition. This chemical composition can be interpreted as about 16% of oxidation along the Ir/Al_2O_3 interface on each side. For instance, in the case of the [16:35]*4 heterostructure, about 1-2 monolayers of Ir are assumed to be oxidized along the interfaces with Al_2O_3 on both sides. Upon further decreasing the Ir contribution to 2 cycles, i.e., approximately 0.1 nm, denoted by the blue curve, we obtain a significant shift towards higher binding energies suggesting the presence of an Al-O-Ir-O-Al bonding state. The bond length of Ir-Ir is about 2.7 Å, therefore, compositions having 2, 4, and 8 cycles of Ir mainly consist of O-Ir-O bonded layers, whereas with 16 cycles of Ir (0.9 nm), 2-3 metallic stacks are sandwiched between Ir-O bonded monolayers. The bond-dissociation energies of Ir-Ir, Ir-O, and Al-O are 361± 68 kJ/mol, 414±42 kJ/mol, and 501 ± 10 kJ/mol, respectively, indicating a possibility of Ir-O bond formation at the Ir/Al_2O_3 interfaces [205]. These inspections enable to probe the growth and structure of the Ir/Al_2O_3 heterostructures.

6.3 Optical properties

6.3.1 Linear optical properties

To explain the heterostructures from an optical perspective, various state of the art investigations have been implemented. The transmission T, reflection R, and optical losses OL spectra of the Ir/Al_2O_3 heterostructures are demonstrated in Figure 6.6. The upper and lower panels are for 3.1 nm and 1.4 nm spacer Al_2O_3 layers, respectively. The transmission spectra in Figure 6.6(a) show a gradual decrease in transmission as the Ir content is increasing. Initially, the transmission is quite similar up to 16 cycles of Ir inclusion with a gradual decrease, especially at the UV spectral region. For the compositions with 32 ALD cycles of Ir and higher, the transmission rapidly decreases indicating the rise of effective metallic character. For 128 Ir ALD cycles (≈ 7.6 nm) contribution, the stack becomes non-transparent owing to the formation of closed metallic layers creating nanolaminate

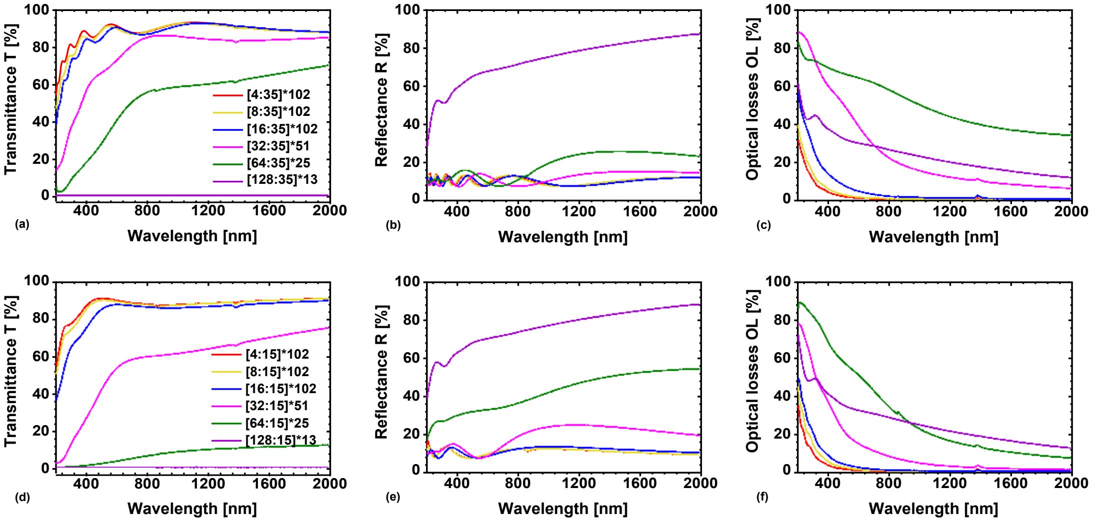

Figure 6.6: Transmission T (a, d), reflection R (b, e) and optical losses OL (c, f) spectra of the heterostructures with 35 cycles (upper panel) and 15 cycles (lower panel) of Al_2O_3 spacer layers, respectively.

structure, as discussed later in the SEM images.

The reflectance spectra shown in Figure 6.6(b) also indicate metallic character for samples with more Ir content, as given by the distinct increment observed in [128:35]*102 sample exhibiting a metallic reflection. In the case of the structures with 1.4 nm spacer layer thickness (lower panel Figure 6.6(e)), the reflection spectra already start depicting distinguishable metallic features even with relatively low content of Ir. The reflection spectra look similar up to 16 cycles of Ir content indicating a dielectric behaviour. Further from 32 ALD cycles onwards, a strong increase in R occurred finally leading to metallic reflection property for the heterostructures containing a higher amount of Ir. In addition, the transmission spectra behave more sensitively to the metallic character than the reflectance curves. Initially, up to 16 ALD cycles of Ir contribution, as denoted by the red, yellow, and blue curves in Figure 6.6(d)), T is relatively high like an effectively dielectric system; a visible decrease is observed in the UV spectral range. With increasing Ir content, T decreases rapidly leading to a non-transparent metallic stack for the 128 ALD cycles of Ir composition. It is observed from the UV/VIS spectrophotometry measurements that the Ir/Al_2O_3 heterostructures undergo an effective dielectric to metal transition with increasing Ir contribution, and the critical Ir thickness for the transition is within 32 to 64 ALD cycles (≈ 2 to 4 nm).

The corresponding optical losses OL, i.e., (100 - (T+R)), are plotted in Figure 6.6(c) and (f), respectively. As depicted in the lower panel of Figure 6.6, the decrease in transmission is more rapid than that of the thicker spacer layer systems. As well, the reflection spectra start exhibiting metallic nature already at 64 Ir cycles. Metallicity already emerged at a lower Ir content when the spacer thickness is smaller. However, for ultrathin Ir contributions (up to 16 cycles), even a 1.4 nm spacer layer has been the suficient barrier to attain a partially metallic character of the heterostructure stacks, which will be more evident from the optical constants determined using spectroscopic ellipsometry (SE) method. The metallic contribution is however visible in the optical losses of the [16:15]*102 heterostructure. Its optical losses (mainly absorption) extend in the IR spectral range. This is in agreement with the XPS study showing about 68% metallic character for the heterostructure with 16 cycles of Ir.

- Optical constants and heterostructure stack thickness

The linear optical constants and the total thickness of the heterostructure stacks have been determined by the SE technique. While obtaining the optical constants, each heterostructure was considered as an effective medium, as opposed to a layer-by-layer approach. The measured ellipsometric parameters ψ and Δ have been fitted by employing Drude-Lorentz oscillator model containing 3 to 7 Lorentz oscillators depending on the complexity of the system. An example of measured and fitted ellipsometry data has been presented in Figure 6.7 for the [128:35]*13 heterostructure. A promising agreement has been achieved between the simulation and experimental results. A similar fitting procedure has been carried out for all the heterostructures ensuring the lowest possible mean square error MSE values. However, the heterostructures with 32 and 64 cycles of Ir (i.e., ≈ 2 nm and 4 nm) were found to be the most challenging to model precisely because of being in the transition regime. Whereas modelling the heterostructures with an unambiguous dielectric or metallic character turned out to be more straightforward. Once an acceptable fit of the SE data was attained, the T, R spectra were

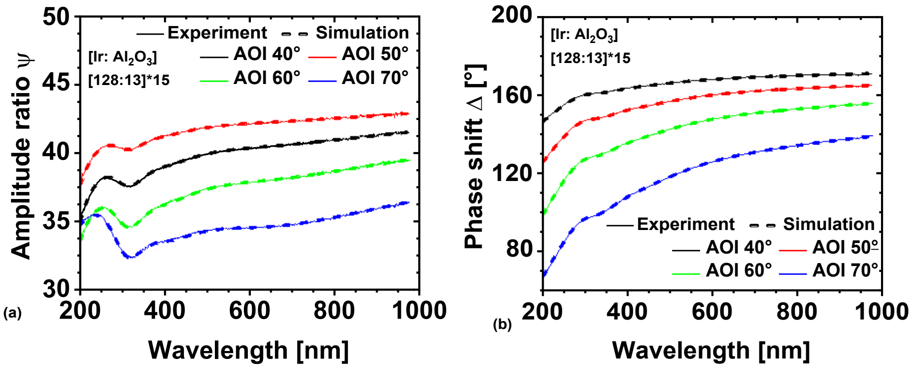

Figure 6.7: Experimental and simulated values of ellipsometric parameters at different angles of incidence (a) amplitude ratio ψ and (b) phase shift Δ. A case study is shown here for the [128:35]*15 heterostructure.

simulated from the oscillator models and compared to the measured T, R values. The fits of the SE data were only considered satisfactory if the simulated T, R values depict a reasonable match with the measured spectra. For instance, the T, R values of [8:35]*102 heterostructure have been simulated using the determined refractive indices from the SE measurements. The simulated T, R data is showing a reasonable agreement with the measured T, R values, as depicted in Figure 6.8.

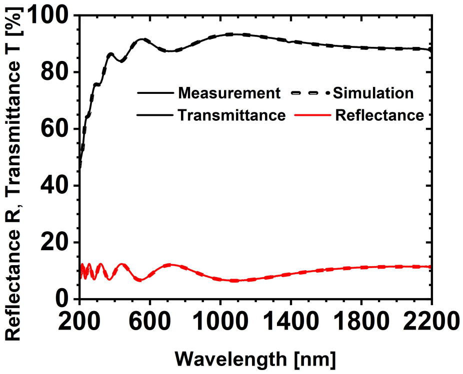

Figure 6.8: Comparison of the measured and simulated transmittance T and reflectance R data. The simulation has been performed using the fitted values of refractive indices n by employing spectroscopic ellipsometry. A case study is shown here for the [8:35]*102 heterostructure.

In order to ensure the determination of dispersion spectra as reliable as possi-ble, an example of the fitting procedure for the transition-regime heterostructure

[64:35]*25 is given in Figure 6.9. The measured T, R spectra with the corresponding OL are shown with solid curves, and the T, R, OL spectra derived from the fits of the SE measurements are shown in dashed curves. The wavelength range of the SE measurements was 200 to 980 nm; the derived T, R spectra consequently span a narrower spectral range than the T, R measurements, which were performed from 200 to 2000 nm wavelength range. Furthermore, the measured T, R data was also fitted with the Drude-Lorentz oscillator model, as shown with dash-dotted curves in Figure 6.9 (b). The optical constants were further derived

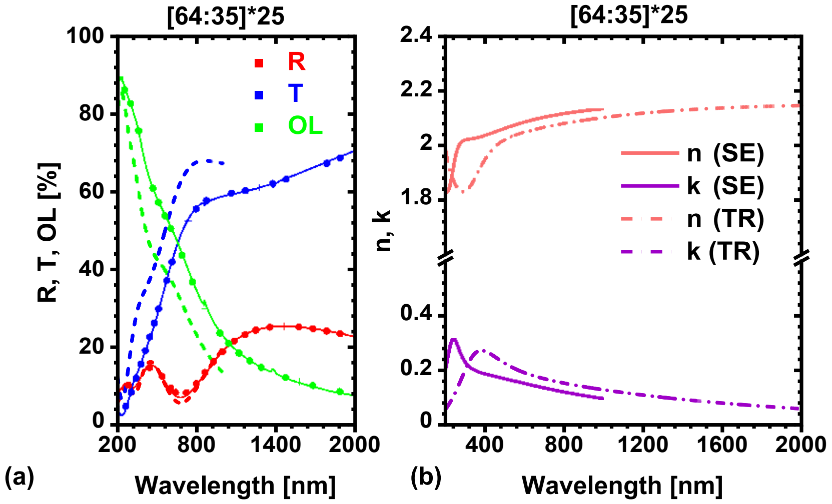

Figure 6.9: A case study with [65:35]*25 heterostructure sample. (a) Three data sets for the reflectance R (red), transmittance T (blue) and the optical losses OL (green) are compared; the measured T, R spectra (solid curves), fits of the T, R measurements (dotted curves). The T, R spectra simulated (dashed curves) from the oscillator model were used to fit the SE measurements. (b) The refractive index n (pink) and the extinction coeficient k (violet) spectra were derived from the SE (solid curves) and T, R fits (dashed curves), respectively.

from the T, R fits, generating a second set of n and k values in addition to the values derived from fitting the SE parameters. A comparison of the two data sets for n and k is shown in Figure 6.9(b). The optical constants from the SE fit are denoted by solid curves and the ones from the T, R fit are plotted in dash-dotted curves. The similarity between the two sets increases the confidence in the reliability of these models for obtaining dispersion spectra, as presented in the following. Discrepancies are mainly attributed to slight variations due to different substrates and the non-uniformity of film growth. Additionally, a discrepancy is observed in general in the investigation of the dispersion of absorbing materials by SE vs. spectrophotometry, even for the same sample. As seen in Figure 6.6, a slight variation of the Ir content between 16 to 64 cycles leads to a very large variation in T and OL, but relatively less for the reflection curves. Iridium nucleation and growth behaviours depend on the substrate material and at least the first few layers are prone to be influenced by the substrate. The non-uniformity also drastically affects the T and OL values. Variation of about 1-2 nm of Ir thickness could lead to an almost 10% change in transmission.

As observed for both spacer thicknesses, the refractive index spectra quite resemble that of Al_2O_3 for heterostructures having thinner individual Ir thickness (≈ up to 16 cycles, see Figure 6.10(a, c)). Figure 6.10(a, c) and 6.10(b, d) represent n and k dispersion spectra for the heterostructures with 35 and 15 Al_2O_3 cycles, respectively. Thereafter, a gradual increase in n and k have been observed since

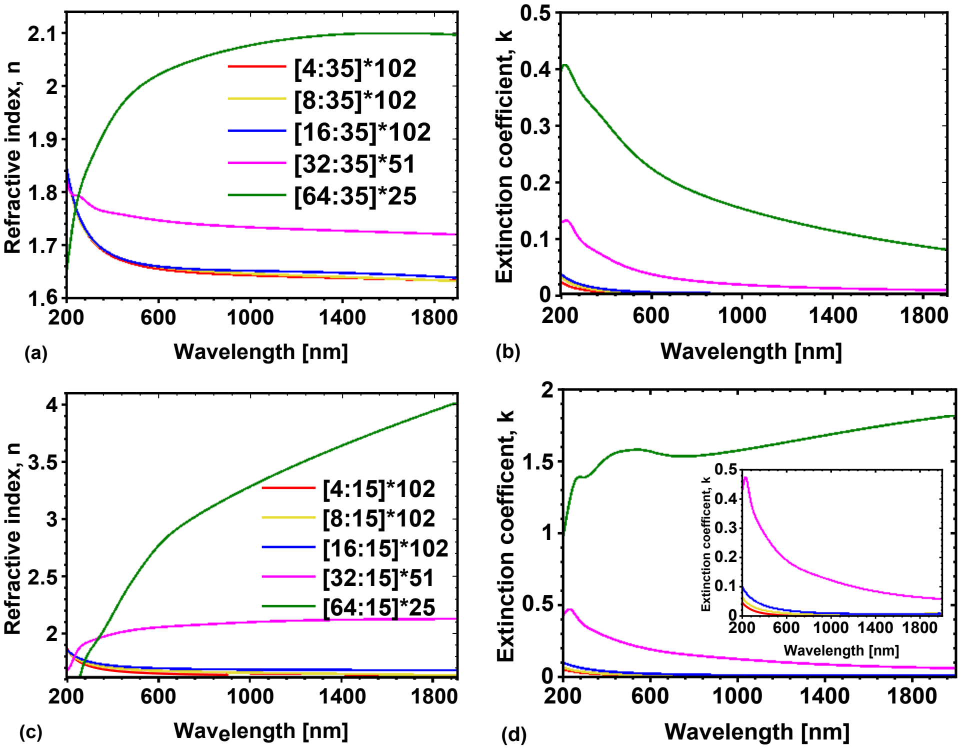

Figure 6.10: Refractive index n and extinction coeficient k spectra of various heterostructures having (a, b) 35 and (c, d) 15 ALD cycles of Al_2O_3 spacer layer.

the metallic character of the heterostructures starts predominating as the Ir cycles approach 32. Finally, with 128 ALD cycles of Ir, the refractive index n and extinction coeficient k possess a similar trend as of single layer Ir films (as plotted in Figure 6.13(a, d) in Chapter 6.3.2). The k values are initially slightly higher than single layer Al_2O_3 films, while following a similar trend, especially with a higher absorption near the UV spectral range, as confirmed by the higher optical losses in UV regime in the OL spectra in Figure 6.6(c, f) as well. The dispersion behaviour of k exhibits significant metallic character from the stacks with 32 ALD cycles of Ir onwards, even more pronounced for the thinner space layer systems. Hence, the critical Ir contribution for transiting from effectively dielectric to metal is supposedly within 32 to 64 cycles of Ir ($\approx$ 2-4 nm), which is also consistent with the observations from the UV/VIS spectrophotometry measurements.

Further, the variation of the effective dielectric function ϵ of the heterostructures has been examined. The real and imaginary parts of ϵ in the UV/VIS spectral range are depicted in Figure 6.11(a-d) for the heterostructures with 35 and 15 cycles of Al_2O_3, respectively. The stacks with low Ir content behave similarly to single layer Al_2O_3. With increasing Ir ALD cycles, e.g., at 32 cycles of Ir, the metallic character starts to influence the dielectric function of the heterostructures, whereby the $Im(\epsilon)$ is more sensitive to the Ir content. Subsequently, for the heterostructures with 128 cycles of Ir, a similar trend as of a single layer Ir film is observed. Noteworthy is the composition ratio at which the system is in the transition phase (in between the dielectric and metallic phase), i.e., the [64:15]*25 heterostructure. The real part of the dielectric function $Re(\epsilon)$ for [64:15]*25 heterostructure tends to zero at around 230 to 240 nm wavelength, as shown by the yellow-shaded region in Figure 6.11 (c). In materials, where $Re(\epsilon)$ approaches zero, i.e., at the epsilon-near-zero (ENZ) frequencies, a strong nonlinear optical response has been observed [206,207]. This heterostructure containing Ir and Al_2O_3 interfaces can therefore be a potential candidate for exploring an enhanced nonlinear optical response. However, the imaginary part of the dielectric function $Im(\epsilon)$ is relatively high, approximately around 4.2 to 4.6. The [64:15]*25 heterostructure also exhibited high optical losses of nearly around 90% for a thickness of about

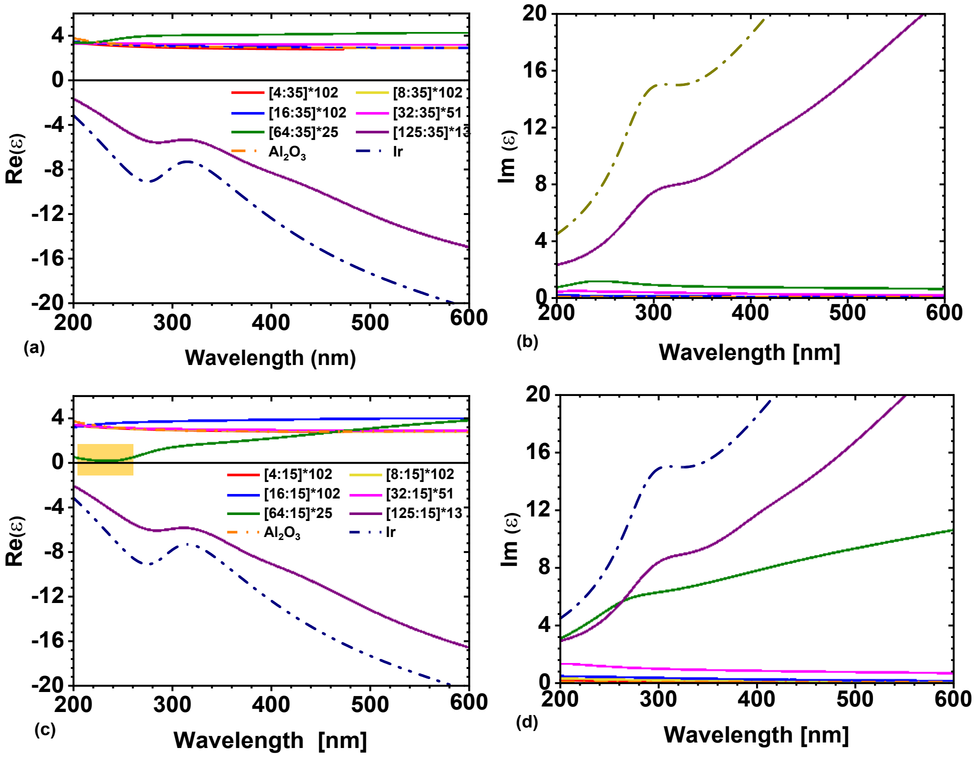

Figure 6.11: The real and imaginary part of the dielectric function (ϵ) of the heterostructures with (a, b) 35 cycles and (c, d) 15 cycles of Al_2O_3 spacer layers. The yellow-shaded region in (c) depicts the epsilon-near-zero (ENZ) behaviour of the [64:15]*25 heterostructure.

110 nm in its ENZ wavelength range, as seen in Figure 6.6 (f). High optical losses remain one of the largest obstacles faced in ENZ material development, which has led to criticism of the practicality of ENZ materials [208]. Several means have been attempted to compensate for the high optical losses observed in many ENZ materials, for example, by combining the ENZ material with a dielectric in a multilayer structure [98, 99, 209] or by doping the ENZ material with a gain-medium [210]. This opens the scope of future research in designing and developing new nonlinear optical materials.

While evaluating the thickness and roughness of the heterostructures, the calculated and determined stack thickness (by means of SE, XRR, and SEM techniques) along with measured r.m.s. surface roughness for all the heterostructures are listed in Table 6.1. In general, the SE technique has been considered to be one of the most reliable methods to determine the total stack thickness. The thickness

Table 6.1: Comparison of determined film thickness by different methods and r.m.s surface roughness of various Ir/Al_2O_3 heterostructures. The evaluated thickness below is calculated from the single layer GPC values.

Compositions $[Ir:Al_2O_3]$*N	Volume fraction of Ir (%)	Evaluated thickness (nm)	Film thickness (nm)			Roughness r.m.s (nm)
			SE	XRR	SEM	WLI
[4:35]*102	6	343.7	335.9	326.4	312.3	1.1
[8:35]*102	11	366.2	330.3	342.2	320.6	0.4
[16:35]*102	21	411.1	351.9	345.8	395.2	0.5
[32:35]*51	34	250.4	226.5	-	282.5	1.1
[64:35]*25	51	166.8	152.8	-	-	0.4
[128:35]*13	67	132.5	129.4	-	156.7	1.1
[4:15]*102	15	160.1	140.4	136.4	137.0	0.6
[8:15]*102	26	182.6	139.6	147.2	146.5	1.0
[16:15]*102	42	227.5	153.5	213.5	224.7	1.3
[32:15]*51	59	158.6	128.6	-	-	0.7
[64:15]*25	74	121.8	108.1	-	-	0.7
[128:15]*13	85	109.1	116.1	-	-	1.1

determination accuracy from the SE measurements is about ±1 nm. However, the samples with thick individual Ir layers having low T values are critical for precise SE measurements. SEM micrographs provide a rough estimation of the thickness, along with a visual cross-sectional appearance of the stacks. XRR method has also been applied on selected samples to probe the individual layer thicknesses, total stack thickness, and interface roughness. For the samples with higher Ir contributions, XRR measurements show a bad signal-to-noise ratio making them unsuitable for the fitting procedure. However, the heterostructures with thin Ir films could be reliably analysed by XRR (as observed in Figure 6.3). It is challenging to determine the total thickness of such atomically thin heterostructures. Overall, almost all the compositions turned out to be thinner than the expected thickness, indicating a possible nucleation delay of Ir on the Al_2O_3 sublayers, as observed in our previous study on nucleation of Ir on various substrates [61]. The thicknesses determined by SE and XRR are mostly consistent with each other and with the calculated (expected) thickness using individual GPC values of the constituents. Figure 6.12 portrays the SEM micrographs of selected heterostruc-

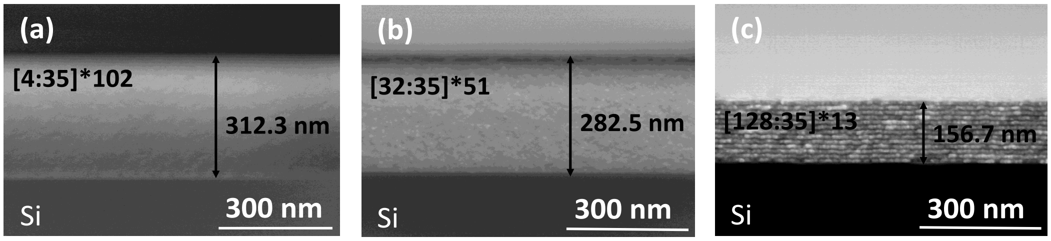

Figure 6.12: Scanning electron micrographs (SEM) of selected heterostructures; (a) [4:35]*102, (b) [32:35]*51, (c) [128:35]*13. For ultrathin Ir coatings (i.e., up to 32 cycles ≈ 2 nm), SEM could not resolve the heterostructures. In the case of heterostructure with 128 Ir cycles (≈ 7.6 nm), a layered structure is visible.

tures, (a) [4:35]*102, (b) [32:35]*51, and (c) [128:35]*13. At 32 cycles of Ir (≈ 2 nm) or lower, the heterostructures could not be resolved by SEM. In the case of 128 Ir cycles (≈ 7.6 nm), a layered heterostructure is visible. While estimating the stack thickness, SEM images show a bit of deviating thickness as compared to the calculated value. This result can be attributed to the measurement arti-fact or charging effects arose during the SEM imaging. The deviation is in the range of 10% among different techniques. Notably, the thickness of the compos-ites with large Ir content is probably underestimated by SE measurements, since their k-values are very large. These cross-validated investigations represent the robustness and thickness control of the ALD growth method, even when metal and dielectric are grown using a single ALD recipe. Remarkably, it maintains the superlattice nature of heterostructures even with interfaces repeated up to 102 times.

6.3.2 Effective medium approximation approaches

From a design perspective of thin film optical systems, it is essential to address the simulation of the optical constants for such heterostructures, based on the effective medium approximation (EMA) approaches in comparison with ellipsometry evaluations. Maxwell–Garnett (MG) and Bruggeman (BG) formalisms have been applied to numerically obtain an estimation of effective n and k-values of the heterostructures and compared to the experimental values obtained by SE in Figure 6.13. The MG model being based on the inclusion of a material in another host matrix, breaks down at a higher volume fraction f of the inclusion material, as the particle-particle interaction is not considered, and the model loses its validity. In contrast, the BG framework considers the system to be a homogeneous mixture of two materials. Figure 6.13 depicts a comparison of dispersion spectra determined

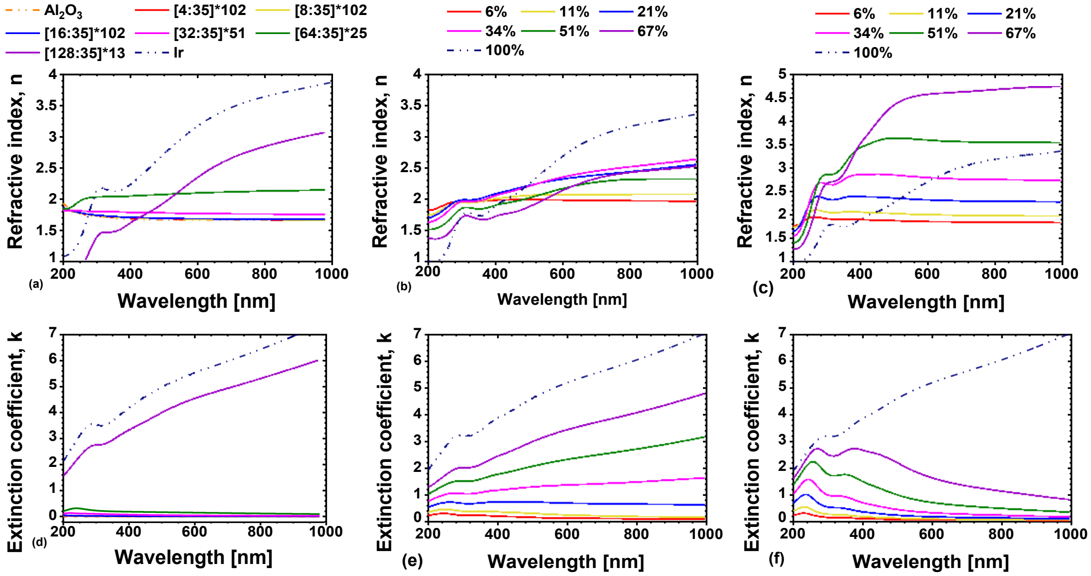

Figure 6.13: Comparison of dispersion spectra using the spectroscopic ellipsometry technique (left panel; a, c) and effective medium approximation based simulations. The evolution of n and k were simulated using Bruggeman (middle panel; b, e) and Maxwell-Garnett (right panel; c, f) models. The simulations were performed using different volume fractions of Ir corresponding to heterostructures mentioned in Table 6.1; all having 35 cycles of Al_2O_3 spacer layer. The corresponding volume fractions are mentioned in percentages above the plots of middle and right panels.

using ellipsometric measurements (a, d) and EMA simulations (BG: b, e and MG: c, f), respectively. In the right panel, Figure 6.13(c, f) illustrate the effective n and k simulated by MG approach. It shows an increasing trend in optical constants as the metallic influence increases, however, the model collapses as the f approaches close to 50%. On the other hand, the BG model (in Figure 6.13(b, e), middle panel) demonstrates an increasing trend of optical constants with increasing Ir cycles. However, the n spectra could not follow the experimental observations for the thickest Ir contribution (i.e., 128 cycles ≈ 7.6 nm). This can be attributed to the fact of generating closed Ir layers in Ir/Al_2O_3 nanolaminate systems leading to the breakdown of the mixture model assumptions.

Additionally, special attention was given to the [64:15]*25 composite due to its ENZ behavior. Figure 6.14 depicts the dielectric function of [64:15]*25 as

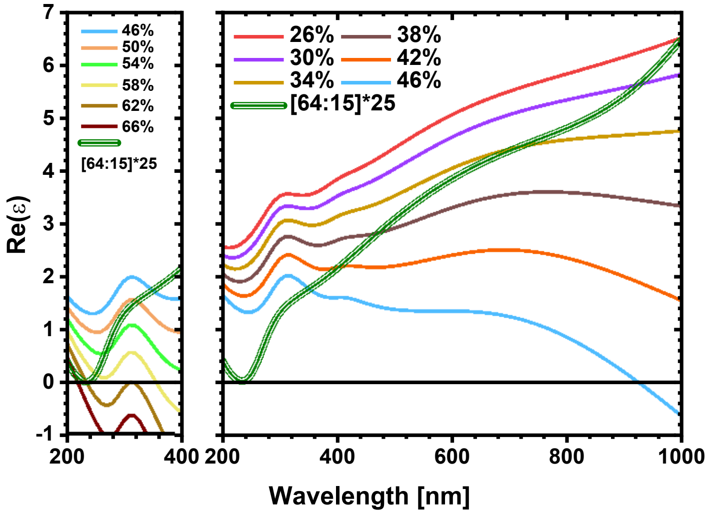

Figure 6.14: The real part of the dielectric function calculated according to Bruggeman's approach. The colored lines indicate various volume fractions of Ir using BG model. The deep green triple line represents the dielectric function of the [64:15]*25 heterostructure, derived from the fits of SE measurement.

derived from the SE measurement fits, alongside the EMA model based on BG formalism for selected amounts of Ir volume fractions. Figure 6.14 (left) zooms into the narrower spectral range of 200-400 nm targeting ENZ spectral range of the [64:15]*25 heterostructure, whereas, Figure 6.14 (right) covers the broader spectral response. The volume fractions chosen to be shown in the graphs are the ones that bear some resemblance to Re(ϵ) of the ALD-grown heterostructure. Although neither the BG model nor the MG model was able to accurately predict the behavior of the dielectric function of [64:15]*25. Considering the entire spectral range, the simulations that give the closest match to [64:15]*25 have a significantly lower Ir contribution than expected, taking into account that the Ir content of the fabricated heterostructure is roughly 50%. However, models with higher volume fractions of Ir are comparable to Re(ϵ) of [64:15]*25 when focus-ing on 200 to 400 nm wavelength. This emphasizes on how small changes in the composition ratio emerge in major shifts in the ENZ wavelength. A precise tunability of the composition ratio is thus crucial to achieve the ENZ behaviour at a targeted wavelength. It should be noted that this material model does not account for the partial oxidic bonding at the Ir-O-Al interfaces (see XPS spectra). Even though these simulations cannot precisely estimate the behavior of such heterostructures, they provide a reliable trend of Re(ϵ) with increasing volume fraction of the metal. Further improvement of the material modelling will be the scope of future research to facilitate the improved material design and fabrication for targeted ENZ applications.

6.3.3 Nonlinear optical properties

- Second harmonic generation (SHG)

Second harmonic generation (SHG) is one of the most widely studied nonlinear optical processes. It is a second order phenomenon which is forbidden in a medium having inversion symmetry. By employing a nanolaminate strategy, it has been possible to break the symmetry at the interfaces leading to surface SHG [94, 96, 97]. Here, the potential of obtaining SHG from periodic metal-dielectric stacks of Ir/Al_2O_3 has experimentally been investigated. A case study has been conducted using the heterostructures with $\approx$ 3.1 nm spacer thickness. The schematic diagram of the experimental setup [211, 212] is depicted in Figure 6.15.

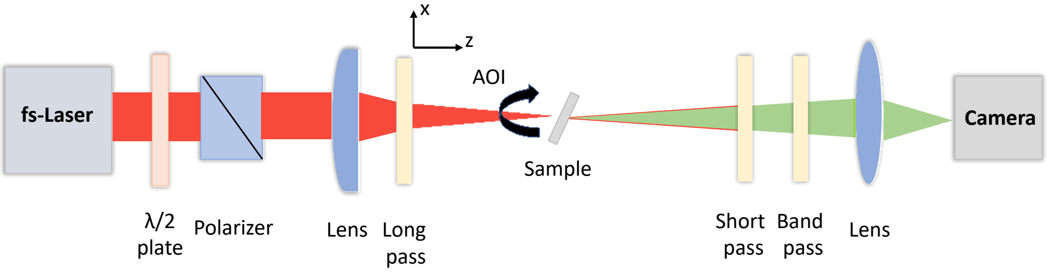

Figure 6.15: Schematic illustration of the characterization setup for second harmonic generation (SHG).

An ultrafast laser (PHAROS-SP by Light Conversion) of 200 fs short pulses at a wavelength of 1032 nm with a repetition rate of 200 kHz is incident on the sample through the polarizer and the half-wave plate. The beam is focused onto the sample to a beam diameter of 250 µm using a plano-convex lens of 400 mm focal length. The sample is placed on a rotational stage allowing to precisely vary the angle of incidence. The emitted light through the sample has been collected using a collector lens and finally detected by a CMOS camera. This is also set on a motorized stage to detect the SHG both in T and R modes. A set of short pass and band pass filters have been employed to selectively detect the second harmonic contribution at the detection unit. The uncoated fused silica substrate and single layer Al_2O_3 and Ir coatings were measured as reference samples. Initially, the output SHG signal is measured by varying the angle of incidence (AOI) from 0° to 80°, and eventually, the AOI for the highest output signal has been noted for each sample. The maximum signal has been observed in between around 55° to 70° AOI values for the samples. A relatively high AOI is required to facilitate the breaking of centrosymmetry for achieving the SHG signal. Following this, the output signal has been detected as a function of input power keeping the AOI fixed for the highest output signal. Data presented in the following are for the measurements using TM (transverse magnetic, i.e., $E^{(i)}$ is parallel to the plane of incidence)-polarized incident light, as it shows significantly higher output SHG owing to the exclusive out-of-plane nonlinear tensor components.

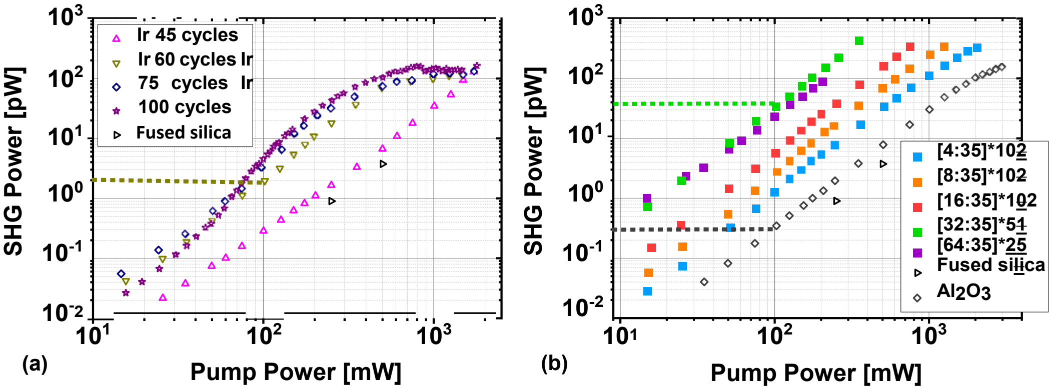

Figure 6.16: Second harmonic generation (SHG) power is plotted as a function of input pump power for (a) Ir nanoparticles of different ALD cycles, and (b) selected Ir/Al_2O_3 heterostructures. The depicted SHG measurements were performed in the TM-polarization mode of the incident beam. The heterostructure films show enhanced second order nonlinearity as compared to single layer Ir and Al_2O_3 coatings. The dashed lines denote the comparison of output SHG power values of different coatings at an input pump power of 100 mW.

Figure 6.16 demonstrates the evolution of output SHG power as a function of incident power for (a) Ir coatings and uncoated fused silica and (b) selected Ir/Al_2O_3 heterostructures. The plots are depicted in log-log scale and a linear fit of the measured data resulted in a slope of around 2. This confirms the presence of SHG from the coatings, as the output power shows a quadratic behaviour with the incident power. Our previous study reported that 45 ALD Ir cycles refer to Ir nanoparticles with approximately 20% surface coverage, whereas, 100 ALD Ir cycles lead to around 60% surface coverage [61], respectively. In Figure 6.16(a), an increasing SHG signal has been detected with an increasing number of Ir cycles. Further, the signal saturates rapidly as the metallic surface coverage increases, as demonstrated for samples with 60 to 100 Ir ALD cycles, which might be caused due to self-absorption. The slope of the SHG signal for the sample with 45 ALD Ir cycles is approximately 2, however, an increase in the slope of more than 2 is observed for Ir coatings with 75 and 100 Ir ALD cycles at relatively low pump power values. This enhancement is attributed to the thermal non-equilibrium between the electron gas and the lattice [213–215]. Moreover, the Ir coatings with a low surface coverage have a continuous, quadratic increase of the SHG signal up to 2 W pump power, which is the prescribed limit of the applied laser system. In contrast, the SHG signal of nearly continuous ultrathin Ir films indicates damage above 100 mW and saturation of the SHG signal. Hence, Ir samples with a low surface coverage (around 60 ALD cycles, i.e., less than 40% surface coverage) have more attractive SHG properties for applications in the transmission mode, due to a better stability.

Figure 6.16(b) illustrates that the SHG signal of the Ir/Al_2O_3 heterostructures experiences a linear increase from 4 to 16 cycles of Ir content. The SHG power is approximately doubled with the doubling of Ir ALD cycles. The contribution of the Ir in increasing the SHG signal could be attributed to the enhancement of the metallic character of the multilayer stacks. It seems that the entire SHG signal arises from the iridium component. Although the linear refractive index n and the extinction coeficient k have a very small variation for these three heterostructures (as demonstrated in the previous section), and accordingly, the transmittance of these compositions is also nearly identical between 400 to 1200 nm wavelength, a significant increase of their second order nonlinear response (SHG) has been observed with increasing Ir content. This indicates that the response of the electrons in the Ir atoms to the incident electromagnetic field is dominant. Interestingly, even though the number of interfaces is half in the [32:35]*51 heterostructure, and a similar total amount of Ir is grown, its SHG signal is nearly 5 times larger than that of the [16:35]*102 heterostructure. A higher Ir:Al_2O_3 ratio as in the [64:35]*25 heterostructure is not advantageous since the absorption losses start dominating and the transmitted SHG power decreases. The reproducibility of the results has been verified. Overall, it is evident that ultrathin metallic coatings incorporated in a dielectric matrix have one to two orders of magnitude larger SHG signal than single layer metallic films along with significantly improved laser stability in the heterostructures due to the reduced absorption despite a large metal content.

6.4 Application in ultrafast optoelectronics

These investigations are from a collaborative research with the Wigner Research Centre for Physics, Hungary. The study focuses on generating laser induced ultrafast current in the Ir/Al_2O_3 based metal-dielectric heterostructures. Conventional electronics is reaching the speed limit of about 1 THz. A new era of optoelectronic devices working in PHz regime has attracted huge attention. These devices are based on controlling the current on few femtosecond time scales [216, 217]. Here, few cycle carrier envelop phase (CEP) stabilized laser pulses have been implemented to create such ultrafast current. The laser excites the charge carriers at the metal-dielectric-metal interface. This effect has already been explored in some dielectric materials, e.g., HfO_2, SiO_2, and GaN [218]. The input pulse can be as weak as 300 pJ. However, the little gain achieved from the dielectrics encour-ages to look for new material systems to enhance the applications of the current control phenomenon. In this research, current control measurements have been performed on a selected set of ALD-grown Ir/Al_2O_3 heterostructures. Gold electrodes were patterned on the substrates. The slit size is about 1 µm between the two electrodes. This has been illuminated with few-cycle laser pulses up to 2.5 nJ, corresponding to the field strength of 0.4 V/Å on the target, with a repetition rate of 80 MHz. The schematics of the measurement procedure is illustrated in Figure 6.17(a). The CEP dependent current is detected in the connected electrical circuit using lock-in amplification. In the following expression, $J = G^{-1}V$, where the lock-in amplifier measures the voltage V, which can be converted to current J, by dividing by the gain factor G of the pre-amplifier [218].

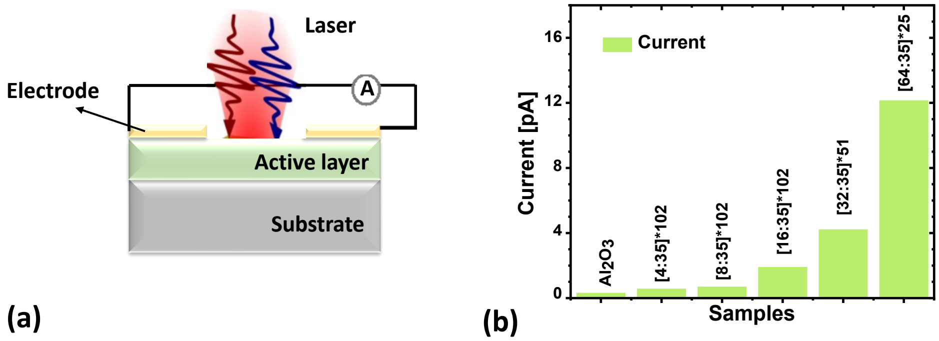

Figure 6.17: (a) Schematics of the measurement setup of ultrafast current generation. A focused laser beam is impinging on the active layer. Here, selected Ir/Al_2O_3 heterostructures have been investigated as active layers. (b) The maximum generated current as function of increasing Ir content in the heterostructures indicates an increasing trend in generated current with thicker metal interlayer.

The Ir/Al_2O_3 heterostructures having different individual Ir contributions are measured with a position scan. The maximum current generated in each scan has been detected. Figure 6.17(b) illustrates the maximum current generated in the heterostructures in comparison with single layer Al_2O_3 film as a reference. An enhancement in the output signal is observed as the individual Ir layer thickness is increasing. The increase in current can be attributed to the field enhancement effect by the metallic contribution in the heterostructures. Additionally, simulations predict a connection between the maximum output signal and the metallic concentration. These results were submitted in our recent works [219,220]. These observations emphasize the potential enhancement of optically driven current generation in these atomically tailored metal-dielectric heterostructures.

6.5 Discussions

This chapter demonstrates a potential route to develop atomic scale metal-dielectric heterostructures of Ir/Al_2O_3 by employing the ALD technique. A combination of spectroscopic and microscopic methods has been implemented to thoroughly understand the interfacial properties. The XRR and HRTEM studies reveal the creation of layer by layer heterostructures in contrast to the formation of core-shell structures. Furthermore, the XPS analyses supported the formation of an Ir-O-Al environment for Angstrom scale Ir contributions. It is unique to observe the precisely controlled growth of atomically thin metallic Ir layer ($\approx$ 68% metallicity) starting from about 1 nm, enabled by the intrinsic atomic scale control of the ALD processes. A holistic and reliable set of characterizations has been developed to determine the thickness and dispersion behaviour of such heterostructures. Following this, the linear optical properties demonstrate the possibility of tailoring the optical constants by precise tuning of compositions. Additionally, manipulating the dielectric function enables to obtain epsilon-near-zero (ENZ) metamaterials based on metal-dielectric multilayer films. The precise composition control provided by the ALD technology can tailor the ENZ condition. The ENZ nature of the $Re(\epsilon)$ has evoked the potential of nonlinear optical applications. Furthermore, the SHG measurements indicate the feasibility of applying these metal-dielectric heterostructures for achieving higher output eficiency in SHG processes, as well as an improved laser induced damage threshold in comparison to the single layer metallic systems. Additionally, a brief overview is provided on the utility of such heterostructures in laser induced ultrafast current generation. These observations pave the path to artificially engineer novel optical materials for future applications in integrated optics, metamaterials, ultrafast optoelectronics, and tailored surfaces for enhanced optical nonlinearities. The fabrication technologies are CMOS compatible and will be of paramount importance in photonic integrated circuits.

Chapter 7

Summary and outlook

For the development of novel device concepts, CMOS compatibility, and 3D photonic integration, multilayer stacks of different materials with nanoscale thickness have become an integral part of this process chain. Atomic layer deposition (ALD) is one of the key technologies to enable the growth of such materials by pushing the edge of state of the art nanofabrication techniques to atomic scales. Due to the inherent self-limiting nature of the surface reactions, ALD provides promising 3D conformality as well as atomic control of the film composition.

This dissertation investigates the growth and properties of all-dielectric and metal-dielectric heterostructures where individual thicknesses have been achieved to be a few nanometers down to a few Angstroms. The conclusions based on the results of this research are summarized in the following.

A comprehensive study has been carried out to understand the growth, structural, chemical, and optical properties of hetero-interfaces formed between two technologically relevant oxides Al_2O_3 and TiO_2. The periodicity to form quantizing heterostructures while tuning the optical bandgap of TiO_2 has been evaluated here. Initially, plasma enhanced ALD (PEALD) processes of Al_2O_3 and TiO_2 were developed at 100°C to achieve uniform (2-3% non-uniformity across 200 mm), dense and optically homogeneous thin films. PEALD enables film growth at a lower temperature due to the required reaction energy being provided by the energetic radicals generated in the O_2 plasma. The single layer films possess very low optical losses down to 250 nm and 400 nm for Al_2O_3 and TiO_2, respectively. Al_2O_3

having the higher bandgap is applied to be the barrier material, whereas, the relatively low bandgap material TiO_2 is implemented as the quantum well material. Alternative stacking of these two materials having different optical bandgaps gives rise to the quantum well superlattice structures. In the heterostructures, the film thickness of Al_2O_3 and TiO_2 has been varied from ≈ 1 Å to 2 nm, respectively. The intermixing at interfaces, a modified bonding environment, and the formation of ternary oxides at interfaces become dominant structural features at this length scale. As the quantum well thickness is decreased to ≈ 0.5 nm or lower, a significant blue shift has been observed in the optical band-edge indicating towards the formation of optical quantizing structures. The technologically challenging length scale to attain quantizing effects in dielectrics has been targeted using the ALD processes due to the precise thickness and composition control of the constituents. Consequently, this enables the engineering of the optical bandgap and tailoring of the optical dispersion spectra by developing atomic scale heterostructures. Furthermore, thorough investigations have been devoted to systematically study the evolution of E_g as a function of n based on the composition ratio. The ultrathin quantizing nanolaminates of Al_2O_3/TiO_2, possessing higher E_g values, can also serve as potential candidates for optical coatings in high power laser applications. Overall, our rigorous investigations emphasize the flexibility of ALD to design novel ‘artificial’ optical materials of desired refractive indices and optical bandgap combinations with precise composition control at nanoscale. Following this, antireflection coatings for 355 nm have been designed and realized using two selected compositions. This demonstrates how the application window of TiO_2 coatings can be expanded to the UV spectral range by means of creating ALD heterostructures. Further, we extended our studies towards other important oxide interfaces, such as HfO_2/SiO_2 heterostructures. These structures indicate the flexibility of tailoring refractive indices, consequently, the optical bandgap and improve the laser induced damage threshold values making these heterostructures suitable for high power laser applications.

While investigating the metal-dielectric heterostructures, a unique combina-tion of Ir and Al_2O_3 has been introduced. Noble metal Ir is known for its versatile applications, for instance, barrier coatings, electrical contacts in microelectronics, and stable metallic mirrors, to list a few. Initially, single layer films of Ir and Al_2O_3 have been developed at 380°C by means of thermal ALD processes. In the heterostructures, the Ir thickness has been varied from ≈ 2 Å to 7.6 nm, whereas, the Al_2O_3 spacer thickness has been chosen to have 3.5 nm and 1.5 nm, respectively. Our previous studies on ALD Ir coatings on various substrates have demonstrated an island-type growth behaviour for ultrathin Ir coatings (e.g., below ≈ 5-6 nm). However, in the case of heterostructures with very low Ir content, a lay-ered structure has been observed in contrast to the expected core-shell structure, as revealed by the XRR and HRTEM analyses. Further XPS measurements led to the indication of interface mixing and formation of IrO_X at the interfaces where the individual Ir thickness was at sub-nanometer scale in the heterostructures. Upon increasing the Ir thickness to 1 nm, the change in bonding environment shows ≈ 68% metallic and 32% oxidic behaviour. It has remained challenging over the years to achieve such ultrathin transparent metallic layers. Several at-tempts have been made to grow ultrathin metal layers by PVD-based coating technologies. In this research, the well defined atomic layer by layer growth mode of the ALD technique has been exploited to obtain nearly a monolayer of metallic Ir coating, as supported by our STM observations. The reflection R and transmission T spectra and the dispersion properties of the Ir/Al_2O_3 heterostructures clearly validate a transition from effectively dielectric to metal as the individual Ir thickness became 2-4 nm. Additionally, the total stack thickness for all heterostructures has been determined by the SE, XRR, and SEM techniques. A reasonable agreement among them emphasizes that the ALD processes were well controlled and the superlattice nature was retained even with 102 times of repetition. The SE analyses were cross-validated by determining the T, R spectra from the fitted optical constants and comparing them with the measured values from spectrophotometry measurements. Furthermore, while calculating the dielectric constants, the $Re(\epsilon)$ of the [64:15]*25 composition demonstrated an epsilon near zero (ENZ) behaviour near 200-300 nm. This motivates future research in designing and fabricating ENZ materials with desired spectral performance using atomically controlled metal-dielectric heterostructures. Following this, the heterostructures exhibited the presence of second harmonic generation (SHG). The multilayer strategy has successfully achieved a higher second order nonlinearity as compared to single layer Ir and Al_2O_3 coatings. The inclusion of the dielectric Al_2O_3 spacers in the heterostructures has improved their laser induced damage threshold in comparison with pristine Ir coatings. These results demonstrate the potential of Ir-based heterostructures as an alternative nonlinear optical material at the nanoscale. Further analysis would be necessary to determine the $\chi^{(2)}$ parameters of such material systems.

Overall, ultrathin layers down to an Angstrom scale thickness in dielectric heterostructures and down to monolayer metallic films in metal-dielectric heterostructures have been successfully achieved. ALD allows us to leverage the precise thickness and composition of complex heterostructures down to atomic scale enabled by the atomic layer by layer growth mode towards manipulating the dispersion properties, optical bandgap, absorption and scattering losses, optical nonlinearity and laser induced damage threshold of heterostructure thin films. The potential of controlling the interface properties by implementing atomically thin barrier coatings could be explored further. Understanding the impact of the ultrathin interfaces in generating SHG and HHG would be the scope for future research direction. Nitride-based heterostructures (AlN, TiN, SiN) could be developed and incorporated for enhanced functionalities. The material basis of high-quality optical thin film coating processes could be further strengthened with the aim to grow non-centrosymmetric thin films and heterostructures with enhanced second-harmonic generation (SHG). Further, more complex optical systems can be developed, for instance, guided mode resonance grating elements with enhanced nonlinear optical properties by matching resonant waveguide conditions and active top-layer material nonlinearity. The investigations presented in this dissertation shall be helpful for future research activities in the above mentioned directions and beyond.

Zusammenfassung

In jeder Epoche der menschlichen Zivilisation zählt die Entdeckung neuer Materialien zu den größten Errungenschaften. Seit jeher öffnen sie die Tür zu neuen Technologien und machen diese zu einem integralen Bestandteil von Wachstum und Lebensqualität.

Mit der Miniaturisierung von Halbleiter-Bauelementen ist eine neue Generation von Materialien im Nanometer- und Ångströmbereich hervorgetreten. Solche ultradünnen Materialien können im Vergleich zu ihren Bulkmaterialien von Natur aus einzigartige Eigenschaften besitzen. Daher ist die Entwicklung neuartiger Materialien im Nanometermaßstab mit abstimmbaren Funktionalitäten von großem Interesse. Voraussetzung für die Erzeugung ultradünner Schichten und deren Heterostrukturen ist die Entwicklung und Umsetzung modernster Verfahren auf atomarer Ebene.

Die Atomlagenabscheidung (ALD) ist eine chemische Beschichtungstechnologie, die auf sequenziellen und selbstbegrenzenden chemischen Reaktionen von gasförmigen Reaktanten mit den verfügbaren funktionellen Gruppen auf der Substratoberfläche beruht. Aufgrund der selbstbegrenzten Oberflächenreaktionen und des zyklusbasierten Abscheidungsmechanismus ermöglicht die ALD eine präzise Kontrolle der Zusammensetzung bis in den atomaren Bereich sowie eine beeindruckende 3D-Konformität auf Strukturen mit hohem Aspektverhältnis. Dadurch eignet sich ALD besonders für die Herstellung ultradünner oder atomarer Heterostrukturen und bietet zudem die Flexibilität der Bauelementintegration. Ziel der Dissertation war die Untersuchung des Wachstums und Eigenschaften von sowohl dielektrischen als auch metall-dielektrischen Heterostrukturen auf atomarer Skala.

Im ersten Teil der Arbeit wurde eine umfassende Studie zum Verständnis des Wachstums, der strukturellen, chemischen und optischen Eigenschaften von dielektischen Hetero-Grenzflächen durchgeführt, welche sich zwischen den zwei technologisch relevanten Oxiden Al_2O_3 und TiO_2 ausbilden. Die alternativen Lagen von zwei Materialien mit unterschiedlichen optischen Bandlücken führt zur sogenannten Quantum-Well-Superlattice, einer Heterostruktur, bei der in dieser Arbeit Al_2O_3 als ein Material mit hoher Bandlücke als Barriere verwendet wird, und TiO_2 als ein Material mit relativ niedriger Bandlücke als 'Well'-material eingesetzt wird. Der technologisch anspruchsvolle kleine Maßstab zur Erzielung von Quantisierungseffekten in Dielektrika wurde mit Hilfe von ALD-Prozessen angestrebt, da hierdurch die Dicke und die Komposition der Bestandteile kontrolliert werden. Dies ermöglicht die Modifikation der optischen Bandlücke durch Anpassung des optischen Dispersionsprofils. In den Heterostrukturen wurden die Schichtdicken von Al_2O_3 und TiO_2 von ≈ 1 Å bis 2 nm variert. Die Vermischung an den Grenzflächen, die veränderte Bindungsumgebung und die Bildung von ternären Oxiden an den Grenzflächen führen zu dominanten Strukturmerkmalen auf dieser Größenskala. Bei einer Verringerung der TiO_2-Schichtdicke auf ca. 0,5 nm oder weniger wurde eine signifikante Blauverschiebung der Bandlücke beobachtet, welche auf die Bildung optischer Quantenstrukturen hinweist. Darüber hinaus wurden eine systematische Studie durchgeführt, um die Entwicklung von E_g als Funktion des Brechungsindex n auf der Grundlage des Zusammensetzungsverhältnisses zu analysieren. Die ultradünnen quantisierenden Nanolaminate aus Al_2O_3/TiO_2, die höhere E_g-Werte aufweisen, können auch als potenzielle Kandidaten für optische Beschichtungen in Hochleistungslaseranwendungen dienen. Auf Grundlage der gewonnenen Erkenntnisse wurden Antireflexionsbeschichtungen für die Laserwellenlänge 355 nm entwickelt und unter Verwendung von zwei ausgewählten Zusammensetzungen demonstriert. Es wurde erfolgreich gezeigt, dass der Anwendungsbereich von TiO_2-Schichten durch die Einbindung in Heterostrukturen bis in den UV-Spektralbereich erweitert werden kann. Schließlich erfolgte eine Ausweitung der Untersuchungen auf andere wichtige Oxidgrenzflächen, wie HfO_2/SiO_2-Heterostrukturen. Diese Strukturen bieten ebenso die Flexibilität, den Brechungsindex und die optische Bandlücke einzustellen. Die darüber hinaus ermittelten erhöhten Laserzerstörschwellen machen diese Heterostrukturen besonders attraktiv für Hochleistungslaseranwendungen.

Im zweiten Teil der Arbeit wurde bei der Untersuchung von metall-dielektrischen Heterostrukturen eine einzigartige Kombination von Iridium (Ir) und Al_2O_3 eingeführt. Das Edelmetall Ir ist für seine vielseitigen Anwendungen bekannt, z.B. für Barrierebeschichtungen, elektrische Kontakte in der Mikroelektronik, und stabile Metallspiegel. Zunächst wurden Einzelschichten aus Ir und Al_2O_3 bei 380°C mit thermischen ALD-Verfahren entwickelt. In den Heterostrukturen, wurde die Dicke des Ir von ≈ 2 Å bis 7,6 nm variert, während die Dicke des Al_2O_3-Abstandshalters (engl. spacer) auf 3,5 nm bzw. 1,5 nm festgelegt wurde. Die strukturellen und optischen Eigenschaften solcher Heterostrukturen wurden systematisch mit verschiedenen spektroskopischen und mikroskopischen Methoden untersucht. Frühere Studien zu ALD-Ir-Beschichtungen auf verschiedenen Substraten zeigten ein inselartiges (Volmer-Weber) Wachstumsverhalten für ultradünne Ir-Schichten (z.B. unter ≈ 5-6 nm). Im Gegensatz wurde Ir/Al_2O_3 Heterostrukturen jedoch eine Schichtstruktur beobachtet, wie die XRR- und HRTEM-Analysen bestätigen. Weitere XPS-Messungen ergaben den Hinweis auf eine Grenzflächenmischung und die Bildung von IrO_X an den Grenzflächen, wodurch die individuelle Ir-Schichtdicke in den Heterostrukturen im Subnanometerbereich lag. Nach Erhöhung der Ir-Dicke auf 1 nm zeigt die Veränderung der Bindungsumgebung ≈ 68% metallisches und 32% oxidisches Verhalten. In der vorliegenden Arbeit wurde das deutlich definierte Schicht-für-Schicht-Wachstum der ALD-Technologie genutzt, und letztlich eine einlagige metallische Ir-Beschichtung erzeugt, was durch STM-Bilder gezeigt wurde. Die Reflexions- und Transmissionsspektren R und T sowie die Dispersionsspektren der Ir/Al_2O_3-Heterostrukturen bestätigen eindeutig einen Übergang vom effektiven Dielektrika zum Metall, wenn die individuelle Ir-Schichtdicke 2-4 nm erreicht. Zusätzlich wurde die Gesamtdicke des Schichtstapels (engl. stack) für alle Heterostrukturen mit Hilfe der SE, XRR- und SEM-Techniken bestimmt. Die gute Übereinstimmung zwischen den Verfahren unterstreicht, dass die ALD-Prozesse gut kontrolliert wurden und der

Übergittercharakter erhalten blieb, auch bei 102 Wiederholungen der Heterostruktur. Die Stimmung der dielektrischen Konstanten, Re(ϵ) der [64:15]*25-Zusammensetzung zeigt ein 'Epsilon Near Zero' (ENZ) Verhalten bei 200-300 nm auf. Dies motiviert die zukünftige Forschung zur Entwicklung und Herstellung von ENZ-Materialien mit der gewünschten spektralen Leistung. Darüber hinaus zeigten die Heterostrukturen eine optische Frequenzverdopplung der Grund-welle des Laserlichts (engl. second-harmonic generation; SHG). Die Mehrschichtstrategie hat erfolgreich eine höhere Nichtlinearität zweiter Ordnung im Vergleich zu einlagigen Ir- und Al_2O_3-Beschichtungen aufgezeigt. Die Einbeziehung der dielektrischen Al_2O_3-Abstands-halter in die Heterostrukturen erhöhen zudem die Laserzerstörschwellen im Vergleich zu einzel Ir-Schichten. Diese Ergebnisse zeigen das Potenzial von Ir-basierten Zusammensetzungen als alternatives nichtlineares optisches Material auf der Nano-skala. Zur Bestimmung von $\chi^{(2)}$ solcher Materialsysteme sind weitere Analysen geplant, die jedoch nicht Gegenstand der vorliegenden Arbeit sind.

Zusammengefasst wurden ultradünne Schichten bis zu einer Schichtdicke im Ängström-Bereich in dielektrischen Heterostrukturen und bis hin zu einlagigen metallischen Schichten erfolgreich realisiert. Atomlagenabscheidung ermöglicht es hierbei, die Dicke und Zusammensetzung der komplexen Heterostrukturen bis hinunter auf die atomare Skala genau zu beherrschen, und somit auch Dispersionseigenschaften, optische Bandlücken, Absorptions- und Streuverluste, optische Nichtlinearität und Laserzerstörschwellen der erzeugten Heterostruktur-Dünnschichten zu verbessern. Die rigorosen Untersuchungen dieser Arbeit unterstreichen die Flexibilität der ALD-Methode zur Herstellung neuartiger 'künstlicher' optischer Materialien mit gewünschten Funktionalitäten durch die maßgeschneiderte Zusammensetzung im Nanomaßstab und diesen als Grundlage für die Entwicklung von inovativen optische Systemen.

Bibliography

[1] M. Fox, Optical properties of solids, Oxford University Press, 2010.

[2] T. Edvinsson, Optical quantum confinement and photocatalytic properties in two-, one- and zero-dimensional nanostructures, Royal society open science 5(9) (2018).

[3] M. Mende, S. Schrameyer, H. Ehlers, D. Ristau, L. Gallais, Laser damage resistance of ion-beam sputtered Sc_2O_3/SiO_2 mixture optical coatings, Appl. Opt. 52, 1368-1376 (2013).

[4] C. Franke, O. Stenzel, S. Wilbrandt, N. Kaiser, A. Tünnermann, Preparation and characterization of aluminum oxide/aluminum fluoride mixture coatings for applications in the deep ultraviolet spectral range, Proc. SPIE 9627, 96271N (2015).

[5] S. Yoshida, S. Misawa, S. Gonda, Epitaxial growth of GaN/AlN heterostructures, Journal of Vacuum Science Technology B: Microelectronics Processing and Phenomena 1, 250 (1983).

[6] K. Yasuda, Emergent Transport Properties of Magnetic Topological Insulator Heterostructures, Springer Theses, 2020.

[7] J. Liu, T. Hesjedal, Magnetic topological insulator heterostructures: A review, Adv. Mater. 2102427 (2021).

[8] M. Mogi, Quantized Phenomena of Transport and Magneto-Optics in Magnetic Topological Insulator Heterostructures, Springer, 2022.

[9] J. P. V. der Ziel, R. Dingle, R. C. Miller, W. Wiegmann, W. A. N. Jr., Laser oscillation from quantum well states in very thin GaAsAl$_{0.2}$Ga$_{0.8}$As multilayered structures, Appl. Phys. Lett. 26, 463-465 (1975).

[10] W. V. McLevige, H. T. Yuan, W. M. Duncan, W. R. Frensley, F. H. Doerbeck, H. Morkoc, T. J. Drummond, GaAs/AlGaAs heterojunction bipolar transistors for integrated circuit applications, IEEE Electron Device Letters 3, 2 (1982).

[11] S. Nakamura, M. Senoh, S. Nagahama, N. Iwasa, T. Yamada, T. Matsushita, H. Kiyoku, Y. Sugimoto, InGaN-based multiquantum-well-structure laser diodes, Jpn. J. Appl. Phys. 55, 2 (1996).

[12] D. S. Ghosh, T. L. Chen, V. Pruneri, Ultrathin Cu-Ti bilayer transparent conductors with enhanced figure-of-merit and stability, Appl. Phys. Lett. 96, 091106 (2010).

[13] D. S. Ghosh, R. Betancur, T. L. Chen, V. Pruneri, J. Martorell, Semi-transparent metal electrode of Cu–Ni as a replacement of an ITO in organic photovoltaic cells, Sol. Energy Mat. Sol. Cells 95, 4, 1228-1231 (2011).

[14] N. Formica, D. S. Ghosh, T. L. Chen, V. Pruneri, Highly stable ultrathin Ag-Ni films for flexible transparent electronics, ECS - The Electrochemical Society, Meet. Abstr., MA2012-01 820 (2012).

[15] M. Herzog, A. von Reppert, J. E. Pudell, C. Henkel, M. Kronseder, C. H. Back, A. A. Maznev, M. Bargheer, Phonon-dominated energy transport in purely metallic heterostructures, Adv. Funct. Mater. 31, 27, 2101086 (2021).

[16] E. Pomerantseva, Y. Gogotsi, Two-dimensional heterostructures for energy storage, Nat Energy 2, 17089 (2017).

[17] E. Najafidehaghani, Z. Gan, A. George, T. Lehnert, G. Q. Ngo, C. Neumann, T. Bucher, I. Staude, D. Kaiser, T. Vogl, U. Hübner, U. Kaiser, F. Eilenberger, A. Turchanin, 1D p–n junction electronic and optoelectronic devices from transition metal dichalcogenide lateral heterostructures grown

by one-pot chemical vapor deposition synthesis, Adv. Funct. Mater. 31, 27, 2101086 (2021).

[18] Z. Gan, E. Najafidehaghani, S. H. Han, S. Shradha, F. Abtahi, C. Neumann, J. Picker, T. Vogl, U. Hübner, F. Eilenberger, A. George, A. Turchanin, Patterned growth of transition metal dichalcogenide monolayers and multilayers for electronic and optoelectronic device applications, Small Methods 6, 2200300 (2022).

[19] Z. Gan, I. Paradisanos, A. E. Real, J. Picker, E. Najafidehaghani, F. Davies, C. Neumann, C. Robert, P. Wiecha, K. Watanabe, T. Taniguchi, X. Marie, J. Biskupek, M. Mundszinger, R. Leiter, U. Kaiser, A. V. Krasheninnikov, B. Urbaszek, A. George, A. Turchanin, Chemical vapor deposition of high-optical-quality large-area monolayer janus transition metal dichalcogenides, Adv. Mater. 34, 38, 2270270 (2022).

[20] J. Li, X. Bi, Quantum confinement induced ultra-high intensity interfacial radiative recombination in nanolaminates, Nanoscale 9, 16420-16428 (2017).

[21] A. Cho, J. Arthur, Molecular beam epitaxy, Progress in Solid State Chemistry 10(3), 157-191 (1995).

[22] L. Chang, K. Ploog, Molecular Beam Epitaxy and Heterostructures, Martinus Nijhoff Publishers, 1985.

[23] R. Farrow, Molecular Beam Epitaxy: Applications to Key Materials, Noyes Publications, 1995.

[24] B. Joyce, Molecular beam epitaxy, Rep. Prog. Phys. 48, 1637 (1985).

[25] W. P. McCray, MBE deserves a place in the history books, Nature Nanotechnology volume 2, pages259–261 (2007) 2, 259-261 (2007).

[26] X. Chen, X. Ma, K. He, J. Jia, Q. Xue, Molecular beam epitaxial growth of topological insulators, Adv. Mater. 23, 1162–1165 (2011).

[27] L. He, X. Kou, K. Wang, Review of 3D topological insulator thin-film growth by molecular beam epitaxy and potential applications, Phys. Status Solidi RRL (2013) 7, No. 1–2, 50–63 (2013).

[28] Y. Illarionov, A. Banshchikov, D. Polyushkin, S. Wachter, T. Knobloch, M. Thesberg, L. Mennel, M. Paur, M. Stöger-Pollach, M. V. A. Steiger-Thirsfeld, M. Waltl, N. S. Sokolov, T. Mueller, T. Grasser, Ultrathin calcium fluoride insulators for two-dimensional field-effect transistors, Nat. Electron. 2, 230-235 (2019).

[29] S. M. George, Atomic layer deposition: An overview, Chem. Rev. 110, 1, 111–131 (2010).

[30] A. Khanna, A. Z. Subramanian, M. Häyrinen, S. Selvaraja, P. Verheyen, D. V. Thourhout, S. Honkanen, H. Lipsanen, R. Baets, Impact of ALD grown passivation layers on silicon nitride based integrated optic devices for very-near-infrared wavelengths, Opt. Express 22, 5684-5692 (2014).

[31] G. Moille, S. Combrié, L. Morgenroth, G. Lehoucq, F. Neuilly, B. Hu, D. Decoster, A. de Rossi, Integrated all-optical switch with 10 ps time resolution enabled by ALD, Laser & Photonics Reviews 10, 3, 409 - 419 (2016).

[32] G. N. West, Seeing blue: pushing integrated photonics into the ultraviolet with ALD aluminum oxide, Proc. SPIE 11283, Integrated Optics: Devices, Materials, and Technologies XXIV, 112830B (2020).

[33] W. A. P. M. Hendriks, L. Chang, C. I. van Emmerik, J. Mu, M. de Goede, M. Dijkstra, S. M. Garcia-Blanco, Rare-earth ion doped Al_2O_3 for active integrated photonics, Advances in Physics: X, 6:1 (2021).

[34] H. Kim, Atomic layer deposition of metal and nitride thin films: Current research efforts and applications for semiconductor device processing, J. Vac. Sci. Technol. B: Microelectronics and Nanometer Structures Processing, Measurement, and Phenomena 21, 2231–2261 (2003).

[35] C. S. Huang, Atomic Layer Deposition for Semiconductors, Springer, 2014.

[36] T. Hirvikorpi, M. Vähä-Nissi, J. J. Nikkola, A. Harlin, M. Karppinen, Thin Al_2O_3 barrier coatings onto temperature-sensitive packaging materials by atomic layer deposition, Surf. Coat. Technol. 205, 50885092 (2011).

[37] C. Barbos, D. Blanc-Pelissier, A. Fave, C. Botella, P. Regreny, G. Grenet, E. Blanquet, A. Crisci, M. Lemiti, Al_2O_3 thin films deposited by thermal atomic layer deposition: Characterization for photovoltaic applications, Thin Solid Films 8(9):4726-9 (2008).

[38] H. Patel, C. Reichel, A. Richter, P. Masuch, J. Benick, S. Glunz, Effective charge dynamics in Al_2O_3/SiO_2 multilayer stacks and their influence on silicon surface passivation, Appl. Surf. Sci. 579, 152175 (2022).

[39] K. B. Jinesh, J. L. van Hemmen, M. C. M. van de Sanden, F. Roozeboom, J. H. Klootwijk, W. F. A. Besling, W. M. M. Kessels, Dielectric properties of thermal and plasma-assisted atomic layer deposited Al_2O_3 thin films, J. Electrochem. Soc. 158 (2), G21 (2011).

[40] M. Tapajna, L. Valik, F. Gucmann, D. Gregusova, K. Frohlich, S. Has-cik, E. Dobrocka, L. Toth, B. Pecz, J. Kuzmik, Low-temperature atomic layer deposition-grown Al_2O_3 gate dielectric for GaN/AlGaN/GaN MOS HEMTs: Impact of deposition conditions on interface state density, J. Vac. Sci. Technol. B: Nanotechnol. and Microelectron. 35 (1), 01A107 (2017).

[41] A. Szeghalmi, M. Helgert, R. Brunner, F. Heyroth, U. Gösele, M. Knez, Atomic layer deposition of Al_2O_3 and TiO_2 multilayers for applications as bandpass filters and antireflection coatings, Appl. Opt. 48, 1727-1732 (2009).

[42] A. Szeghalmi, M. Helgert, R. Brunner, F. Heyroth, U. Gösele, M. Knez, Tunable guided-mode resonance grating filter, Adv. Funct. Mater. 20, 2053-2062 (2010).

[43] V. Beladiya, T. Faraz, P. Schmitt, A.-S. Munser, S. Schröder, S. Riese, C. Mühlig, D. Schachtler, F. Steger, R. Botha, F. Otto, T. Fritz, C. van Helvoirt, W. M. M. Kessels, H. Gargouri, A. Szeghalmi, Plasma-enhanced

atomic layer deposition of HfO_2 with substrate biasing: Thin films for high-reflective mirrors, ACS Appl. Mater. Interfaces 2022 14, 12, 14677–14692 (2022).

[44] R. L. Puurunen, Surface chemistry of atomic layer deposition: A case study for the trimethylaluminum/water process, J. Appl. Phys. 97, 121301 (2005).

[45] H. B. Profijt, S. E. Potts, M. C. M. van de Sanden, W. M. M. Kessels, Plasma-assisted atomic layer deposition: Basics, opportunities, and challenges, J. Vac. Sci. Technol. A 29, 050801 (2011).

[46] H. C. M. Knoops, T. Faraz, K. Arts, W. M. M. Kessels, Status and prospects of plasma-assisted atomic layer deposition, J. Vac. Sci. Technol. A 37, 030902 (2019).

[47] L. Kim, Y. J. Jeong, T. K. An, S. Park, J. H. Jang, S. Nam, J. Jang, S. Kim, C. Park, Optimization of Al_2O_3/TiO_2 nanolaminate thin films prepared with different oxide ratios, for use in organic light-emitting diode encapsulation, via plasma-enhanced atomic layer deposition, Phys. Chem. Chem. Phys. 18, 1042-1049 (2016).

[48] L. Kim, K. Kim, S. Park, Y. Jeong, H. Kim, D. Chung, S. Kim, C. Park, Al_2O_3/TiO_2 nanolaminate thin film encapsulation for organic thin film transistors via plasma-enhanced atomic layer deposition, ACS Appl. Mater. Interfaces 6, 9, 6731–6738 (2014).

[49] I. Dirnstorfer, T. Chohan, P. Jordan, M. Knaut, D. Simon, J. Bartha, T. Mikolajick, Al_2O_3-TiO_2 nanolaminates for conductive silicon surface passivation, IEEE J. Photovolt. 6, 86-91 (2016).

[50] I. Iatsunskyi, E. Coy, R. Viter, G. Nowaczyk, M. Jancelewicz, I. Baleviciute, K. Zaleski, S. Jurga, Study on structural, mechanical, and optical properties of Al_2O_3-TiO_2 nanolaminates prepared by atomic layer deposition, J. Phys. Chem. C 119, 20591-20599 (2015).

[51] O. Yilvaara, L. Kilpi, X. Liu, S. Sintonen, S. Ali, M. Laitinen, J. Julin, E. Haimi, T. Sajavaara, S. H. H. Lipsanen, H. Ronkainen, R. Puurunen, Aluminum oxide/titanium dioxide nanolaminates grown by atomic layer deposition: Growth and mechanical properties, J. Vac. Sci. Technol. A 35, 01B105 (2017).

[52] L. Ghazaryan, S. Handa, P. Schmitt, V. Beladiya, V. Roddatis, A. Tünnermann, A. Szeghalmi, Structural, optical, and mechanical properties of TiO_2 nanolaminates, Nanotechnology 32, 95709 (2021).

[53] T. Willemsen, M. Jupé, L. Gallais, D. Tetzlaff, D. Ristau, Tunable optical properties of amorphous tantala layers in a quantizing structure, Opt. Lett. 42, 4502-4505 (2017).

[54] M. Steinecke, H. Badorreck, M. Jupé, T. Willemsen, L. Hao, L. Jensen, D. Ristau, Quantizing nanolaminates as versatile materials for optical interference coatings, Appl. Opt. 59, A236–A241 (2020).

[55] D. S. Ghosh, Ultrathin Metal Transparent Electrodes for the Optoelectronics Industry, Springer Theses, 2013.

[56] N. Formica, D. Ghosh, A. Carrilero, T. Chen, R. Simpson, V. Pruneri, Ultrastable and atomically smooth ultrathin silver films grown on a copper seed layer, ACS Appl. Mater. Interfaces 5, 8, 3048-3053 (2013).

[57] R. Maniyara, D. Rodrigo, J. C.-F. R. Yu, D. Ghosh, R. Yongsunthon, D. Baker, A. Rezikyan, F. Abajo, V. Pruneri, Tunable plasmons in ultrathin metal films, Nat. Photonics 13, 328–333 (2019) 13, 328-333 (2019).

[58] D. Lehr, J. Reinhold, I. Thiele, H. Hartung, K. Dietrich, C. Menzel, T. Pertsch, E. Kley, A. Tünnermann, Enhancing second harmonic generation in gold nanoring resonators filled with lithium niobate, Nano Lett. 15(2), 1025-1030 (2015).

[59] S. Stempfhuber, N. Felde, S. Schwinde, M. Trost, P. Schenk, S. Schröder, A. Tünnermann, Influence of seed layers on optical properties of aluminum in the UV range, Opt. Express 28, 20324-20333 (2020).

[60] P. Schmitt, S. Stempfhuber, N. Felde, A. Szeghalmi, N. Kaiser, A. Tünnermann, S. Schwinde, Influence of seed layers on the reflectance of sputtered aluminum thin films, Opt. Express 29, 19472-19485 (2021).

[61] P. Schmitt, V. Beladiya, N. Felde, P. Paul, F. Otto, T. Fritz, A. Tünnermann, A. Szeghalmi, Influence of substrate materials on nucleation and properties of iridium thin films grown by ALD, Coatings 11(2), 173 (2021).

[62] P. Schmitt, N. Felde, T. Döhring, M. Stollenwerk, I. Uschmann, K. Hanemann, M. Siegler, G. Klemm, N. Gratzke, A. Tünnermann, S. Schwinde, S. Schröder, A. Szeghalmi, Influence of substrate materials on nucleation and properties of iridium thin films grown by ALD, Optical Materials Express 12 (2), 545-559 (2022).

[63] D. Wei, Y. Tan, Y. Wang, T. kong, S. Shen, S. Mao, Function-switchable metal/semiconductor junction enables eficient photocatalytic overall water splitting with selective water oxidation products, Science Bulletin 65, 6, 1389-1395 (2020).

[64] I. Razdolski, A. Chekhov, A. Stognij, A. Stupakiewicz, Ultrafast transport and relaxation of hot plasmonic electrons in metal-dielectric heterostructures, Phys. Rev. B 100, 45412 (2019).

[65] V. Lucarini, J. Saarinen, K. E. Peiponen, E. Vartiainen, Kramers-Kronig Relations in Optical Materials Research, Springer, 2005.

[66] L. Macros, J. Larruquert, Analytic optical-constant model derived from Tauc-Lorentz and urbach tail, Opt. Express 24, 28561-28572 (2016).

[67] M. Di, E. Bersch, A. Diebold, Comparison of methods to determine bandgaps of ultrathin HfO_2 films using spectroscopic ellipsometry, J. Vac. Sci. Technol. A 29, 041001 (2011).

[68] F. Urbach, The long-wavelength edge of photographic sensitivity and of the electronic absorption of solids, Phys. Rev. 92, 1324 (1953).

[69] H. Shahrokhabadi, A. Bananej, M. Vaezzadeh, Investigation of cody–lorentz and tauc–lorentz models in characterizing dielectric function of $(HfO_2)_x(ZrO_2)_{1-x}$ mixed thin film, Journal of Applied Spectroscopy 84, 915-922 (2017).

[70] P. Drude, Zur Elektronentheorie der metalle. Annalen der Physik, Annalen der Physik 306 (3), 566 (1900).

[71] N. V. Smith, Classical generalization of the Drude formula for the optical conductivity, Phys. Rev. B 64, 155106 (2001).

[72] P. D. Sia, Overview of Drude-Lorentz type models and their applications, Nanoscale Syst.: Math. Model. Theory Appl. 2014; 3, 1–13 (2014).

[73] O. Stenzel, Optical coatings: Material Aspects in theory and Practice, Springer Science Business, 2004.

[74] H. Tompkins, E. A. Irene, Handbook of ellipsometry, William Andrew, 2005.

[75] A. Moradi, Maxwell-Garnett effective medium theory: Quantum nonlocal effects, Phys. Plasmas. 22, 42105 (2015).

[76] V. A. Markel, Introduction to the Maxwell Garnett approximation: tutorial, JOSA A 33, 1244–1256 (2016).

[77] D. A. G. Bruggeman, Berechnung verschiedener physikalischer Konstanten von heterogenen Substanzen. I. Dielektrizitätskonstanten und Leitfähigkeiten der Mischkörper aus isotropen Substanzen, Annalen der Physik 416(7), 636–664 (1935).

[78] D. Aspnes, Local-field effects and effective-medium theory: A microscopic perspective, Am. J. Phys. 50(8) (1982).

[79] L. I. Schiff, Quantum Mechanics, McGraw-Hill, 1995.

[80] O. Stenzel, The physics of thin film optical spectra: An introduction, Springer, 2007.

[81] M. Born, E. Wolf, Principles of optics: electromagnetic theory of propagation, interference and diffraction of light, Elsevier, 1999.

[82] N. Kaiser, Old rules useful to the designer of optical coatings, VIP Vacuum's Best, Wiley Online Library 20, S1, 7-14 (2008).

[83] Y. R. Shen, The principles of nonlinear optics, John Wiley Sons, 1998.

[84] R. W. Boyd, Nonlinear Optics, Academic Press, 2008.

[85] G. New, Introduction to Nonlinear Optics, Chambridge University Press, 2011.

[86] V. G. Dmitriev, G. G. Gurzadyan, D. N. Nikogosyan, Handbook of Nonlinear Optical Crystals, Springer, 1999.

[87] D. N. Nikogosyan, Nonlinear Optical Crystals: A Complete Survey, Springer, 2005.

[88] J. Wen, F. Geng, F. Wang, J. Huang, X. Jiang, Q. Deng, L. Cao, Nonlinear optical and laser damage properties of KDP crystal with trace impurities in bulk, Cryst. Res. Technol. 53, 7 (2018).

[89] R. A. Ganeev, I. A. Kulagin, A. I. Ryasnyanski, R. I. Tugushev, T. Usmanov, Characterization of nonlinear optical parameters of KDP, $LiNbO_3$ and BBO crystals, Opt. Comm. 229, 1-6 (2004).

[90] Z. S. Shanon, R. S. Alnayli, K. J. Tahir, Study of the nonlinear optical properties of lithium triborate crystal by using z-scan technique, Int. J. Sci. Res. 5, 8 (2016).

[91] L. Zhang, A. M. Agarwal, L. C. Kimerling, J. Michel, Nonlinear group IV photonics based on silicon and germanium: from near-infrared to mid-infrared, Nanophotonics 3, 4-5 (2013).

[92] G. Safarpour, M. Novzari, M. A. Izadi, S. Yazdanpanahi, The linear and nonlinear optical properties of GaAs/GaAlAs nanowire superlattices, Superlattices Microstruct. 75, 725-738 (2014).

[93] L. Karvonen, A. Säynätjoki, Y. Chen, H. Jussila, J. Rönn, M. Ruoho, T. Alasaarela, S. Kujala, R. A. Norwood, N. Peyghambarian, K. Kieu, S. Honkanen, Enhancement of the third-order optical nonlinearity in ZnO/Al_2O_3 nanolaminates fabricated by atomic layer deposition, Appl. Phys. Lett. 103, 31903 (2013).

[94] L. Alloatti, C. Kieninger, A. Froelich, M. Lauermann, T. Frenzel, K. Köhnle, W. Freude, J. Leuthold, M. Wegener, C. Koos, Second-order nonlinear optical metamaterials: ABC-type nanolaminates, Appl. Phys. Lett. 107, 121903 (2015).

[95] S. Clemmen, A. Hermans, E. Solano, J. Dendooven, K. Koskinen, M. Kauranen, E. Brainis, C. De-tavernier, R. Baets, Atomic layer deposited second-order nonlinear optical metamaterial for back-end integration with CMOS-compatible nanophotonic circuitry, Opt. Lett. 40, 5371–5374 (2015).

[96] A. Wickberg, C. Kieninger, C. Sürgers, S. Schlabach, X. Mu, C. Koos, M. Wegener, Second-harmonic generation from Zno/Al_2O_3 nanolaminate optical metamaterials grown by atomic-layer deposition, Adv. Opt. Mater. 4(8) (2016).

[97] F. Abtahi, P. Paul, S. Beer, A. Kuppadakkath, A. Pakhomov, A. Szeghalmi, S. Nolte, F. Setzpfandt, F. Eilenberger, Enhanced surface second harmonic generation in nanolaminates, Opt. Express 31, 11354-11362 (2023).

[98] S. Suresh, O. Reshef, M. Alam, J. Upham, M. Karimi, R. Boyd, Enhanced nonlinear optical responses of layered epsilon-near-zero metamaterials at visible frequencies, ACS Photonics 8 (1), 125–129 (2021).

[99] I. Liberal, N. Engheta, Near-zero refractive index photonics, Nat. Photonics 11 (3), 149–158 (2017).

[100] F. J. F. Löchner, A. George, K. Koshelev, T. Bucher, E. Najafidehaghani, A. Fedotova, D.-Y. Choi, T. Pertsch, I. Staude, Y. Kivshar, A. Turchanin, F. Setzpfandt, Hybrid dielectric metasurfaces for enhancing second-harmonic generation in chemical vapor deposition grown MoS_2 monolayers, ACS Photonics 8, 1, 218–227 (2021).

[101] A. Kuppadakkath, A. George, A. Tuniz, G. Q. Ngo, H. Knopf, F. Löchner, F. Abtahi, T. Bucher, M. Steinert, S. Shradha, E. Najafidehaghani, T. Käsebier, A. Gottwald, N. Felde, P. Paul, T. Ullsperger, S. Schröder, A. Szeghalmi, T. Pertsch, I. Staude, T. Vogl, U. Zeitner, A. Turchanin, F. Eilenberger., Direct growth of monolayer MoS_2 on nanostructured silicon waveguides, Nanophotonics 0235 (2022).

[102] A. Fedotova, M. Younesi, J. Sautter, A. Vaskin, F. J. F. Löchner, M. Steinert, R. Geiss, T. Pertsch, I. Staude, F. Setzpfandt, Second-harmonic generation in resonant nonlinear metasurfaces based on lithium niobate, Nano Lett. 20, 12, 8608–8614 (2020).

[103] A. Fedotova, M. Younesi, M. Weissflog, D. Arslan, T. Pertsch, I. Staude, F. Setzpfandt, Spatially engineered nonlinearity in resonant metasurfaces, Photon. Res. 11, 252-259 (2023).

[104] A. Wickberg, A. Abass, H.-H. Hsiao, C. Rockstuhl, M. Wegener, Second-harmonic generation by 3D laminate metacrystals, Adv. Opt. Mater. 7, 1801235 (2019).

[105] V. Aleskovskii, S. Kol'tsov, Some characteristics of molecular layering reactions, Abstract of Scientific and Technical Conference, Goskhimizdat, Leningrad p. 67 (1965).

[106] R. Puurunen, A short history of atomic layer deposition: Tuomo suntola's atomic layer exitaxy, Chem. Vap. Dep. 20, 332-344 (2014).

[107] T. Suntola, J. Antson, Method for producing compound thin films, Patent. FIN 52359 US 4 058 430 (29.11.1974).

[108] M. Mattinen, G. Popov, M. Vehkamäki, P. J. King, K. Mizohata, P. Jalkanen, J. Räisänen, M. Leskelä, M. Ritala, Atomic layer deposition of emerging 2D semiconductors, HfS_2 and ZrS_2, for optoelectronics, Chem. Mater. 31, 15, 5713–5724 (2019).

[109] L. Tadmor, E. Brusaterra, E. B. Treidel, F. Brunner, N. Bickel, S. S. T. Vandenbroucke, C. Detavernier, J. Würfl, O. Hilt, Effects of post metallization annealing on Al_2O_3 atomic layer deposition on n-GaN, Semicond. Sci. Technol 38, 015006 (2023).

[110] E. Schiliro, R. L. Nigro, S. E. S. E. Panasci, S. Agnello, M. Cannas, F. M. Gelardi, F. Roccaforte, F. Giannazzo, Direct atomic layer deposition of ultrathin aluminum oxide on monolayer MoS_2 exfoliated on gold: The role of the substrate, Adv. Mater. Interfaces 8 (21), 2101117 (2021).

[111] E. Schiliro, P. Fiorenza, G. Greco, F. Monforte, G. G. Condorelli, F. Roccaforte, F. Giannazzo, R. L. Nigro, Early growth stages of aluminum oxide (Al_2O_3) insulating layers by thermal- and plasma-enhanced atomic layer deposition on AlGaN/GaN heterostructures, ACS Appl. Electron. Mater. 4 (1), 406415 (2022).

[112] X. Meng, X. Wang, D. Geng, C. Ozgit-Akgun, N. Schneider, J. W. Elam, Atomic layer deposition for nanomaterial synthesis and functionalization in energy technology, Mater. Horiz. 4, 133-154 (2017).

[113] N. Schneider, L. Duclaux, M. Bouttemy, C. Bugot, F. Donsanti, A. Etcheberry, N. Naghavim, Transparent ohmic contact for CIGS solar cells based on p-type aluminum copper sulfide material synthesized by atomic layer deposition, ACS Appl. Energy Mater. 1, 12, 7220–7229 (2018).

[114] H. L. Tulzo, N. Schneider, D. Lincot, F. Donsanti, Toward an all-atomic layer deposition (ALD) process for Cu(In,Ga)(S,Se)$_2$ (CIGS)-type solar cell, Sol. Energy Mater Sol. Cells 200, 109965 (2019).

[115] A. Richter, H. Patel, C. Reichel, J. Benick, S. Glunz, Improved silicon surface passivation by ald Al_2O_3/SiO_2 multilayers with in-situ plasma treatments, Adv. Mater. Interfaces 2202469 (2023).

[116] K. Gerold, V. Beladiya, P. Paul, D. Kästner, M. Saarniheimo, K. Niiranen, S. Schröder, A. Szeghalmi, Conformal antireflection coatings for optical dome covers by atomic layer deposition, Appl. Opt. 62, B92-B96 (2023).

[117] Optical coatings: Conformal thin films for curved and freeform optics. available online: accessed on 23 May (2023).
URL https://beneq.com/en/markets/optical-coatings/

[118] V. Cremers, R. L. Puurunen, J. Dendooven, Conformality in atomic layer deposition: Current status overview of analysis and modelling, Appl. Phys. Rev. 6, 021302 (2019).

[119] K. Arts, M. Utriainen, R. L. Puurunen, W. M. M. Kessels, H. C. M. Knoops, Film conformality and extracted recombination probabilities of o atoms during plasma-assisted atomic layer deposition of SiO_2, TiO_2, Al_2O_3, and HfO_2, J. Phys. Chem. C 123, 44, 27030–27035 (2019).

[120] K. Pfeiffer, U. Schulz, A. Tünnermann, A. Szeghalmi, Antireflection coatings on curved substrates, Coatings 7(8), 118 (2017).

[121] P.Paul, V. Beladiya, D. Kästner, U. Schulz, M. Burkhardt, A. Szeghalmi, Conformal antireflection coating on polycarbonate domes, Proc. SPIE 11872, Advances in Optical Thin Films VII, 118720E (2021).

[122] M. Bosund, E. Salmi, R. Peltonen, Atomic layer deposition into ultra-high aspect ratio structures with a stop-flow ald reactor. available under: https://beneq.com/en/thin-films/research-world/science-letters/atomic-layer-deposition-ultra-high-aspect-ratio-structures-stop-flow-ald (21.11.2022).

[123] M. Kariniemi, J. Niinistö, M. Vehkamäki, M. Kemell, M. Ritala, M. Leskelä, Conformality of remote plasma-enhanced atomic layer deposition processes: An experimental study, J. Vac. Sci. Technol. A 30, 01A115 (2012).

[124] M. Ritala, Z. Niinistö, Chemical Vapour Deposition: Precursors, Processes and Applications, Chapter 4: Atomic Layer Deposition, RSC Publishing, 2008.

[125] P. Genevée, E. Ahiavi, N. Janunts, T. Pertsch, M. Oliva, E.-B. Kley, A. Szeghalmi, Blistering during the atomic layer deposition of iridium, J. Vac. Sci. Technol. A 34, 01A113 (2016).

[126] H. G. Tompkins, E. Irene, Handbook of Ellipsometry, William Andrew, Inc., 2005.

[127] H. G. Tompkins, J. N. Hilfiker, Spectroscopic Ellipsometry, Momentum Press, 2016.

[128] H. Fujiwara, Spectroscopic Ellipsometry: Principles and Applications, John Wiley & Sons, Ltd, 2007.

[129] A. Cauchy, Sur la réfraction et la réflexion de la lumière, Bull. des sc. Math. 14, 6-10 (1830).

[130] J. A. Woollam, "What is Ellipsometry?" (2022).
URL https://www.jawoollam.com/resources/ellipsometry-tutorial/what-is-ellipsometry

[131] A. Ferlauto, G. Ferreira, J. Pearce, C. Wronski, R. Collinsa, Analytical model for the optical functions of amorphous semiconductors from the near-

infrared to ultraviolet: Applications in thin film photovoltaics, J. Appl. Phys. 92(5) (2002).

[132] U. Richter, G. Dittmar, H. Ketelsen, SpectraRay Software Manual, SENTECH Instruments GmbH, 2017.

[133] Fraunhofer IOF internal.

[134] O. Stenzel, S. Wilbrandt, K. Friedrich, N. Kaiser, Realistische Modellierung der NIR/VIS/UV optischen Konstanten dünner optischer Schichten im Rahmen des Oszillatormodells, Vakuum in Forschung und Praxis 21, 15–23 (2009).

[135] G. Stoney, The tension of metallic films deposited by electrolysis, Proc. R. Soc. Lond. A 82, 172-175 (1909).

[136] S. M. Sze, Physics of Semiconductor Devices, Wiley Sons, Taiwan, 1985.

[137] B. R. Nag, Physics of Quantum Well Devices, Kluwer Academic Press, 2002.

[138] E. O. Odoh, A. S. Njapba, A review of semiconductor quantum well devices, Advances in Physics Theories and Applications 46, ISSN 2224-719X (Paper) ISSN 2225-0638 (Online) (2015).

[139] Z. Alferov, Heterostructures for optoelectronics: History and modern trends, Proceedings of the IEEE 101, 10, 2176-2182 (2022).

[140] H. Zhang, Y. Sun, K. Song, C. Xing, L. Yang, D. Wang, H. Yu, X. Xiang, N. Gao, G. Xu, H. Suna, S. Long, Demonstration of AlGaN/GaN HEMTs on vicinal sapphire substrates with large misoriented angles, Appl. Phys. Lett. 119, 072104 (2021).

[141] M. Kneissl, D. W. Treat, M. Teepe, N. Miyashita, N. M. Johnson, Ultraviolet AlGaN multiple-quantum-well laser diodes, Appl. Phys. Lett. 82, 4441 (2003).

[142] K. Iida, T. Kawashima, A. Miyazaki, H. Kasugai, S. Mishima, A. Honshio, Y. Miyake, M. Iwaya, S. Kamiyama, H. Amano, I. Akasaki, 350.9 nm UV laser diode grown on low-dislocation-density AlGaN, Jpn. J. Appl. Phys. 43, L499 (2004).

[143] J. Cho, J. H. Park, J. K. Kim, E. F. Schubert, White light-emitting diodes: History, progress, and future, Laser Photonics Rev. 11, 1600147 (2022).

[144] H. Zhang, Y. Sun, K. Song, C. Xing, L. Yang, D. Wang, H. Yu, X. Xiang, N. Gao, G. Xu, H. Suna, S. Long, Development of highly eficient ultraviolet LEDs on hybrid patterned sapphire substrates, Opt. Lett. 46, 5356-5359 (2021).

[145] J. P. S. Zory, Quantum Well Lasers, Academic. Press. Inc., 1993.

[146] S. J. Liang, Y. Li, B. Cheng, F. Miao, Emerging low-dimensional heterostructure devices for neuromorphic computing, Small Structures 3, 10 (2022).

[147] W. Lee, M. Hon, Space-limited crystal growth mechanism of TiO_2 films by atomic layer deposition, . Phys. Chem. C 2010, 114, 15, 6917–6921 114, 15, 6917-6921 (2010).

[148] R. Puurunen, T. Sajavaara, E. Santala, V. Miikkulainen, T. Saukkonen, M. M. Laitinen, M. Leskelä, Controlling the crystallinity and roughness of atomic layer deposited titanium dioxide films, J. Nanosci. Nanotechnol. 11, 9, 8101-8107 (7) (2011).

[149] S. Ratzsch, E. B. Kley, A. Tünnermann, A. Szeghalmi, Influence of the oxygen plasma parameters on the atomic layer deposition of titanium dioxide, Nanotechnology 26, 024003 (2015).

[150] W. Chiappim, G. E. Testoni, A. C. O. C. Doria1, R. S. Pessoa, M. A. Fraga, N. K. A. M. Galvão, K. G. Grigorov, L. Vieira, H. S. Maciel, Relationships among growth mechanism, structure and morphology of PEALD TiO_2 films:

the influence of O_2 plasma power, precursor chemistry and plasma exposure mode, Nanotechnology 27, 305701 (2016).

[151] M. E. Dufond, M. W. Diouf, C. Badie, C. Laffon, P. Parent, D. Ferry, D. Grosso, J. C. S. Kools, S. D. Elliott, L. Santinacci, Quantifying the extent of ligand incorporation and the effect on properties of TiO_2 thin films grown by atomic layer deposition using an alkoxide or an alkylamide, Chem. Mater. 32, 4, 1393-1407 (2020).

[152] T. Amotchkina, M. Trubetskov, A. Tikhonravov, I. Angelov, V. Pervak, Reliable optical characterization of e-beam evaporated TiO_2 films deposited at different substrate temperatures, Appl. Opt. 53, A8–15 (2014).

[153] M. Hasan, A. Haseeb, R. Saidur, H. Masjuki, M. Hamdi, Influence of substrate and annealing temperatures on optical properties of rf-sputtered TiO_2 thin films, Opt. Mater. 32, 690-695 (2010).

[154] Y. Shi, R. Zhang, H. Zheng, D. Li, W. Wei, X. Chen, Y. Sun, Y. Wei, H. Lu, N. Dai, L. Chen, Optical constants and band gap evolution with phase transition in sub-20-nm-thick TiO_2 films prepared by ALD, Nanoscale Res. Lett. 12, 243 (2017).

[155] J. Tauc, R. Grigorovici, A. Vancu, Optical properties and electronic structure of amorphous germanium, Physica status solidi b 12, 243 (1966).

[156] G. E. Jellison, F. A. Modine, Parameterization of the optical functions of amorphous materials in the interband region, Appl. Phys. Lett. 69, 371 (1996).

[157] D. Pal, A. Mathur, A. Singh, J. Singhal, A. Sengupta, S. Dutta, S. Zollner, S. Chattopadhyay, Tunable optical properties in atomic layer deposition grown ZnO thin films, J. Vac. Sci. Technol. A 35, 01B108 (2017).

[158] S. Shestaeva, A. Bingel, P. Munzert, L. Ghazaryan, C. Patzig, A. Tünnermann, A. Szeghalmi, Mechanical, structural, and optical prop-

erties of PEALD metallic oxides for optical applications, Appl. Opt. 56, C47-C59 (2017).

[159] E. Filatova, A. Konashuk, Interpretation of the changing the band gap of Al_2O_3 depending on its crystalline form: Connection with different local symmetries, J. Phys. Chem. C 119, 35, 20755–20761 (2015).

[160] J. Moudler, W. Stickle, P. Sobol, K. Bomben, Handbook of X-ray photoelectron spectroscopy, Physical Electronics, Inc., 1995.

[161] L. Zhu, Q. Lu, L. Lv, Y. Wang, Y. Hu, Z. Deng, Z. Lou, Y. Hou, F. Teng, Ligand-free rutile and anatase TiO_2 nanocrystals as electron extraction layers for high performance inverted polymer solar cells, RSC Adv. 7, 20084-20092 (2017).

[162] G. Xing, L. Zhao, T. Sun, Y. Su, X. Wang, Hydrothermal derived nitrogen doped $SrTiO_3$ for eficient visible light driven photocatalytic reduction of chromium (vi), Springer Plus 5, 1132 (2016).

[163] A. Gautam, A. Kshirsagar, R. Biswas, S. Banerjee, P. Khanna, Photodegradation of organic dyes based on anatase and rutile TiO_2 nanoparticles, RSC Adv. 6, 2746–2759 (2016).

[164] H. Finkenrath, The moss rule and the influence of doping on the optical dielectric constant of semiconductors-I, Infrared Phys. 28, 327–332 (1988).

[165] X. Fu, M. Commandré, L. Gallais, M. Mende, H. Ehlers, D. Ristau, Laser-induced damage in composites of scandium, hafnium, aluminum oxides with silicon oxide in the infrared, Appl. Opt. 53, A392–A398 (2014).

[166] K. Abe, K. Nomura, T. Kamiya, H. Hosono, Optical evidence for quantization in transparent amorphous oxide semiconductor superlattice, Phys. Rev. B 86, 81202 (2012).

[167] M. Jupé, T. Willemsen, H. Liu, M. Steinecke, L. Jensen, D. Ristau, Manufacturing of quantized nanolaminates, Optical Interference Coatings Conference (OIC) (OSA) TB.4 (2019).

[168] S. Alam, P. Paul, V. Beladiya, P. Schmitt, O. Stenzel, M. Trost, S. Wilbrandt, C. Mühlig, S. Schröder, G. Matthäus, S. Nolte, S. Riese, F. Otto, T. Fritz, A. Gottwald, A. Szeghalmi, Heterostructure films of SiO_2 and HfO_2 for high-power laser optics prepared by plasma-enhanced atomic layer deposition, Coatings 13(2), 278 (2023).

[169] A. Anders, E. Byon, D. H. Kim, K. Fukuda, S. H. N. Lim, Smoothing of ultrathin silver films by transition metal seeding, Solid State Commun. 140, 225229 (2006).

[170] V. J. Logeeswaran, N. P. Kobayashi, M. S. Islam, W. Wu, P. Chaturvedi, N. X. Fang, S. Y. Wang, R. S. Williams, Ultrasmooth silver thin films deposited with a germanium nucleation layer, Nano Lett. 9, 1, 178–182 (2009).

[171] P. Nagpal, N. C. Lindquist, S. H. Oh, D. J. Norris, Ultrasmooth patterned metals for plasmonics and metamaterials, Science 325, 5940, 594-597 (2009).

[172] S. Rashid, M. Sebastiani, M. Z. Mughal, R. Daniel, E. Bemporad, Influence of the silver content on mechanical properties of Ti-Cu-Ag thin films, Nanomaterials 11(2), 435 (2021).

[173] A. Etiemble, C. D. Loughian, M. Apreutesei, C. Langlois, S. Cardinal, J. M. Pelletier, J. F. Pierson, P. Steyer, Innovative Zr-Cu-Ag thin film metallic glass deposed by magnetron pvd sputtering for antibacterial applications, J. Alloys Compd. 707, 155-161 (2017).

[174] Y. Qi, J. Wang, Z. Zhu, M. Li, Thermo-reliability of pvd Cr/Au on sapphire substrates for high-temperature sensors, AIP Advances 12, 065109 (2022).

[175] I. S. Lee, C. N. Whang, J. C. Park, D. H. Lee, W. S. Seo, Biocompatibility and charge injection property of iridium film formed by ion beam assisted deposition, Biomaterials 24, 13, 2225-2231 (2003).

[176] A. C. Probst, M. Stollenwerk, F. Emmerich, A. Büttner, S. Zeising, J. Stadtmüller, F. Riethmüller, V. Stehlíková, M. Wen, L. Proserpio,

C. Damm, B. Rellinghaus, T. Döhring, Influence of sputtering pressure on the nanostructure and the X-ray reflectivity of iridium coatings, Surf. Coat. Technol. 343, 101-1071 (2018).

[177] J. Hämäläinen, M. Ritala, M. Leskelä, Atomic layer deposition of noble metals and their oxides, Chem. Mater. 26 (1), 786–801 (2014).

[178] ALD database. available online: accessed on 11 February (2023).
URL www.atomiclimits.com/alddatabase.

[179] S. Wack, P. L. Popa, N. Adjeroud, J. Guillot, B. R. Pistillo, R. Leturcq, Large-scale deposition and growth mechanism of silver nanoparticles by plasma-enhanced atomic layer deposition, J. Phys. Chem. C 123 (44), 27196–27206 (2019).

[180] A. Niskanen, T. Hatanpää, K. Arstila, M. Leskelä, M. Ritala, Radical-enhanced atomic layer deposition of silver thin films using phosphine-adducted silver carboxylates, Chem. Vap. Depos. 13, 408–413 (2007).

[181] T. Hasselmann, B. Misimi, N. Boysen, D. Zanders, J. Wree, D. Rogalla, T. Haeger, F. Zimmermann, K. O. Brinkmann, S. Schädler, D. Theirich, R. Heiderhoff, A. Devi, T. Riedl, Silver thin-film electrodes grown by low-temperature plasma-enhanced spatial atomic layer deposition at atmospheric pressure, Adv. Mat. Technol. 2200796 (2022).

[182] M. Mäkelä, T. Hatanpää, K. Mizohata, J. Räisänen, M. Ritala, M. Leskelä, Thermal atomic layer deposition of continuous and highly conducting gold thin films, Chem. Mater. 29 (14), 6130–6136 (2017).

[183] M. Mäkeläa, T. Hatanpää, M. Ritala, M. Leskelä, Potential gold(I) precursors evaluated for atomic layer deposition, J. Vac. Sci. Technol. A 35, 01B112 (2017).

[184] F. S. M. Hashem, F. Grillo, V. R. Ravikumar, D. Benz, A. Shekhar, M. B. E. Grifiths, S. T. Barryc, J. R. van Ommen, Thermal atomic layer deposition of

gold nanoparticles: controlled growth and size selection for photocatalysis, Nanoscale 12, 9005-9013 (2020).

[185] D. J. Hagen, J. Connolly, I. M. Povey, S. Rushworth, M. E. Pemble, Island coalescence during film growth: An underestimated limitation of Cu ald, Adv. Mater. Interfaces 4 (18), 1700274 (2017).

[186] J. Hämäläinen, T. Sajavaara, E. Puukilainen, M. Ritala, M. Leskelä, Atomic layer deposition of osmium, Chem. Mater. 24, 55–60 (2012).

[187] M. Lashdaf, T. Hatanpää, A. O. I. Krause, J. Lahtinen, M. Lindblad, M. Titta, Deposition of palladium and ruthenium ß-diketonates on alumina and silica supports in gas and liquid phase, Appl. Catal. A 241, 51-63 (2003).

[188] T. Aaltonen, A. Rahtu, M. Ritala, M. Leskelä, Reaction mechanism studies on atomic layer deposition of ruthenium and platinum, Electrochem. Solid-State Lett. 6(9) (2003).

[189] M. Lammel, R. Schlitz, K. Geishendorf, T. K. D. Makarov, S. Fabretti, H. Reichlova, R. Huebner, K. Nielsch, A. Thomas, S. T. B. Goennenwein, Spin hall magnetoresistance in heterostructures consisting of noncrystalline paramagnetic YIG and Pt, Appl. Phys. Lett. 114, 252402 (2019).

[190] T. Aaltonen, M. Ritala, V. Sammelselg, M. Leskelä, Atomic layer deposition of iridium thin films, J. Electrochem. Soc. 151 (8), G489 (2004).

[191] M. Mattinen, J. Hämäläinen, F. Gao, P. Jalkanen, K. Mizohata, J. Räisänen, R. L. Puurunen, M. Ritala, M. Leskelä, Nucleation and conformality of iridium and iridium oxide thin films grown by atomic layer deposition, Langmuir 32 (41), 10559–10569 (2016).

[192] T. Aaltonen, M. Ritala, M. Leskelä, Ald of rhodium thin films from $Rh(acac)_3$ and oxygen, Electrochem. Solid-State Lett. 8, C99–C101 (2005).

[193] T. Aaltonen, P. Alén, M. Ritala, M. Leskelä, Ruthenium thin films grown by atomic layer deposition, Chem. Vap. Depos. 9(1) (2003).

[194] R. Müller, L. Ghazaryan, P. Schenk, S. Wolleb, V. Beladiya, F. Otto, N. Kaiser, A. Tünnermann, T. Fritz, A. Szeghalmi, Growth of atomic layer deposited ruthenium and its optical properties at short wavelengths using $Ru(EtCp)_2$ and oxygen, Coatings 8(11), 413 (2018).

[195] A. Ames, R. Bruni, V. Cotroneo, R. Johnson-Wilke, T. Kester, P. Reid, S. Romaine, S. Tolier-McKinstry, R. H. T. Wilke, Using iridium films to compensate for piezo-electric materials processing stresses in adjustable X-ray optics, Proc. SPIE 9603, Optics for EUV, X-Ray, and Gamma-Ray Astronomy VII 96031I (2015).

[196] Y. Gong, C. Wang, Q. Shen, L. Zhang, Low-temperature deposition of iridium thin films by pulsed laser deposition, Vacuum 82(6):594-598 (2008).

[197] C. Dussarrat, J. Gatineau, High purity iridium thin films depositions using the inorganic IrF_6, Proc. Electrochem. Soc. 5, 354–359 (2005).

[198] S. W. Kim, S. H. Kwon, D. K. Kwak, S. W. Kang, Phase control of iridium and iridium oxide thin films in atomic layer deposition, J. Appl. Phys. 103, 23517 (2008).

[199] J. Hämäläinen, T. Hatanpää, E. Puukilainen, L. Costelle, T. Pilvi, M. Ritala, M. Leskelä, (MeCp)Ir(CHD) and molecular oxygen as precursors in atomic layer deposition of iridium, J. Mater. Chem. 20, 7669–7675 (2010).

[200] S. Schlicht, S. Haschke, V. Mikhailovskii, A. Manshina, J. Bachmann, Highly reversible water oxidation at ordered nanoporous iridium electrodes based on an original atomic layer deposition, Chem. Electro. Chem. 5, 1259–1264 (2018).

[201] M. Peuckert, XPS study on thermally and electrochemically prepared oxidic adlayers on iridium, Surf. Sci. 144 (2-3), 451–464 (1984).

[202] R. Nyholm, A. Berndtsson, N. Martensson, Core level binding energies for the elements Hf to Bi (z=72-83), J. Phys. C: Solid State Phys. 13 (36), L1091-L1096 (1980).

[203] V. Pfeifer, T. Jones, J. V. Vélez, C. Massué, R. Arrigo, D. Teschner, F. Girgsdies, M. Scherzer, T. Greiner, J. Allan, G. W. M. Hashagen, S. Piccinin, M. Hävecker, A. Knop-Gericke, R. Schlögl, The electronic structure of iridium and its oxides, Surf. Interface Anal. 48 (5), 261–273 (2016).

[204] S. Freakley, J. Ruiz-Esquius, D. Morgan, The X-ray photoelectron spectra of Ir, IrO_2 and $IrCl_3$ revisited, Surf. Interface Anal. 49 (8), 794–799 (2017).

[205] Y. Luo, Handbook of Bond Dissociation Energies in Organic Compounds, CRC Press, 2002.

[206] M. Alam, I. Leon, R. Boyd, Large optical nonlinearity of indium tin oxide in its epsilon-near-zero region, Science 352 (6287), 795–797 (2016).

[207] L. Caspani, R. Kaipurath, M. Clerici, M. Ferrera, T. Roger, J. Kim, N. Kinsey, M. Pietrzyk, A. D. Falco, V. Shalaev, A. Boltasseva, D. Faccio, Enhanced nonlinear refractive index in ϵ-near-zero materials, Phys. Rev. Lett. 116 (23), 233901 (2016).

[208] M. Javani, M. Stockman, Real and imaginary properties of epsilon-near-zero materials, Phys. Rev. Lett. 117 (10), 107404 (2016).

[209] M. Koivurova, T. Hakala, J. Turunen, A. Friberg, M. Ornigotti, H. Caglayan, Metamaterials designed for enhanced enz properties, New J. Phys. 22 (9), 93054 (2020).

[210] L. Sun, X. Yang, J. Gao, Loss-compensated broadband epsilon-near-zero metamaterials with gain media, Appl. Phys. Lett. 103 (20) (2013).

[211] S. Beer, J. Gour, A. Alberucci, C. David, S. Nolte, U. D. Zeitner, Second harmonic generation under doubly resonant lattice plasmon excitation, Opt. Express 30, 40884-40896 (2022).

[212] J. Gour, S. Beer, A. Alberucci, U. D. Zeitner, S. Nolte, Enhancement of third harmonic generation induced by surface lattice resonances in plasmonic metasurfaces, Opt. Lett. 47, 6025-6028 (2022).

[213] N. A. Papdogiannis, S. D. Moustaizis, Nonlinear enhancement of the efficiency of the second harmonic radiation produced by ultrashort laser pulses on a gold surface, Opt. Commun. 137, 174 (1997).

[214] J. Hohfeld, S. Wellershoff, J. Güdde, U. Conrad, V. Jähnke, E. Matthias, Electron and lattice dynamics following optical excitation of metals, Chem. Phys. 251, 237 (2000).

[215] L. Girardini, E. Pog, G. Soavi, A. Tomadin, P. Biagioni, S. Conte, S. Mignuzzi, D. Fazio, T. Taniguchi, K.Watanabe, L. Duo, M. Finazzi, M. Polini, A. C. Ferrari, G. Cerullo, M. Celebrano, Tunable broadband light emission from graphene, 2D Mater. 8, 035026 (2021).

[216] A. Schiffrin, T. Paasch-Colberg, N. Karpowicz, V. Apalkov, D. Gerster, S. Mühlbrandt, M. Korbman, J. Reichert, M. Schultze, S. Holzner, J. V. Barth, R. Kienberger, R. Ernstorfer, V. S. Yakovlev, M. I. Stockman, F. Krausz, Optical-field-induced current in dielectrics, Nature 493, 70–74 (2013).

[217] F. Krausz, M. I. Stockman, Attosecond metrology: from electron capture to future signal processing, Nat. Photon. 8, 205–213 (2014).

[218] V. Hanus, V. Csajbók, Z. Pápa, J. Budai, Z. Márton, G. Z. Kiss, P. Sándor, P. Paul, A. S. Z. Wang, B. Bergues, M. F. Kling, G. Molnár, J. Volk, P. Dombi, Light-field-driven current control in solids with pJ-level laser pulses at 80 MHz repetition rate, Optica 8, 570-576 (2021).

[219] B. Fehér, V. Hanus, Z. Pápa, J. Budai, P. Paul, A. Szeghalmi, P. Dombi, Laser-induced ultrafast currents in dielectrics enhanced by iridium nanoparticles, Optica High-brightness Sources and Light-driven Interactions Congress, Technical Digest Series, paper HF3B.5 (2022).

[220] V. Hanus, B. Fehér, V. Csajbók, P. Sándor, Z. Pápa, J. Budai, Z. Wang, P. Paul, A. Szeghalmi, P. Dombi, On-chip carrier-envelope phase scanner and cep control of laser beams, submitted.

Appendix

Table : Some examples of second harmonic generation (SHG) processes in various nanoscale materials.

Materials	Growth methods	SHG properties	References
Al_2O_3/ZnO nanolaminate	ALD	χ^2_{zzz} = –4.0 pm/V χ^2_{yyz} = 1.6 pm/V χ^2_{zyy} = –4.0 pm/V	Wickberg et. al., Adv. Opt. Mater. 4, 1203–1208 (2016)
ZnO bulk		χ^2_{zzz} = 1.5pm/V	Wickberg et. al., Adv. Opt. Mater. 4, 1203–1208 (2016)
ZnO bulk		χ^2 = 1.23 pm/V	Zhu et. al., Adv. Opt. Photon. 13, 242-352 (2021)
ZnO film	PLD	χ^2_{zzz} = –13.4 pm/V	Wickberg et. al., Adv. Opt. Mater. 4, 1203–1208 (2016)
Al_2O_3/ZnO on 3D metacrystal	ALD	Two orders enhancement as compared to planar nanolaminate	Wickberg et. al., Adv. Opt. Mater. 7, 1801235 (2019)
$Al_2O_3/TiO_2/HfO_2$ nanolaminate	ALD	χ^2_{zzz} = 0.26 pm/V χ^2_{yyz} = 0.18 pm/V χ^2_{zxx} = 0.10 pm/V	Alloatti et. al., Appl. Phys. Lett. 107, 121903 (2015)
$TiO_2/Al_2O_3/In_2O_3$ nanolaminate	ALD	χ^2_{zzz} = 6.1±0.4 pm/V	Clemmen et. al., Optics letters 40, 5371–5374 (2015)
SiN film	PECVD	χ^2_{zzz} = 2.5 pm/V	Ning et. al., Appl. Phys. Lett. 100, 161902 (2012)
SiN waveguide	PECVD	χ^2_{yyy} = 0.14±0.08 pm/V χ^2_{xxy} = 0.30±0.18 pm/V	Puckett et. al., Opt. Express 24, 16923-16933 (2016)
AlN		χ^2 = 4.7 pm/V	Zhu et. al., Adv. Opt. Photon. 13, 242-352 (2021)
Au, Ag, Al, Co, Cr, Ge, Ni, Sb, Ti, TiN, W, Zn, Si, ITO, Cu	Magnetron sputtering	Relative SHG intensity in arb. unit Au, Ag, Al, W films have higher SHG than other metals	Che et. al., Results in Physics 7, 593–595 (2017)

Abbreviations and symbols

ALD	atomic layer deposition
Al_2O_3	aluminium oxide, alumina
AlN	alumium nitride
Ar	argon
AR	antireflection
ARC	antireflection coating
CEP	carrier envelope phase
CVD	chemical vapour deposition
DOS	density of states
EMA	effective medium approximation
EMT	effective medium theory
GPC	growth per cycle
H_2O	water
HfO_2	hafnium oxide, hafnia
HHG	higher harmonic generation
Ir	iridium
$Ir(acac)_3$	iridium acetylacetonate
IrO_x	iridium oxide
MEMS	micro-electromechanical systems
ms	millisecond
MSE	mean square error
O_2	oxygen
PEALD	plasma enhanced atomic layer deposition
PVD	physical vapour deposition

R	reflectance
RF	radio frequency
r.m.s.	root mean square
s	second
sccm	standard cubic centimeter per minute
SE	spectroscopic ellipsometry
SEM	scanning electron microscopy
SiN	silicon nitride
SiO_2	silicon oxide, alumina
STM	scanning tunnelling microscopy
T	transmittance
TiN	titanium nitride
TiO_2	titanium oxide, titania
TMA	trimethylaluminium
TTIP	titanium isopropoxide
UV-VIS	ultraviolet and visible
WLI	white light interferometry
XPS	x-ray photoelectron spectroscopy
XRR	x-ray reflectometry
3DMAS	trisdimethylaminosilane

ϵ	dielectric constant
E_g	optical bandap
⍰	Planck’s constant
n	refractive index
k	extinction coeficient
κ	momentum
K	wave vector
λ	wavelength
ψ	amplitude ratio
Δ	phase difference

Publications

- P. Paul, K. Pfeiffer, A. Szeghalmi, Antireflection coating on PMMA substrates by atomic layer deposition, Coatings 2020, 10 (1), 64.
- P. Paul, Md. G. Hafiz, P. Schmitt, C. Patzig, F. Otto, T. Fritz, A. Tünnermann, A. Szeghalmi, Optical bandgap control in Al_2O_3/TiO_2 heterostructures by plasma enhanced atomic layer deposition: Toward quantizing structures and tailored binary oxides, Spectrochimica Acta Part A: Molecular and Biomolecular Spectroscopy 252, 119508 (2021).
- P. Schmitt, V. Beladiya, N. Felde, P. Paul, F. Otto, T. Fritz, A. Tünnermann, A. Szeghalmi, Influence of Substrate Materials on Nucleation and Properties of Iridium Thin Films Grown by ALD, Coatings 2021, 11(2), 173.
- V. Hanus, V. Csajbók, Z. Pápa, J. Budai, Z. Márton, G. Z. Kiss, P. Sándor, P. Paul, A. Szeghalmi, Z. Wang, B. Bergues, M. F. Kling, G. Molnár, J. Volk, P. Dombi, Light-field-driven current control in solids with pJ-level laser pulses at 80 MHz repetition rate, Optica 8 (4), 570-576 (2021).
- A. Kuppadakkath, A. George, A. Tuniz, G. Q. Ngo, H. Knopf, F. Löchner, F. Abtahi, T. Bucher, M. Steinert, S. Shradha, E. Najafidehaghani, T. Käsebier, A. Gottwald, N. Felde, P. Paul, T. Ullsperger, S. Schröder, A. Szeghalmi, T. Pertsch, I. Staude, T. Vogl, U. Zeitner, A. Turchanin, F. Eilenberger. Direct Growth of Monolayer MoS_2 on Nanostructured Silicon Waveguides, Nanophotonics, 0235 (2022).
- P. Paul, P. Schmitt, V. Sigurjonsdottir, K. Hanemann, N. Felde, S. Schröder, F. Otto, M. Gruenewald, T. Fritz, V. Roddatis, A. Tünnermann, A. Szeghalmi,

Atomically Thin Metal-Dielectric Heterostructures by Atomic Layer Deposition, ACS Appl. Mater. Interfaces 2023, 15 (18), 22626-22636.

- P. Schmitt, P. Paul, W. Li, Z. Wang, C. David, N. Daryakar, N. Felde, A. Munser, M. Kling, S. Schröder, A. Tünnermann, A. Szeghalmi, Linear and nonlinear optical properties of iridium nanoparticles grown via atomic layer deposition, Coatings 2023, 13(4), 787 (Invited).

- S. Alam, P. Paul, V. Beladiya, P. Schmitt, O. Stenzel, G. Matthaeus, S. Nolte, S. Riese, F. Otto, T. Fritz, A. Gottwald, A. Szeghalmi. Heterostructure films of SiO_2 and HfO_2 for high power laser optics prepared by plasma-enhanced atomic layer deposition (PEALD), Coatings 2023, 13(2), 278.

- F. Abtahi, P. Paul, S. Beer, A. Kuppadakkath, A. Pakhomov, A. Szeghalmi, S. Nolte, F. Setzpfandt, F. Eilenberger, Enhanced surface second harmonic generation in nanolaminates, Opt. Express 31, 11354-11362 (2023).

- K. Gerold, V. Beladiya, P. Paul, D. Kästner, M. Saarniheimo, K. Niiranen, S. Schröder and A. Szeghalmi, Conformal antireflection coatings on large optical cubes, Appl. Opt. 62, B92-B96 (2023).

- M. Hazra, P. Paul, D. Kim, C. David, S. Gräfe, U. Peschel, A. Szeghalmi, A. Pfeiffer, Nonlinear polarization holography of nanoscale iridium films, arXiv.2211.03436, submitted.

- V. Hanus, B. Fehér, V. Csajbók, P. Sándor, Z. Pápa, J. Budai, Z. Wang, P. Paul, A. Szeghalmi, P. Dombi, On-Chip Carrier-Envelope Phase Scanner and CEP control of Laser Beams, submitted.

Conference contributions (only own presentations)

- (Talk) P. Paul, P. Schmitt, V. Sigurjonsdottir, K. Hanemann, F. Otto, M. Grünewald, T. Fritz, Z. Wang, W. Li, M. F. Kling, A Tünnermann, A. Szeghalmi, Structural and optical properties of atomically engineered

Ir/Al_2O_3 nanocomposites, SPIE Photonics Europe, April 3rd – 7th 2022, Strasbourg, France.

- (Invited talk + Proceeding) P. Paul, V. Beladiya, D. Kästner, M. Burkhardt, U. Schulz, A. Szeghalmi. Conformal antireflection coatings on polycarbonate domes, Proceedings of SPIE, Advances in Optical Thin Films VII 11872, 31-36 (2021), September 13th - 16th 2021, Virtual Meeting.

- (Talk) P. Paul, Md. G. Hafiz, P. Schmitt, C. Patzig, F. Otto, T. Fritz, A. Tünnermann, A. Szeghalmi, Optical Quantizing Structures in Al_2O_3/TiO_2 Heterostructures by Plasma Enhanced Atomic Layer Deposition, AVS ALD/ALE 2021, June 27th – 30th 2021, Virtual Meeting.

- (Talk + proceeding) P. Paul, Md. G. Hafiz, A. Tünnermann, A. Szeghalmi, Tunable Optical Properties in Al_2O_3/ TiO_2 Nanocomposites Fabricated by Atomic Layer Deposition (ALD), OSA Advanced Photonic Congress 2020, Novel Optical Materials and Applications, paper No2MC.4., June 13th – 17th 2021, Virtual Meeting.

- (Talk) P. Paul, K. Pfeiffer, A. Szeghalmi, Antireflection Coatings on PMMA Substrates by Atomic Layer Deposition, AVS ALD/ALE 2020, June 29th – July 1st 2020, Virtual Meeting.

- (Poster) P. Paul, P. Schmitt, W. Li, Z. Wang, N. Daryakar, C. David, K. Hanemann, R. Rafi, S. Beer, M. Kling, A. Tünnermann, A. Szeghalmi, Linear and Nonlinear Optical Properties of Iridium Nanoparticles grown by Atomic Layer Deposition, International Conference of Quantum, Nonlinear and Nanophotonics ICQNN 2022, September 5th - 9th 2022, Jena, Germany. Poster award: 3rd Prize.

- (Poster) P. Paul, P. Schmitt, K. Hanemann, V. Sigurjonsdottir, F. Otto, M. Grünewald, T. Fritz, W. Li, Z. Wang, M. Kling, A. Tünnermann, A. Szeghalmi, Structural and optical properties of atomically engineered Ir/Al_2O_3 heterostructures, AVS ALD 2022, June 26th – 29th 2022, Ghent, Belgium.

- (Poster) P. Paul, P. Schenk, A. Tünnermann, A. Szeghalmi, Ultrafast nonlinear optics in ALD nanolaminates, 1st NOA Spring School and PI workshop, March 2nd – 6th 2020, Jena, Germany.

Public outreach

- K. Pfeiffer, P. Paul, A. Szeghalmi, Functionalising complex shaped optics, Electro Optics 2021, February, 24-26.

Lebenslauf

Name: Pallabi Paul
Geburtstag: 5. September 1991
Geburtsort: Kalkutta, Indien

03/2023 - Heute	Wissenschaftliche Mitarbeiterin am Ferdinand Braun Institut, Leibniz-Institut für Höchstfrequenztechnik (FBH), Berlin
03/2019 - 03/2023	Doktorandin am Institut für Angewandte Physik an der Friedrich-Schiller-Univerität Jena
10/2016 - 02/2019	Master of Science in Photonics, Abbe School of Photonics, Friedrich-Schiller-Universität Jena
08/2014 - 08/2016	Wissenschaftliche Mitarbeiterin am S. N. Bose National Centre for Basic Sciences, Indien
07/2012 - 06/2014	Studium der Physik an der Universität Kalkutta, Indien mit dem Abschluss: Master of Science
07/2009 - 06/2012	Studium der Physik an der Universität Kalkutta, Indien mit dem Abschluss: Bachelor of Science
05/1997 - 05/2009	Schulbesuch, Schulabgangzeugnis

Jena, 05.06.2023 Pallabi Paul

Acknowledgements

At the culmination of this enriching journey, I wish to acknowledge all the persons who have supported my efforts through this phase.

First of all, I would like to express my sincere and humble gratitude to my supervisor Dr. Adriana Szeghalmi for providing me with this opportunity and for her continuous support and guidance throughout this whole learning process. I am thankful for her availability to discuss any doubts, and for sharing countless ideas and thoughts along with an enthusiastic view. These have enriched my work remarkably. Apart from the academic input, I would really appreciate her kind approach. Thank you Adriana, for everything!

I would like to thank Prof. Dr. Andreas Tünnermann for giving me this enriching exposure to work at the Institute of Applied Physics IAP, FSU and at the Fraunhofer Institute for Applied Optics and Precision Engineering IOF. I am grateful for his profound advice in many aspects for the success of our SFB 1375: Nonlinear Optics down to Atomic Scales (NOA) project.

I would like to acknowledge Dr. Sven Schröder from Fraunhofer IOF, for his advice and continuous encouragement throughout this phase. His integral view on translating research into applications has broadened my research perspectives.

I am deeply thankful to the current and former members of our Atomic Layer Deposition of Optical Coatings, IAP and Conformal Coatings, IOF groups: Dr. Kristin Gerold, Paul Schmitt, Vivek Beldiya, David Kästner, Md. Golam Hafiz, Shawon Alam, Kevin Hanemann, Raihan Rafi, Dr. Lilit Ghazaryan, Sreejesh Satheesh Kumar, and Martin Miculka for creating an open, pleasant and supportive working environment. It has been a pleasure to work with you all!

Kristin, thank you for introducing me to the cleanroom environment, and the ALD equipments. Thanks for being available for any discussions, exchange of ideas, and our varied chats over culture, society, traveling, etc. I am really amazed by your skill of structured working and very much inspired by that. I would highly appreciate you for taking the time to correct the German part of my dissertation. Working with you will always be remembered fondly.

Paul, thank you for sharing your experience on the deposition of metal films by ALD. Discussions with you gave me a broader perspective on this field which set the ground for me while developing metal-dielectric heterostructures.

Thanks to Vivek for our discussions on various tool-related issues. Your tips and tricks helped me save time in the lab in many cases. Thank you for providing me with a brief introduction to the field of bias-assisted ALD processes. Also, having Indian snacks from you from time to time was a joy!

A huge thanks go to David for his throughout support to maintain the ALD tools. I am thankful to him for answering all my doubts with immense patience.

Thanks to Raihan for sharing his knowledge on the measurement methods for observing second harmonic generation, which improved my understanding of such systems. Thanks to Kevin, Lilit, Sreejesh, and Martin for many interesting and helpful discussions and suggestions.

I am grateful to the colleagues of Microstructure Technology group IAP, especially, Natali Sergeev, Dr. Thomas Siefke, and Detlef Schelle for sharing their expertise in this field. Natali, thanks to you for the SEM measurements and also for introducing me to the tool.

I would like to thank my collaborators Dr. Felix Otto and Dr. Marco Grünewald from the Institute of Solid State Physics IFK, FSU for performing and sharing their experiences on XPS, and STM measurements. I am grateful to you for taking the time to arrange a visit to your lab. I would acknowledge Prof. Dr. Torsten Fritz for his detailed remarks on our manuscripts which guided me in improving my writing skills a lot.

My collaborators from the Ludwig Maximilian Universität Munich and Max Planck Institute for Quantum Optics, Dr. Zilong Wang, and Weiwei Li, a huge thanks goes to you for our fruitful collaboration on investigating third order nonlinearities in Ir ALD coatings. Multiple discussions with you provided me with a broader understanding of nonlinear optics in general.

Thanks to Dr. Vaclav Hanus and Beatrix Feher from the Wigner Research Centre for Physics Budapest, for our collaborations on the ultrafast current generation from thin layered materials. It was a pleasure to meet you in person at the SPIE Photonics Europe 2022.

I am grateful to Dr. Christin David from IFK Jena, for sharing her knowledge on the effective medium theory which has been an important part of my dissertation. Thanks to Dr. Olaf Stenzel from Fraunhofer IOF, for his lectures on thin film optics which built the foundation for me to pursue this exciting field of optical thin film materials.

I wish to thank the master's students: Md. Golam Hafiz, Shawon Alam, Vilborg Vala Sigurjonsdottir, Emmanuel Ebnang, and Konul Jafarova, whom I mentored during this phase. Thank you for all your questions and feedback, which led me to sharpen my understanding. It was a huge learning experience while working with you all. Especially, I would like to thank Kevin and Vilborg for their diligent efforts with the ellipsometry analysis of the Ir/Al_2O_3 systems.

I am thankful to Bodo Martin, Patrick Kabis, and Ralph Schlegel for patiently taking care of IT-related issues at the IAP and IOF. Thanks to the Secretariat team IAP for their support regarding my conference visits, placing purchase orders, and other organizational aspects. A sincere gratitude to all my colleagues at the Institute of Applied Physics IAP and the Fraunhofer IOF for this wonderful journey in a far-away land!

I would like to thank our SFB NOA consortium for organizing various activities, e.g., lecture series, women in photonics workshop, and day outs in industries, throughout this phase. It was a privilege to be a part of these. Special thanks to Barbara Kirchner for coordinating these and taking care of all our queries. I would also like to acknowledge my fellow Ph.D. candidates from our NOA consortium, especially, Fatemeh, Athira, Jeetendra, Navid, and Sebastian for all the collaborations and interesting discussions.

I would like to take this opportunity to acknowledge all my teachers and professors for their immense contributions throughout my academic journey. A humble gratitude to my physics teacher Dr. Basudev Nag Chowdhury for his fantastic approach towards learning the subject, which got me interested in physics at the first place.

I feel thankful for having a group of compassionate friends throughout various phases of my journey, especially, Suchetana, Somrita, Srijit, Subhodip, Udesha, Paulami, Reema, Nishitha, Sanchari, Ankita, Soumi, Maitrayee, Anuvab, Ayan, and many more. Special mention to our 'Lunch Group IOF': Safi, Riza, Saipriya, Anatolii, and Yeshni for all those joyful memories which used to be so mind-refreshing. Special thanks to my cousins Somali, Piku, Sayan, and Titli for being my support system even from continents apart. I wish to thank my maternal uncle, Sibendra Chaudhuri, for his continuous encouragement since my school days. Jethima, Sunanda Chowdhury, a huge thanks to you for your continuous encouragement, especially while writing the dissertation. I would like to express my gratitude to my grandparents for their unconditional love and blessings. I would fondly acknowledge my relatives in Germany, Dadu, Debaprasad Pal Chowdhury, and Dida, Marianne Pal Chowdhury for their affection and for including me as a part of their extended family. I would like to thank all my family members for their wishes and encouragement throughout my academic journey.

Pratik, I am grateful for having you in my life. Thank you for being my companion through thick and thin over the past years. Thanks for your immense support, and especially for your patience. Moreover, a big thanks for helping me out with LaTeX, and for your tips and feedback while writing the dissertation.

At this point, I would like to convey my deepest gratitude to my parents: Ma, Tithi Paul, and Baba, Asim Paul. Perhaps, I cannot thank you both enough. Thank you for your unconditional love and support. Thank you for your immense understanding, especially when I could not be in the best state of my temper. Thank you Ma, for your constant efforts, push, and encouragement since my first day in school.

Finally, I would like to thank everybody who has directly or indirectly contributed to my journey. If I missed anybody, I owe you deep gratitude.

Ehrenwörtliche Erklärung

Ich erkläre hiermit ehrenwörtlich, dass ich die vorliegende Arbeit selbständig, ohne unzulässige Hilfe Dritter und ohne Benutzung anderer als der angegebenen Hilfsmittel und Literatur angefertigt habe. Die aus anderen Quellen direkt oder indirekt übernommenen Daten und Konzepte sind unter Angabe der Quelle gekennzeichnet. Bei der Auswahl und Auswertung folgenden Materials haben mir die nachstehend aufgeführten Personen in der jeweils beschriebenen Weise entgeltlich/unentgeltlich geholfen:

- Durchführung einiger ALD-Beschichtungsexperimente - Paul Schmitt, Institut für Angewandte Physik, Jena
- Durchführung einiger spectralphotometricher und ellipsometricher Messungen - Kevin Hanemann, Vilborg Vala Sigurjonsdottir, Fraunhofer IOF Jena
- REM-Aufnahmen - Natali Sergeev, Institut für Angewandte Physik, Jena
- STEM-Aufnahmen - Christian Patzig, Fraunhofer IMWS, Halle (Saale)
- HRTEM-Aufnahmen - Vladimir Roddatis, Intitut für Materials Physik, Universität Göttingen
- Durchführung und Auswertung von XRR-Messungen - Paul Schmitt, Institut für Angewandte Physik, Jena
- Durchführung und Auswertung von XPS and STM-Messungen - Felix Otto, Marco Grünewald Institut für Festkörper Physik, Jena, Paul Schmitt, Institut für Angewandte Physik, Jena

- Durchführung und Auswertung von GIXRD-Messungen - Ingo Uschmann, Institut für Optik und Quantenelectronik, Jena

- Durchführung second harmonic generation Messungen - Raihan Rafi, Sebastian Beer, Institut für Angewandte Physik, Jena

- Durchführung und Auswertung von WLI Messungen - Nadja Felde, Fraunhofer IOF Jena

Weitere Personen waren an der inhaltlich-materiellen Erstellung der vorliegenden Arbeit nicht beteiligt. Insbesondere habe ich hierfür nicht die entgeltliche Hilfe von Vermittlungs- bzw. Beratungsdiensten (Promotionsberater oder andere Personen) in Anspruch genommen. Niemand hat von mir unmittelbar oder mittelbar geldwerte Leitungen für Arbeiten erhalten, die im Zusammenhang mit dem Inhalt der vorgelegten Dissertation stehen.

Die Arbeit wurde bisher weder im In- noch im Ausland in gleicher oder ähnlicher Form einer anderen Prüfungsbehörde vorgelegt. Die geltende Promotionsordnung der Physikalisch-Astronomischen Fakultät ist mir bekannt.

Ich versichere ehrenwörtlich, dass ich nach bestem Wissen die reine Wahrheit gesagt und nichts verschwiegen habe.

Jena, 05.06.2023 Pallabi Paul